

REPORT DOCUMENTATION PAGE

Form Approved
OMB No. 0704-0188

Public reporting burden for this collection of information is estimated to average 1 hour per response, including the time for reviewing instructions, searching existing data sources, gathering and maintaining the data needed, and completing and reviewing the collection of information. Send comments regarding this burden estimate or any other aspect of this collection of information, including suggestions for reducing this burden, to Washington Headquarters Services, Directorate for Information Operations and Reports, 1215 Jefferson Davis Highway, Suite 1204, Arlington, VA 22202-4302, and to the Office of Management and Budget, Paperwork Reduction Project (0704-0188), Washington, DC 20503.

1. AGENCY USE ONLY (Leave blank)		2. REPORT DATE		3. REPORT TYPE AND DATES COVERED FINAL REPORT 1 Oct 94 - 30 Sep 95	
4. TITLE AND SUBTITLE Modeling, Simulation and Design of High Pressure Crystal Growth Processes				5. FUNDING NUMBERS STTR-TS	
6. AUTHOR(S) Dr Kedar P. Gupta					
7. PERFORMING ORGANIZATION NAME(S) AND ADDRESS(ES) GT Equipment Technologies,, Inc 472 Amherst Street Nashua, NH 03063					
9. SPONSORING / MONITORING AGENCY NAME(S) AND ADDRESS(ES) AFOSR/NE 110 Duncan Avenue Suite B115 Bolling AFB DC 20332-0001				10. SPONSORING / MONITORING AGENCY REPORT NUMBER F49620-94-C-0092	
11. SUPPLEMENTARY NOTES					
12a. DISTRIBUTION / AVAILABILITY STATEMENT APPROVED FOR PUBLIC RELEASE: DISTRIBUTION UNLIMITED				12b. DISTRIBUTION CODE	
<p>Major research goals for this STTR project in Phase I were: (a) development of a high-resolution process model suitable for high pressure crystal growth (HPCG), (b) special experiments for thermophysical property measurement, and (c) a preliminary design of an advanced HPCG furnace to transfer the DoD technology of "one-step in-situ synthesis and MLEK growth of InP crystals" for commercialization. An extraordinary progress was made in all of these areas. Several meetings were held with Rome Laboratory researchers to identify the shortcomings of the present furnace and needs for the future generation high pressure systems. A computer model, MASTRAPP was developed that is better than all other existing numerical models for multiphase, multicomponent processes with moving boundaries and free surfaces. MASTRAPP2d with a reference manual is now available for distribution to the interested groups of researchers. New experiments were designed to obtain property data for InP density, thermal conductivity, electrical resistivity and phosphorus vapor pressure. A preliminary design for an advanced HPCG furnace was developed based on these experiments, extensive HPCG simulations and process details from Rome Laboratory. In developing this design, considerations were also made of the present US, German and Japanese HPCG technologies; quality and cost of InP as a substrate material; and possibility of growing other III-V compounds that require much higher pressures.</p>					
14. SUBJECT TERMS				15. NUMBER OF PAGES	
				16. PRICE CODE	
17. SECURITY CLASSIFICATION OF REPORT UNCLASSIFIED		18. SECURITY CLASSIFICATION OF THIS PAGE UNCLASSIFIED		19. SECURITY CLASSIFICATION OF ABSTRACT UNCLASSIFIED	
20. LIMITATION OF ABSTRACT					

AFOSR STTR Project (Phase I):

MODELING, SIMULATION AND DESIGN OF HIGH PRESSURE CRYSTAL GROWTH PROCESSES

**CONTRACT NO. F49620-94-C-0092
CONTROL NO. 94NE338**

Approved for public release,
distribution unlimited

FINAL REPORT

(November 1995)

PI: Dr. Kedar P. Gupta

**GT Equipment Technologies, Inc.
472 Amherst Street
Nashua, NH 03063**

in partnership with

**Professor Vish Prasad
Process Modeling Laboratory
Department of Mechanical Engineering
State University of New York
Stony Brook, NY 11794-2300**

Subcontractor:

**Dr. Jerry Iseler
MIT Lincoln Laboratory
Lexington, MA 02173-9108**

STAFF REPORT
NOV 1995

Classified and is
not to be released
without prior
approval of AFSC
11-250-12

DTIC QUALITY INSPECTED 1

2. Objectives

Unchanged, See the proposal.

19951206 020

3. Status of Effort

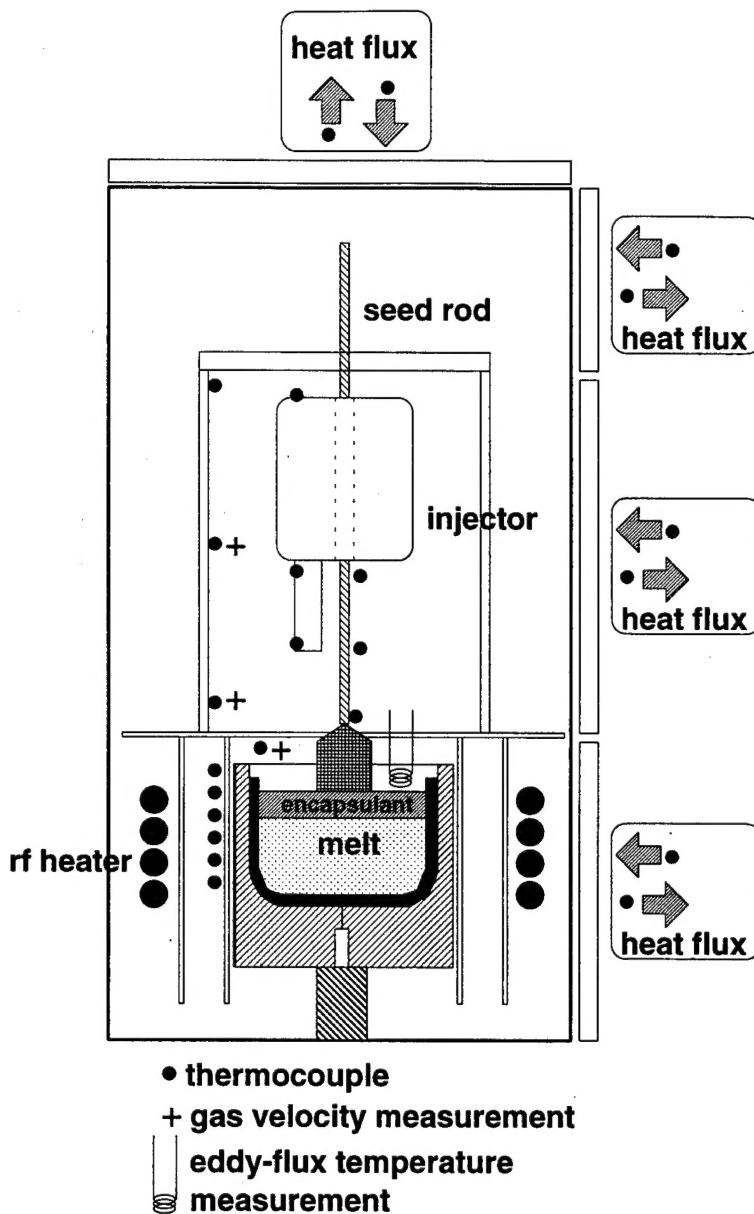
Major research goals for this STTR project in Phase I were: (a) development of a high-resolution process model suitable for high pressure crystal growth (HPCG), (b) special experiments for thermophysical property measurement, and (c) a preliminary design of an advanced HPCG furnace to transfer the DoD technology of *"one-step in-situ synthesis and MLEK growth of InP crystals"* for commercialization. An extraordinary progress was made in all of these areas. Several meetings were held with Rome Laboratory researchers to identify the shortcomings of the present furnace and needs for the future generation high pressure systems. A computer model, MASTRAPP was developed that is better than all other existing numerical models for multiphase, multicomponent processes with moving boundaries and free surfaces. MASTRAPP2d with a reference manual is now available for distribution to the interested groups of researchers. New experiments were designed to obtain property data for InP density, thermal conductivity, electrical resistivity and phosphorus vapor pressure. A preliminary design for an advanced HPCG furnace was developed based on these experiments, extensive HPCG simulations and process details from Rome Laboratory,. In developing this design, considerations were also made of the present US, German and Japanese HPCG technologies; quality and cost of InP as a substrate material; and possibility of growing other III-V compounds that require much higher pressures.

4. Phase I Research Accomplishments

Following is a brief description of the major research accomplishments made during Phase I of this STTR project.

4.1 A High Resolution Computer Model for Crystal Growth: MASTRAPP

Modeling of crystal growth processes presents several major challenges because of the inherently transient, oscillatory and three-dimensional melt and gas flows; strong coupling between convection and radiation; nonplanar, free and moving boundaries/interfaces, highly irregular geometric configuration and many other complexities. Many different algorithms have been proposed to track the moving boundaries depending upon the choice of the numerical schemes (finite element, finite difference, finite volume, or boundary element) and the selection of a grid system (structured or unstructured mesh). Several codes based on finite difference (FDM), finite volume (FVM), finite element (FEM) and combined FVM-FEM algorithms have been developed to simulate the crystal growth processes (all for the low pressure growth). Each of these methods has its own special characteristics. For example, the finite element methods can solve the stress problems much more efficiently in complex geometries. The finite difference and finite volume methods, on the other hand, are more efficient and robust for fluid flow calculations and predict accurate movements of free surfaces and solidification interfaces, especially when the thermophysical properties are allowed to vary depending upon the material, phase, temperature



Accession For	
NTIS	CRA&I <input checked="" type="checkbox"/>
DTIC	TAB <input type="checkbox"/>
Unannounced <input type="checkbox"/>	
Justification	
By _____	
Distribution /	
Availability Codes	
Dist	Avail and/or Special
A-1	

Figure 1: A schematic of the high pressure furnace for in-situ synthesis and growth at Rome Laboratory.

and pressure. The combination of FEM and FVM is therefore considered to be more suitable for crystal growth processes.

However, the combined FVM-FEM scheme suffers from many limitations/drawbacks. The main difficulty is that the grid systems are usually different for the FEM and FDM (or FVM) analyses. An interpolation scheme is therefore required that wastes a substantial amount of CPU time and makes the solution less accurate. A multizone grid generation scheme that can be used by both the FEM and FVM algorithms were not fully developed until the recent work by Zhang, Prasad and co-workers on adaptive grid generation. The most popular techniques for FDM (or FVM) analysis are the body-fitted coordinates (based on the work by Thompson and co-workers) and adaptive grid generation technique by Brackbill and Saltzman. These schemes are only suitable for single domain and steady-state problems. It is very difficult to use these formulations for complex geometries and transient, multiphase processes since no special algorithm was developed for adaptive grid distribution in the interface zone. Also, the algorithm is not suitable for a transient process since it lacks relationship between the grids at different times. The grids at the interface (between subdomains or phases) are generally not smooth, and slope discontinuities and non-orthogonality may exist in these regions. This is critical for accurate modeling of free surfaces and solidification front as in the case of crystal growth processes.

A Novel Computational Technique and Code Development

To meet the first goal of this STTR project, we have designed a special computer algorithm for multiphase, multicomponent systems with free surfaces and moving boundaries and have developed a computer code, MASTRAPP specially suitable for high pressure crystal growth processes. The numerical scheme employs (a) multizone adaptive grid generation technique (MAGG) for the discretization of physical domains of arbitrary shape, and (b) curvilinear finite volume (CFV) scheme for the discretization of the governing partial differential equations.

The MAGG scheme is based on constrained adaptive optimization of grid characteristics. The scheme preserves internal interfaces separating various zones and always makes them coincide with some grid lines. The scheme allows grids to move adaptively as the solutions progress and/or domains change. By selecting appropriate weighting functions, the grid nodes can be concentrated in regions of large variations in field variables. By using appropriate grid inertia, the rate of grid movement can be selectively adjusted. The generated grids are always smooth and orthogonal, maintain slope continuity, and cluster in the regions of interfaces/free surfaces and large gradients. This provides a specially desired feature of adaptive grid generation for HPCG simulations.

The CFV approach is based on flux discretization in the physical domain which makes the change of domain boundaries in the process model easy and less costly. More accurate solutions can be obtained by maintaining orthogonality of the grids. Combined use of these two techniques, MAGG and CFV, together with other numerical techniques has made it possible to develop a very powerful, robust computer model, MASTRAPP for accurate and efficient simulation of crystal growth processes. The details of the MASTRAPP2d version 1.0 are presented in Appendix A.

Following are some of the salient features of this computer model:

- The MASTRAPP2d version 1.0 is specially designed for crystal growth processes and is most suitable for moving and free boundaries and solidification processes in multiphase/

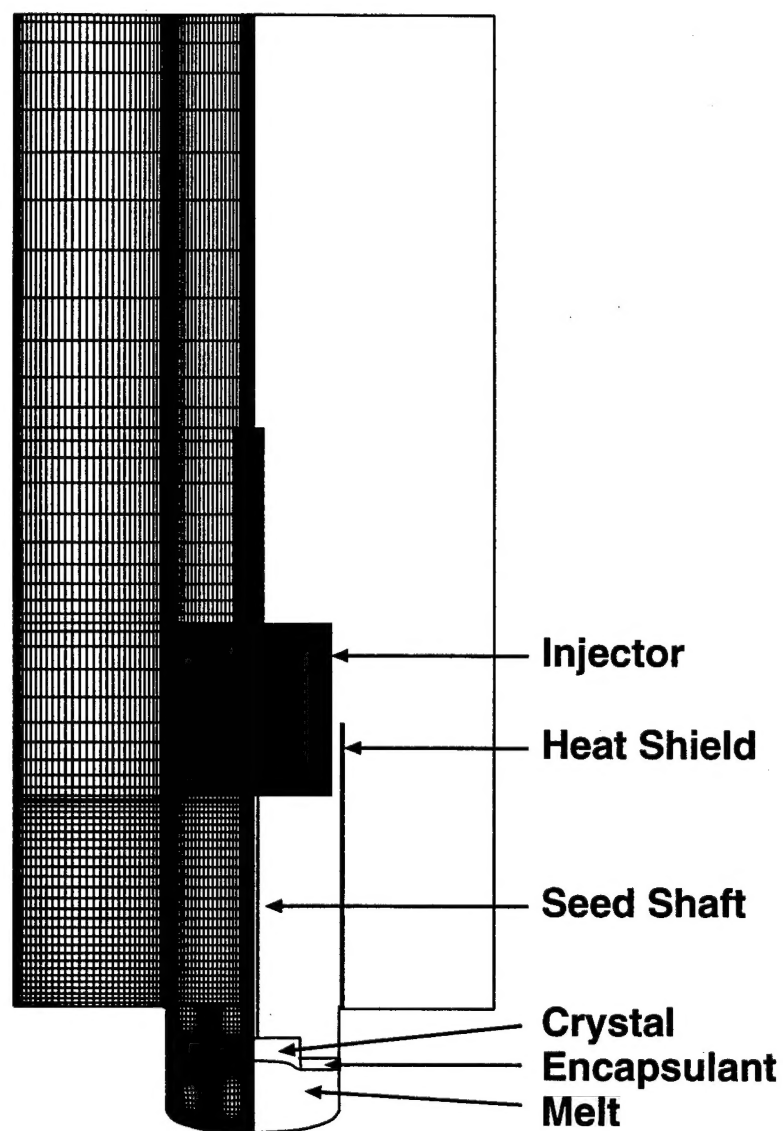


Figure 2: A schematic of the computation domain for calculations by MASTRAPP2d with a grid field.

multicomponent system. This scheme is much better than any other existing technique for this class of problems.

- The code can accurately solve the oscillatory, laminar and turbulent convective flows including natural convection produced by buoyancy forces; Marangoni convection due to surface tension forces; forced convection due to crystal rotation; Couette-type flow caused by the crucible rotation; and the effect of complex thermal boundary conditions.
- The code can account for thermophysical property variation within each zone as well as with abrupt changes in transport properties across the zone/phase boundaries.
- A magnetohydrodynamic (MHD) model has been developed and implemented into the code that can simulate the growth of InP crystals under the application of a magnetic field.
- MASTRAPP can be easily combined with a finite element code. This is a unique feature that allows efficient calculations of stress fields based on concurrently predicted temperature distribution in the crystal. Further work in this area is under progress.
- MASTRAPP is also being combined with a sophisticated radiation model that is capable of predicting node-to-node radiation exchange.
- MASTRAPP2d version 1.0 has been fully tested and is now being extended to three-dimension.
- The model can successfully simulate the in-situ synthesis and growth of InP crystals, and has been used to obtain a series of solutions for the one-step process being developed by Rome Laboratory researchers.
- MASTRAPP can be easily used to study the changes in a HPCG system configuration and consequently, help in designing a next generation furnace.

4.2 High Pressure Growth Simulations

Various stages of the "one-step" in-situ synthesis and high pressure LEK growth of indium phosphide crystals have been simulated for the first time by the present team of researchers. The numerical results (Figs. 1-4) demonstrate the complexity of the flow structure and temperature field in a HPCG system. The flow structure reported by Prasad and co-workers agrees qualitatively with the visually observed flow behavior. However, calculations are only preliminary and are not ready to be compared with the experimental data at this time due to lack of information on boundary conditions and process variables, as well as since the phosphorus vaporization and exothermic reaction have been neglected by the model. The results indicate that the thermal conditions in a HPCG system are extremely complex. The quartz shield in current design is very useful in isolating the strong convective flows in regions close to the cold wall from the buoyant flow directly above the melt, and to reduce the intensity of the gas flow along the seed shaft. The buoyancy dominated flow pattern in the system changes significantly with the rotation of the crucible and the heat shield. It stabilizes the gas flow and increases the heat transfer between the injector bottom and the gas flows. The positions of the seed and injector also affect the thermal field in the furnace dramatically. As the injector moves downward, the temperature of the injector bottom increases which is helpful for the synthesis. Since the injector temperature is controlled by an energy balance between radiation and convection heat transfer and vaporization of phospho-

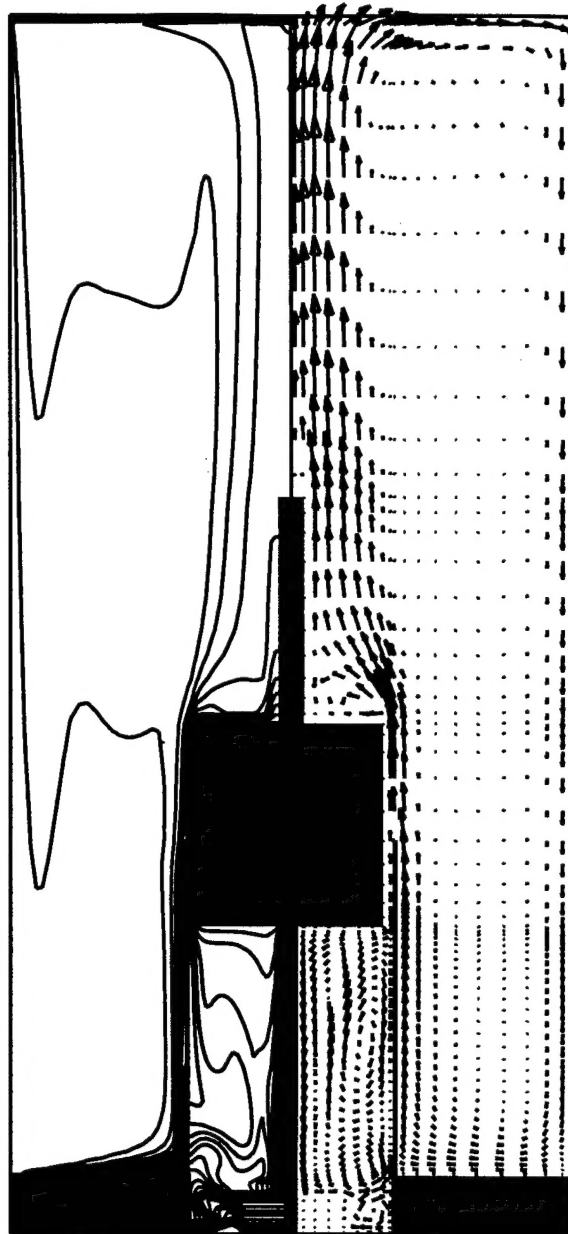


Figure 3: A representative temperature and flow field in the HPCG furnace, simulated by MASTRAPP2d.

rus, the model needs further improvement. Simulation of this kind can provide a better understanding of the HPCG process and can help the process designer to develop a process or redesign the system to achieve improved synthesis and growth conditions.

The growth of III-V compound crystals with a focus on InP has also been simulated by MASTRAPP that shows the complexity of the flow structure and temperature field in a HPCG system [1-5]. It is found that a portion of the crystal may be heated by convection from the hot crucible wall while the other portion of the crystal is cooled by convection losses to the cold walls. The radiation and conduction models, that neglect convection in the gas and widely used in the literature, are not valid for the HPCG growth. The convective heat transfer also plays a key role in setting up the interface and boundary conditions. The temperature distribution on the surface boundary is usually determined by both the convective and radiative heat transfer. Cooling on the top of the crystal also has a significant effect on the temperature distribution in the crystal, the shape and dynamics of the crystal/melt interface, and the pulling velocity. As the crystal is grown, the flow pattern as well as the shape of the crystal/melt interface are changed drastically. In the case of a small crystal, the convective heat transfer has a stronger influence due to a large volume of the gas and a short distance between the top surface of the crystal and the crystal/melt interface. On the other hand, the side wall boundary condition plays an important role in determining the crystal/melt interface and temperature distribution in the crystal when the crystal is long. Calculations presented thus far serve the purpose of demonstrating the strong effects gas convection can have on the high pressure growth.

The "one-step" synthesis and high pressure growth is one of the most challenging materials processes, particularly from the modeling standpoint, and a numerical methodology suitable for this process have a potential for the development of a robust and versatile tool for modeling and simulation of many other complex materials processes. Present simulations demonstrate the effectiveness of the MASTRAPP algorithm to simulate multiphase systems with more than one material, and free and moving interfaces, and show the complexity of the flow structure and temperature field for the synthesis in a HPCG system that will ultimately determine the success of the "one-step" process and crystal quality.

A novel approach of coupled finite volume-finite element scheme is also being developed for simultaneous flow, temperature and stress calculations. It takes advantage of the robustness of finite volume schemes in predicting high Grashof number flows and oscillations, and the versatility of the finite element algorithm for stress predictions. This FVM-FEM coupled scheme is very efficient since no new grid generation is required to calculate stresses in the crystal, and also, no iteration is needed between the FVM and FEM parts of the code [6,7]. Simulations performed thus far demonstrate that the melt convection must be included in the crystal growth model to make accurate predictions of stresses in the crystal. Most of the models reported thus far either neglect convection in the melt or assume known melt/crystal interface profile. By using a simplified stress model, we have shown that even under very small Prandtl number conditions, the convective flows of the melt has a significant influence on the interface shape and thermal stresses near the interface. Accurate calculations of thermal stresses are therefore possible only if the melt convection is included in the model and is predicted accurately. We have also shown that the present novel approach that combines the adaptive, curvilinear finite volume with the finite element scheme, provides an efficient algorithm for the simulation of coupled melt flow, heat transfer and thermal stress problem for crystals growth processes. It utilizes the inherent advantages of MASTRAPP scheme in accurate front tracking, computational efficiency, and

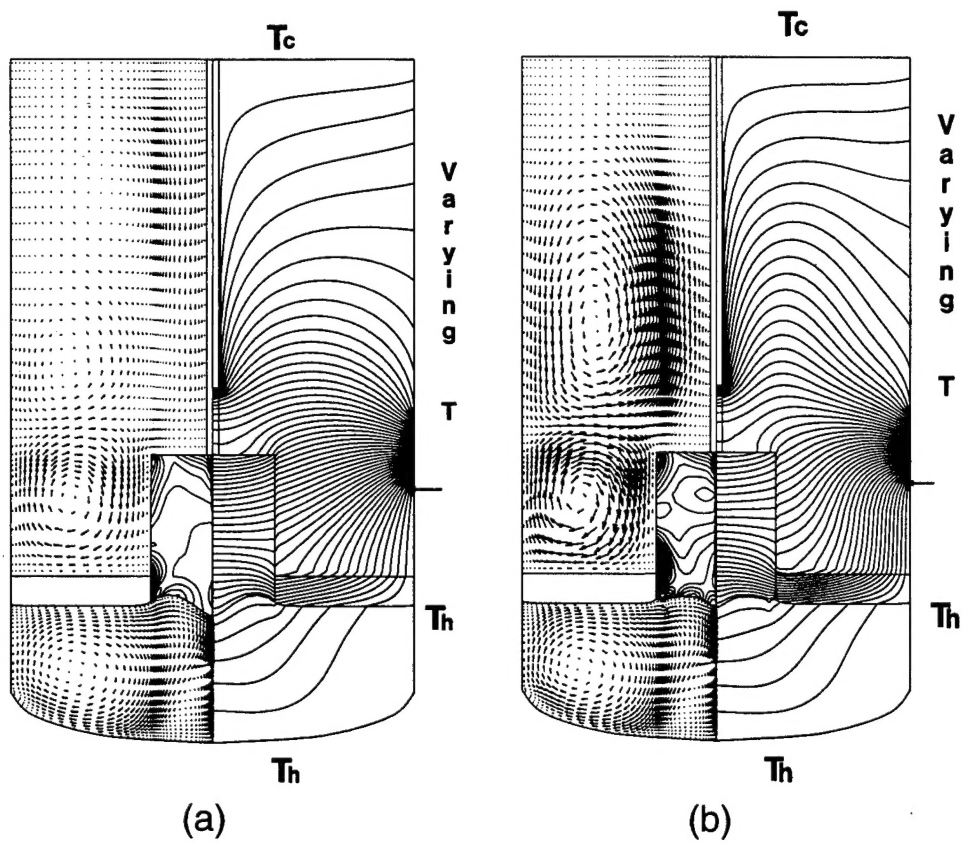


Figure 4: Distributions of temperature, stress, and stream function for high pressure growth (a) at gas Grashof number, $Gr_g = 10^7$ and $Re_s = -10^2$, $Re_c = 10^2$ and $Gr_l = 10^6$, (b) $Gr_g = 10^8$, $Re_s = -10^2$, $Re_c = 10^2$ and $Gr_l = 10^6$.

solution adaptivity and conveniently couples with the FEM algorithm which has always been considered to be the best method for stress calculations. The effect of melt convection on temperature field and thermal stresses in the crystal, particularly in the interface region is consistent with the reported results (Fig. 4). For more accurate predictions of thermal stresses in the crystal, we need to add more comprehensive radiation and turbulence models in the Cz simulation algorithm.

To study the effect of applied magnetic field that has been reported to stabilize the melt flow and interface oscillations in the Cz growth, the transport model has been extended to account for the electro-magnetic effects [8]. The numerical results indicate that the strength of the convective flow is reduced with the application of a magnetic field, and consequently, it can suppress the melt flow oscillations (Fig. 5). The temperature field and the shape of the crystal/melt interface are therefore more stable in a magnetic Cz process. The solidification interface is most often concave with respect to the crystal at high pull rates, and convex at low pull rates. However, the convection in the melt is preserved even when a moderately strong magnetic field is applied. In fact, the experimental data has shown that the convective flow pattern departs from the axisymmetric structure when a strong magnetic field is superimposed. This phenomenon is being further investigated. Figure 4 presents the effect of an applied magnetic field on melt flows and interface profile. Since the microstructure of the crystal, distribution of impurities and crystal striations are strongly dependent on convection in the melt, an applied magnetic field can be very helpful in improving the melt conditions. However, optimal process conditions must be determined to impose a magnetic field and justify its high cost.

The papers based on these numerical results are presented in Appendix B-E.

4.3 Thermophysical Property Measurements and Pressure Data

Several innovative experiments were designed and conducted to measure some of the important thermophysical properties of InP melt and solid as well as to obtain vapor pressure data. Generally, these experiments are highly sophisticated and cumbersome, and in many cases they need to be repeated several times before any meaningful information can be obtained. Of particular importance to the experimentalists in this field are:

- Design of a pressure balancing system to obtain data on vapor pressure of phosphorus over different compositions of InP, e.g., $\text{In}_{0.86}\text{P}_{0.14}$ and $\text{In}_{0.495}\text{P}_{0.505}$.
- Use of a graphite probe to locate the top of the solid and melt as well as the melt/solid interface by sensing the electrical contact in order to measure the density ratio of InP melt and solid.
- Thermal conductivity measurements by using two concentric graphite cylinders with InP melt in between and heated by a submerged molybdenum heater.

Experimental data have been obtained for vapor pressure of phosphorus for $\text{In}_{0.86}\text{P}_{0.14}$ and $\text{In}_{0.495}\text{P}_{0.505}$ melt at 1100°C, 0.35 and 31.3 atm, receptively. The value of 31.3 atm is comparable to 31.7 atm reported by Bachman and Buehler (1974) for $\text{In}_{0.495}\text{P}_{0.505}$. The electrical resistivity of n-type InP has been obtained as $\rho \leq 2.5 \times 10^{-3} \Omega \text{ cm}$. The change in density for InP melt after freezing is obtained as 1.1% which is much lower than that reported by Glazov et al. (1977), and

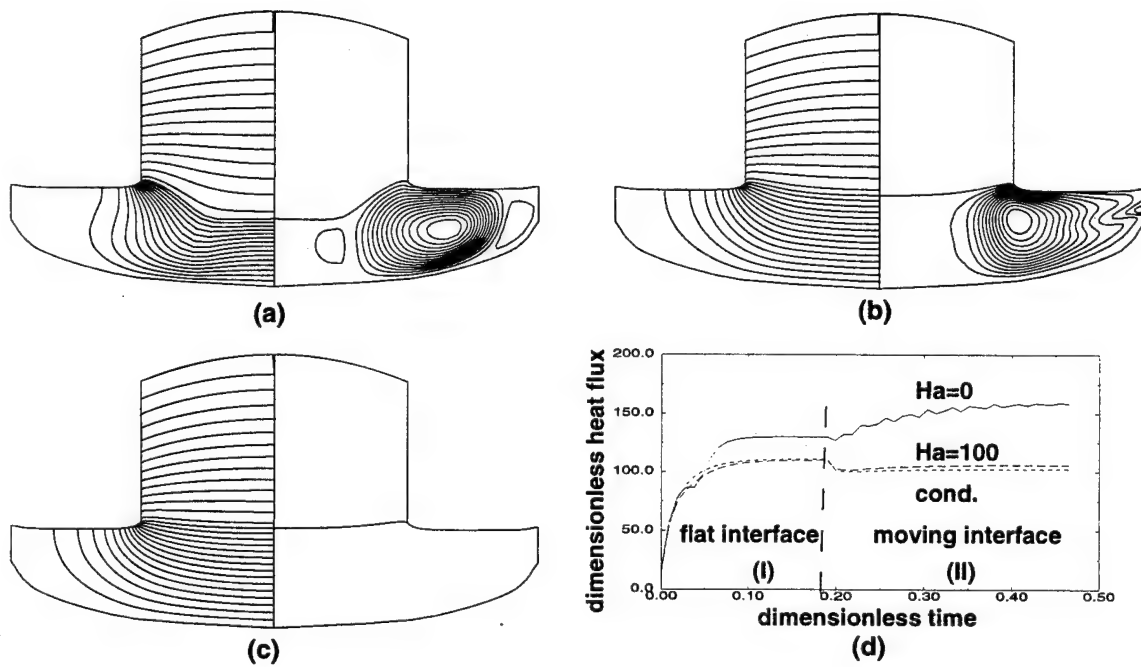


Figure 5: stream function and temperature distributions for oscillatory CZ Si melt flows with and without applied magnetic field for $Gr = 10^7$

is being further investigated to determine the reliability of the present or previously reported data. The thermal conductivity data shows a large variation in its value with temperature. It is important to note that these measurements are extremely important for the use of InP as a substrate material and very little effort was devoted in the past to obtain this information. The details of the measurement techniques and experimental data are presented in Appendix F.

4.4 Preliminary Design of a Next Generation High Pressure Furnace

A tentative design (Fig. 6) for a state-of-the-art crystal growth system suitable for production of large diameter, defect-free InP crystals has been finalized (Table 1) based on the inputs from modeling and simulations at Stony Brook and some critical experiments at MIT Lincoln Lab and Rome Lab. Several brain storming sessions, group meetings, extensive research into current US, German and Japanese technologies and future trends led to the proposed preliminary design.

The advanced HPCG furnace will have the following features:

- Working pressure up to 1,000 psi. This will allow the use of this furnace for study of the InP growth at much higher pressures than 600 psi (current value) as well as experiments on other III-V compounds that require pressure beyond 600 psi.
- Crucible diameter of 6" (current value: 4"). This will allow growth of up to 4" diameter InP crystals. (The current industry standard is 2" and the Rome Lab researchers can grow up to a maximum of 3" diameter crystal with the present furnace.)
- The new chamber design will have better thermal conditions, easy setup and cleaning.
- A unique injector system at the top of the chamber makes the in-situ synthesis much better manageable. The phosphorus injector will be heated by a separate heater that will allow a better control of the synthesis process. (Currently, P-vapor is generated by radiation heating from the melt and the injector is placed inside the furnace creating serious difficulties in operation and control.)
- The design of this furnace is unique and allows full movement of outside magnets so that they could be positioned at any melt level with ease. This can allow application of a cusp magnetic field as well as an axial field at any height with respect to the melt/crystal interface. Since the high pressure chamber does not have protruded flanges, there will be a substantial saving in the cost of magnets for the furnace to be built for Rome Laboratory in Phase II. For commercial application, this design provides compactness, ease of operation and easy accessibility to the inside of the furnace.
- The proposed design has provisions for adequate number of sensors for sensing and feedback control of the crystal growth processes.
- Provisions have also been made for two zone heating of the melt with two power supplies for a better control of the melt temperature gradient. A third power supply will be used for phosphorous injection during the melt synthesis.

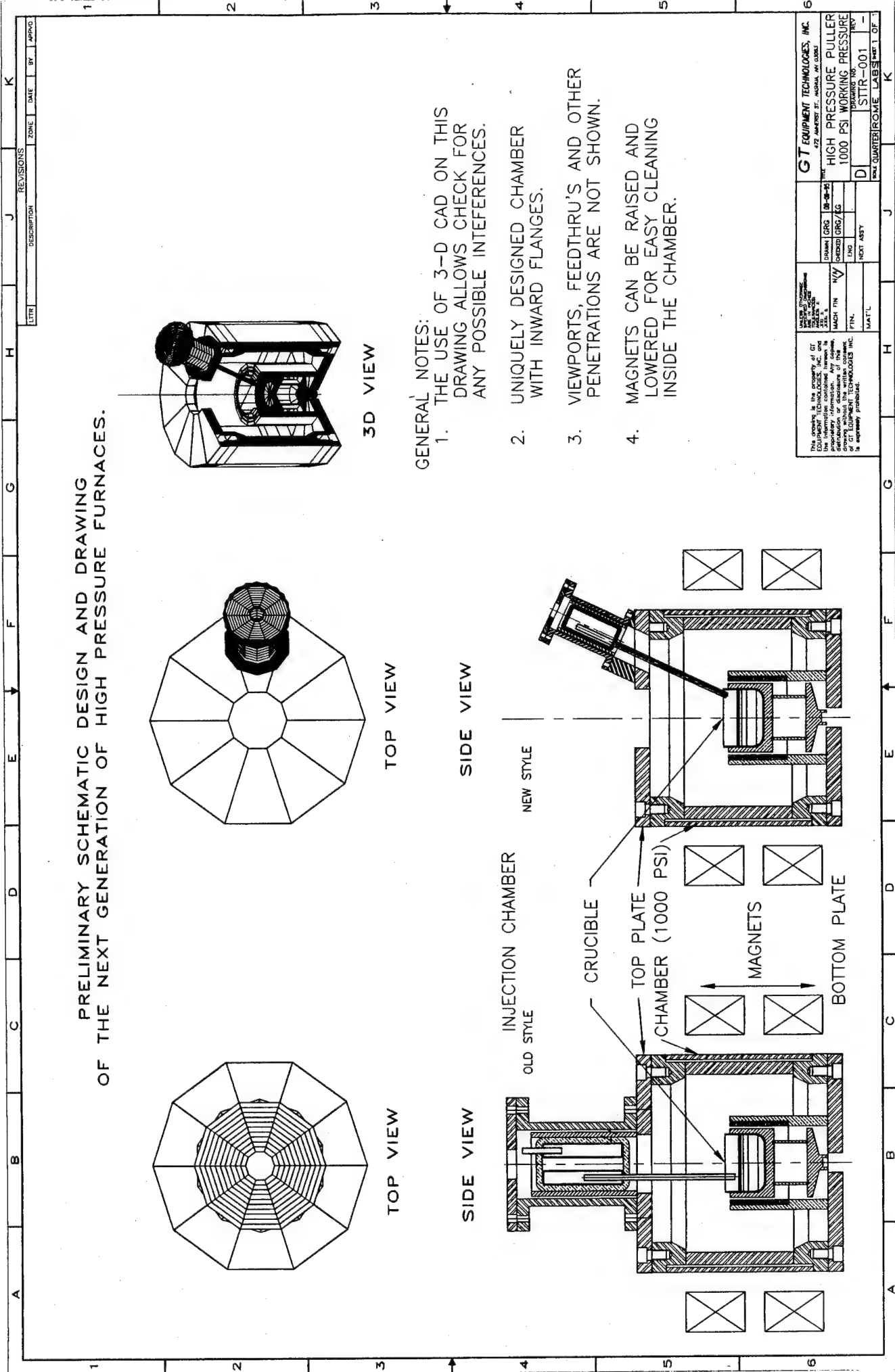


Figure 6. Preliminary design of the next generation high pressure crystal growth system that is suitable for in-situ synthesis. This will allow a much better control of synthesis and growth.

Table 1. Preliminary key specifications of the next generation HPCG Furnace

ID of pressure chamber:	18"
OD of pressure chamber:	22"
Maximum crystal diameter:	4"
Maximum crucible diameter:	6"
Maximum charge size:	8 kg
Maximum crystal length:	6"
Maximum allowable pressure:	1,000 psi
Number Power Feed Throughs:	4
Gas Cone:	Provided quartz dome
Diameter control camera:	CCD type using 1.5 view port
Temperature measurement:	ACCU fiber type
Melt sensor:	provided
Power Supply:	25 kW
Injector system:	Provided
Vacuum system:	Provided
Crucible rotation:	0-30 RPM
Seed rotation:	0-30 RPM

- A three-dimensional CAD system is being used to design this furnace to ensure that there is no interference between various parts when they move during the growth process.
- All of the above features are unique to the proposed system and are generally not available either in the present furnace at Rome Laboratory or the high pressure puller in the world market. (Note that no HPCG furnace is commercially available for one-step in-situ synthesis and growth.)

5. Personnel Supported

GT Equipment Technologies, Inc.

Dr. Kedar P. Gupta, President and PI
 Mr. Jonathan A. Talbott, B.S. (Electrical Engineering), Vice-President
 Mr. Rick White, B.S. (Electrical Engineering), Electrical Designer
 Mr. George Gauthier, B.S. (Mechanical Engineering), Mechanical Designer

State University of New York at Stony Brook

Dr. Vish Prasad, Professor, Mechanical Engineering
 Dr. Hui Zhang, Research Scientist (Mechanical Engineering)

MIT Lincoln Laboratory

Dr. Jerry Iseler, Electronic Materials

6. Publications

1. H. Zhang, V. Prasad and D. F. Bliss, "Transport Phenomena in a High Pressure Crystal Growth System: In-situ Synthesis for InP Melt," *Journal of Crystal Growth* (submitted).
2. H. Zhang, V. Prasad and D. F. Bliss, "Transport Phenomena in High Pressure Crystal Growth Systems for III-V Compounds," *Journal of Crystal Growth* (submitted).
3. Y.F. Zou, H. Zhang and V. Prasad, "Dynamics of Melt-Crystal Interface and Thermal Stresses in Czochralski Grown Crystal," *Eleventh International Conference on Crystal Growth*, The Hague, 1995; also, *Journal of Crystal Growth* (in press).
4. H. Zhang and V. Prasad, "Transport Phenomena of Czochralski Crystal Growth at Low and High Pressures," *Proc., 2nd ISHMT/ASME Heat and Mass Transfer Conference*, Surathkal, 1995.

7. Interactions

(a) Participation/Presentations

Dr. V. Prasad attended the following meetings:

National Heat Transfer Conference, Portland, Oregon, August 5-8, 1995 (Paper Presentations with Dr. H. Zhang)

AFOSR Computational Mathematics Grantees Workshop, Albuquerque, June 1995 (Paper Presentation)

Eleventh International Crystal Growth Conference, The Hague, The Netherlands, June 1995 (Paper Presentations)

First Kick-Off Meeting, ARPA/AFOSR Consortium for Crystal Growth Research, SUNY at Stony Brook, June 8-9, 1995.

American Ceramic Society Annual Meeting, April-May 1995 (Invited Review Paper Presentation)

3rd ASME-JSME Thermal Engineering Joint Conference, Maui, Hawaii, March 1995 (Paper Presentation)

International Mechanical Engineering Congress and Exposition, Chicago, November, 1994 (Paper Presentations with Dr. H. Zhang)

Dr. V. Prasad presented the following seminars:

University of Erlangen-Nuremberg, Erlangen, Germany, June 1995 (seminar)

ZARM, Space Research Center, Bremen, Germany, June 1995 (seminar)

University of Cincinnati, May 1995 (seminar)

All of the above paper presentations and seminars were on high pressure crystal growth and MASTRAPP related topics. Travel expenses to attend these meetings were paid from other grants to Professor Prasad.

Dr. Kedar Gupta and *Mr. Jonathan Talbott* visited the Semicon Show in San Francisco for investigating the availability of High Pressure Chambers and sensors (July 10-13, 1995).

(b) Consultive and Advisory Functions

We have developed a very successful professional relationship with the Rome Laboratory researchers, and are confident that we will be able to commercialize their technique for high pressure in-situ synthesis and growth. Several joint meetings were held either at GTi or Rome Laboratory. These meetings were attended by the researchers from GT Equipment Technologies, SUNY at Stony Brook, MIT Lincoln Laboratory and Rome Laboratory.

Schedule for Meetings for the STTR Project

Date	Location	Description	Attendees
10/13/94	GT Equipment Technologies	Technical Discussion	Dr. Kedar P. Gupta, GTi Mr. Jonathan Talbott, GTi Dr. Hui Zhang, SUNY at Stony Brook Prof. Vish Prasad, SUNY at Stony Brook
10/14/94	G T Equipment Technologies	Technical Discussion	Dr. Kedar P. Gupta, GTi Mr. Jonathan Talbott, GTi Mr. David Bliss, Rome Lab Dr. Andrew Anselmo, Rome Lab Mr. Jerry Iseler, MIT Lincoln Lab Prof. Vish Prasad, SUNY at Stony Brook Dr. Hui Zhang, SUNY at Stony Brook
11/29/94	GT Equipment Technologies	Technical Discussion	Dr. Kedar P. Gupta, GTi Mr. Jonathan Talbott, GTi Prof. Vish Prasad, SUNY at Stony Brook
12/31/94	Rome Lab	Lab visit & Technical discussion	Mr. Jonathan Talbott, GTi Mr. George Bryant, Rome Lab Mr. David Gabbe, Rome Lab Mr. David Bliss, Rome Lab Dr. Andrew Anselmo, Rome Lab
1/11/95	G T Equipment Technologies	Technical Discussion	Dr. Kedar P. Gupta, GTi Prof. Vish Prasad, SUNY at Stony Brook Mr. Jerry Iseler, MIT Lincoln Lab Mr. George Bryant, Rome Lab Mr. David Bliss, Rome Lab Dr. Andrew Anselmo, Rome Lab

2/13/95	Rome Lab	Lab visit & Technical discussion	Mr. Rick White, GTi Mr. Jonathan Talbott, GTi Mr. David Bliss, Rome Lab Mr. David Gabbe, Rome Lab Dr. Andrew Anselmo, Rome Lab Mr. George Bryant, Rome Lab
4/17/95	GT Equipment Technologies	Technical Discussion	Dr. Kedar P. Gupta, GTi Mr. Jonathan Talbott, GTi Mr. Jerry Iseler, MIT Lincoln Lab Dr. Andrew Anselmo, Rome Lab Mr. David Bliss, Rome Lab Prof. Vish Prasad, SUNY at Stony Brook
7/7/95	GT Equipment Technologies	Technical Discussion	Dr. Kedar P. Gupta, GTi Dr. Andrew Anselmo, Rome Lab Mr. George Gauthier, GTi
8/15/95	Rome Lab	Lab visit & Technical discussion	Dr. Kedar P. Gupta, GTi Prof. Vish Prasad, SUNY at Stony Brook Dr. Jerry Iseler, MIT Lincoln Lab Mr. David Bliss, Rome Lab Dr. Andrew Anselmo, Rome Lab Mr. George Bryant, Rome Lab
9/14/95	AFOSR, Bolling AFB		Dr. Kedar P. Gupta Prof. Vish Prasad, SUNY at Stony Brook
9/23-24/95	SUNY at Stony Brook	Technical Discussion	Dr. Kedar P. Gupta, GTi Prof. Vish Prasad, SUNY at Stony Brook Dr. Hui Zhang, SUNY at Stony Brook

(c) Transitions

Our results have provided a better understanding of the InP growth process. The computer model MASTRAPP has already been transferred to a Rome Lab computer. Dr. Andrew Anselmo, a NRC Research Fellow at Rome Laboratory is in the process of developing a proper background to run this code at the Laboratory. The code is also available for transfer to any other DoD Laboratory if they wish to simulate the CZ, MCZ, LEC and/or MLEK crystal growth processes.

The code MASTRAPP is also being used for other NSF and AFOSR supported crystal growth research at SUNY at Stony Brook. The code has already been transferred to researchers at several universities such as Caltech, Tennessee Technological University, VPI, Boston University, Manhattan College and further discussions are underway to transfer it to many other institutions as well as industries.

(d) New Discoveries

Computer code: MASTRAPP2d version 1.0

A Preliminary Design of Next Generation High Pressure Crystal Growth Furnace

(e) Honors/Awards

Professor V. Prasad was elected a Fellow of American Society of Mechanical Engineers. Dr. Prasad's citation includes his contributions to the crystal growth research.

Bibliography

1. H. Zhang and V. Prasad, "Multizone Adaptive Process Model for Czochralski Crystal Growth at Low and High Pressures," *J. Crystal Growth* Vol. 155, pp. 47-65 (1995).
2. V. Prasad and H. Zhang, "Challenging Issues in Bulk Crystal Growth Modeling," Invited paper, *Proc. American Ceramic Society Annual Meeting*, Cincinnati (1995), to be published in a Symposium Volume.
3. H. Zhang, V. Prasad and D. Bliss, "Transport Phenomena in a High Pressure Crystal Growth System: In-situ Synthesis for InP Melt," *J. Crystal Growth* (submitted).
4. H. Zhang, V. Prasad and D. Bliss, "Transport Phenomena in High Pressure Crystal Growth Systems for III-V Compounds," *J. Crystal Growth* (submitted).
5. H. Zhang and Prasad, V. "Multizone Adaptive Simulations for High Pressure Crystal Growth," *ASME-JSME Thermal Engineering Joint Conference*, Hawaii, pp.559-568, 1995.
6. Y. F. Zou, H. Zhang and V. Prasad, "Coupled Melt Flow and Stress Predictions for Czochralski Crystal Growth Processes," *National Heat Transfer Conference*, Portland, 1995.
7. Y. F. Zou, H. Zhang and V. Prasad, "Dynamics of Melt-Crystal Interface and Thermal Stresses in Czochralski Grown Crystal," *Eleventh International Conference on Crystal Growth*, The Hague, 1995; also, *Journal of Crystal Growth* (in press).
8. H. Zhang and V. Prasad, Transport Phenomena of Czochralski Growth at Low and High Pressures, *Second ISHMT-ASME Heat and Mass Transfer Conference*, Surathkal, Mangalore, India, December, 1995.

APPENDIX A

MASTRAPP

Multizone Adaptive Scheme for Transport and Phase-Change Processes

A General Purpose Computer Code for Phase-Change and Free
Surface Problems

REFERENCE MANUAL

for

MASTRAPP2d Version 1.0

(Special Version for High and Low Pressure Crystal Growth Processes)
1995

H. Zhang and V. Prasad
Department of Mechanical Engineering
State University of New York
Stony Brook, NY 11794-2300

CONTENTS

1.	INTRODUCTION	3
1.1	Purpose of the Manual	3
1.2	Capability and Limitation of MASTRAPP2d 1.0	3
1.3	Structure of MASTRAPP2d 1.0	5
2.	MATHEMATICAL FRAMEWORK	5
2.1.	Governing Differential Equation	5
2.2.	Turbulence Model	6
2.3.	Solidification Interface and Free Surface	7
2.4.	Moving Interface Tracking Scheme	8
2.5.	Electric-Magnetic Field	8
2.6.	Application for Crystal Growth	9
3.	OVERVIEW OF THE COMPUTER PROGRAM	9
4.	MULTIZONE ADAPTIVE GRID GENERATION	11
4.1.	General Formulations	11
4.2.	Boundary Node Distribution	14
4.3.	Adaptive Grid Generation for Internal Interfaces	15
5.	CURVILINEAR FINITE VOLUME DISCRETIZATION	16
5.1.	General Formulations	16
5.2.	Discretization Formulation	19
5.3.	Momentum Equation and Momentum Interpolation Method	20
5.4.	Treatment of Pressure-Velocity Coupling	21
5.5.	Pressure Correction Equation	23
5.6.	Pressure Equation	23
5.7.	Solution Procedure	23
5.8.	Treatment of Multistep and Multizone Problems	24
6.	SUBROUTINES OF MASTRAPP2d 1.0	26
7.	LIST OF VARIABLES	29
8.	CONCLUDING REMARKS	33
	REFERENCE	34
	APPENDIX I	36

1. INTRODUCTION

The acronym MASTRAPP2d stands for Multizone Adaptive Scheme for Transport and Phase-change Processes, two-dimensional. MASTRAPP2d is a workstation version designed for two-dimensional problems. It is a general-purpose program for calculation of fluid flow, heat and mass transfer, turbulence, and magnetic field in an irregular multiphase, multicomponent domain with moving phase-change interfaces and free surfaces.

1.1 Purpose of the Manual

This manual provides a documentation of MASTRAPP2d 1.0, the first version prepared for low and high pressure crystal growth processes. It describes the mathematical formulation, the numerical scheme, the solution procedure, and finally, the subroutine structure. The technique and applications of the MASTRAPP2d can be found in several papers by the present authors, most importantly:

Zhang, H. and Prasad, V., 1995, "A Multizone Adaptive Process Model for Crystal Growth at Low and High Pressures," Journal of Crystal Growth (in press).

Hui Zhang, Ph.D. Dissertation, "A Multizone Adaptive Grid Generation Technique for Simulations of Moving and Free Boundary Problems".

Zhang, H., and Moallemi, M.K., 1995, "A Multizone Adaptive Grid Generation Technique for Simulation of Moving and Free Boundary Problems," Numerical Heat Transfer, Part B, Vol. 27, pp. 255-276.

Zhang, H., Prasad, V., and Moallemi, M.K., 1995, "Application of MAGG - A Multizone Adaptive Generation technique - for Simulations of Moving and Free Boundary Problems," Numerical Heat Transfer (submitted).

The philosophy and the rationale behind the choices made to develop this novel numerical algorithm are dealt with in these papers. Since the program structure follows somewhat the SIMPLER scheme of Patankar, it may be helpful if the reader is familiar with the scheme or has read his book: *Numerical Heat Transfer and Fluid Flow* (Hemisphere, 1980).

1.2 Capability and Limitation of MASTRAPP2d 1.0

The numerical methodology of MASTRAPP2d is developed based on the multizone adaptive grid generation (MAGG) technique of Zhang and co-workers, and a curvilinear finite volume discretization method. The MAGG technique provides the capabilities for (a) accurate representation of the irregular boundaries, (b) better treatment of single and multiple moving and free boundaries, and (c) efficient, adaptive distribution

of grid nodes in response to the development of the solution and/or the evolution (enlargement/shrinkage) of the domain with time. The curvilinear finite volume scheme is based on flux discretization in the physical domain. Therefore, physical process models with complex geometric configuration can be easily implemented and modified. The solution convergence is fast and accurate, since no additional nonlinearity or artificial source terms that appear in the conventional coordinate transformation methods, are introduced during the discretization of the governing equations. The code is discretized based on a non-orthogonal curvilinear finite volume (CFV) scheme on a non-staggered grid. The CFV scheme employs flux discretization in the physical domain, that makes it easy to incorporate physical process model modifications into the computer algorithm, and the predictions can be readily examined.

MASTRAPP2d 1.0 is capable of incorporating and predicting the following physical effects:

- Two-dimensional, transient flow, temperature and concentration fields in the melt and gas phases, and diffusion in the solid.
- Oscillatory, turbulent flows and heat transfer.
- Effects of buoyancy, surface tension and magnetic forces.
- Shapes and dynamics of melt/solid interface, meniscus, and free surface; and variations with changes in melt and gas flow structure, rate of heat transfer, surface tension and pressure fields.
- Variable boundary conditions.

The program greatly simplifies for both Cartesian (x,y) and axisymmetric polar (x,r) coordinate systems. The code is, however, still in the developing stage. The turbulence part is not yet fully tested and the wall function used in the present algorithm is somewhat old-fashioned. Updated wall functions that are more realistic and are suitable for curvilinear walls are expected to be incorporated in the updated version.

Three-dimensional and parallel features will also be included in the future versions. The algorithm is, however, based on an elliptic formulation. This code is not suitable for hyperbolic problems, chemical reaction that deals with the detailed chemistry, and combustion problems that are highly compressible. The density variation problems cannot be handled by the present version of this code.

1.3 Structure of MASTRAPP2d 1.0

MASTRAPP2d 1.0 is constructed in two parts: the invariant part and the user application part. The invariant part contains the general calculation scheme that is common to all possible applications of the problem. The user application part provides the problem specification. It is here that the actual details of geometry, fluid properties, flow rates, heat sources, reaction rates, boundary conditions, desired output, etc. are supplied. Three demonstrations are available in the code. IDEMON=1 is the cavity flow with one side of the wall heated and the opposite wall cold, IDEMON=2 presents the axisymmetric cavity flow with hot sidewall and bottom, and cold free surface at the top. IDEMON=3 shows the Czochraski (Cz) growth of silicon crystals. Deformable solidification front and free surface are included in this case. The output data can be directly used by the graphics software TECPLOT. A small transfer program may be required if any other graphics package is used.

2. MATHEMATICAL FRAMEWORK

The wide applicability of MASTRAPP results from the recognition that many of the physical processes can be represented by a general mathematical formulation. As is well known, the transport of momentum, temperature, impurities, dopants, turbulence, electric-magnetic field variables, and many other quantities can be described by a general differential equation for convection-diffusion.

2.1. Governing Differential Equation

The transport of a general dependent variable ϕ in a time-dependent situation is governed by

$$\frac{\partial}{\partial t}(\bar{\rho} r^n \phi) + \frac{\partial}{\partial z}(\bar{\rho} r^n u \phi) + \frac{\partial}{\partial r}(\bar{\rho} r^n v \phi) = \frac{\partial}{\partial z}(r^n \Gamma_\phi \frac{\partial \phi}{\partial z}) + \frac{\partial}{\partial r}(r^n \Gamma_\phi \frac{\partial \phi}{\partial r}) + r^n S_\phi \quad (0.1)$$

where ϕ is the generalized variable, S is the volumetric source, and Γ is the diffusion coefficient. The index n is set to zero if the Cartesian coordinates are used, and to unity if the polar coordinates are employed. Equation (1) can be used for the entire multiphase, multicomponent domain with the provision to account for local properties and abrupt changes in transport properties across the zone boundaries, and their possible movements. This equation can also represent the conventional $k - \epsilon$ turbulence model.

The governing equations used in IDEMON=3 for Cz growth are presented in detail in Table 3 and 4. More detailed information can be found in Appendix I and the papers noted earlier [1-4] as well as in [5-7].

Table 0.1: Variables for Generalized Governing Equation (1)

Equations	Variable ϕ	Diffusivity Γ	Source S
Continuity	1	0	0
z - momentum ⁺	u	$\bar{\mu}_{eff}$	$-\partial p/\partial z + Gr\bar{\beta}\bar{\rho}\theta + S_{turb} + S_{mag}$
r - momentum ⁺	v	$\bar{\mu}_{eff}$	$-\partial p/\partial r - v/r^2 + w^2/r - (2/r^2) \partial w/\partial \theta + S_{turb} + S_{mag}$
rw^* - angular momentum ⁺	rw	$\bar{\mu}_{eff}$	$-(2/r) \partial(rw)/\partial r + \partial p/\partial \theta + (2/r) \partial v/\partial \theta + S_{turb} + S_{mag}$
θ - energy	$\bar{C}_p\theta$	\bar{k}_{eff}/Pr	$-\nabla \cdot \mathbf{q}'' + S_{turb}$
C_i - impurity	C_i	$\bar{\mu}_{eff}$	S_i
C_d - doping	C_d	$\bar{\mu}_{eff}$	S_d
k - kinetic energy	k	$\bar{\mu}_{eff}/\sigma_k$	$G - \bar{\rho}\epsilon$
ϵ - dissipation	ϵ	$\bar{\mu}_{eff}/\sigma_\epsilon$	$C_1 G\epsilon/k - C_2 \bar{\rho}\epsilon^2/k$

⁺ The terms, S_{turb} and S_{mag} , refer to the source terms from turbulence, magnetic forces. * (rw) swirl in θ direction for rotating systems. For nonrotating systems, $w=0$. C_i and C_d refer to the concentration of impurities and dopings, $\bar{\mu}_{eff}$ is the effective dimensionless viscosity, and so on.

The following scales have been used to non-dimensionalize the governing equations; length: b , velocity: ν_o/b , pressure: $\rho_o\nu_o^2/b^2$, time: b^2/ν_o , density: ρ_o , dynamics viscosity: μ_o , conductivity: k_o , specific heat: C_{po} , and temperature: $\theta = (T - T_\infty)/(T_h - T_\infty)$; where subscript 'o' refers to the gas properties at ambient temperature T_∞ . In Table 1, $\bar{\mu}_{eff}$ and \bar{k}_{eff} are the effective dimensionless viscosity and conductivity, respectively, and have both laminar and turbulent components.

2.2. Turbulence Model

For laminar flows, $\bar{\mu}_{i,eff} = \bar{\mu}_i$ and $\bar{k}_{i,eff} = \bar{k}_i$, and in the case of turbulent flows,

$$\bar{\mu}_{i,eff} = \bar{\mu}_i + C_\mu \bar{\rho} k^2 / \epsilon, \quad (0.2)$$

$$\bar{k}_{i,eff} = \bar{k}_i + C_\mu \bar{\rho} k^2 / \epsilon \cdot Pr_m / Pr_{turb}, \quad (0.3)$$

where Pr_{turb} is the turbulent Prandtl number.

The dimensionless turbulent kinetic energy k and its dissipation rate are obtained from the following conservation equations:

$$\frac{\partial \bar{\rho}_i k}{\partial t} + \nabla \cdot (\bar{\rho}_i \mathbf{u}_i k) = \nabla \cdot \left(\frac{\bar{\mu}_{i,eff}}{\sigma_k} \nabla k \right) + S_k, \quad (0.4)$$

$$\frac{\partial \bar{\rho}_i \epsilon}{\partial t} + \nabla \cdot (\bar{\rho}_i \mathbf{u}_i \epsilon) = \nabla \cdot \left(\frac{\bar{\mu}_{i,eff}}{\sigma_\epsilon} \nabla \epsilon \right) + S_\epsilon, \quad (0.5)$$

The source terms S_k and S_ϵ are defined as

$$S_k = \bar{\mu}_t \bar{G} - \bar{\rho} \epsilon \quad (0.6)$$

$$S_\epsilon = C_1 \bar{\mu}_t \frac{\epsilon}{k} \bar{G} - C_2 \bar{\rho} \frac{\epsilon^2}{k} \quad (0.7)$$

where \bar{G} is expressed as follows in the case of axisymmetric flows

$$\bar{G} = 2 \left[\left(\frac{\partial u}{\partial z} \right)^2 + \left(\frac{\partial v}{\partial r} \right)^2 + \left(\frac{v}{r} \right)^2 \right] + \left(\frac{\partial v}{\partial z} + \frac{\partial u}{\partial r} \right)^2 + \left(\frac{\partial w}{\partial z} \right)^2 + \left(\frac{\partial w}{\partial r} - \frac{w}{r} \right)^2. \quad (0.8)$$

Standard values for these constants are used in the simulation, and were obtained from the literature [9].

2.3. Solidification Interface and Free Surface

At the melt/solid interface, an energy balance must consider the solidification rate and any imposed pull rate (as in crystal growth), convection in the melt, conduction in the solid and release of heat of fusion. For solidification of a pure substance with a definite fusion temperature T_f , implying that the solid and liquid phases are separated by a sharp interface, the position of the solid/melt interface can be given by

$$\rho_s h_{sl} (U_{int,n} - U_s(t) \mathbf{e}_x \cdot \mathbf{n}) = k_s \frac{\partial T_s}{\partial n} - k_m \frac{\partial T_m}{\partial n}, \quad (0.9)$$

To obtain conditions at the melt/encapsulant and encapsulant/gas interfaces, we can assume the tangential stress at these interfaces to be zero and the normal stress exactly balanced by the externally applied stresses in the normal direction, which can be written as

$$[(-p\mathbf{I} + \tau)_i \cdot \mathbf{n}] \cdot \mathbf{n} - [(-p\mathbf{I} + \tau)_{i+1} \cdot \mathbf{n}] \cdot \mathbf{n} = \frac{2H}{BoFr} \mathbf{n}, \quad (0.10)$$

where \mathbf{t} and \mathbf{n} are tangential and normal unit vectors, H is the mean interface curvature, \mathbf{I} is the unit tensor, Bo and Fr are the dimensionless Bond and Froude numbers, respectively, and τ is the dimensionless stress tensor.

2.4. Moving Interface Tracking Scheme

The governing equations for melt and solid phases are solved iteratively and independently by invoking the quasi-steady assumption (within one time interval) for the solid/melt interface. A successive approximation is used to track the movement of the interface. The procedure is as follows:

1. Assume an initial solidification and free surface locations, and generate the initial grids.
2. Solve the governing equations for each phase based on the single domain system.
3. Move the solidification interface based on an energy balance and move the free surface based on a normal stress balance. Underrelaxation may be needed to control large variations in the interface shapes.
4. Regenerate the grids and return to step 2 until all equations and boundary conditions are satisfied.

2.5. Electric-Magnetic Field

Lorentz force is introduced into the momentum equation as a body force (source term), F_x and F_r in r and x -directions respectively and F_θ in θ -direction due to swirl velocity (rw).

$$\begin{aligned}
 F_x &= \frac{-Ha^2\sigma}{\sigma_m} b_r (b_r u - b_x v) . \\
 F_r &= \frac{Ha^2\sigma}{\sigma_m} b_x (b_r u - b_x v) . \\
 F_\theta &= -Ha^2 \left(b_x \frac{\partial \Psi_J}{\partial x} + b_r \frac{\partial \Psi_J}{\partial r} \right) .
 \end{aligned} \tag{0.11}$$

where Ha is the Hartman number, and $b_x = 1$ and $b_r = 0$ if an axial magnetic field (x -direction) is applied.

Electric Current Stream Fuction Equation:

The electric current stream function equation is solved instead of electric potential in this code. The primary advantage of using the stream function equation is the simplicity in implementation of boundary conditions. The boundary conditions for potential equation are much more complicated on curvilinear walls. However, this option is available if the user favors to solve the potential equation,

$$\frac{\partial}{\partial x} \left(\frac{\sigma_m}{\sigma} \frac{1}{r} \frac{\partial \Psi_J}{\partial x} \right) + \frac{\partial}{\partial r} \left(\frac{\sigma_m}{\sigma} \frac{1}{r} \frac{\partial \Psi_J}{\partial r} \right) = b_x \frac{\partial w}{\partial x} + b_r r \frac{\partial}{\partial r} \left(\frac{w}{r} \right). \quad (0.12)$$

The boundary condition of the electric current stream function is

$$\Psi_j = 0 \quad (0.13)$$

2.6. Application for Crystal Growth

A detailed description of conservation equations, boundary conditions and governing process parameters for high pressure crystal growth is presented in Appendix I.

3. OVERVIEW OF THE COMPUTER PROGRAM

As already mentioned, the program is divided into two parts: the invariant part and the user application part. The invariant part embodies the grid generation and the general numerical solution procedure, to be described in Chapters 4 and 5. A flow chart is presented in Fig. 1. The invariant part is shown by dashed lines.

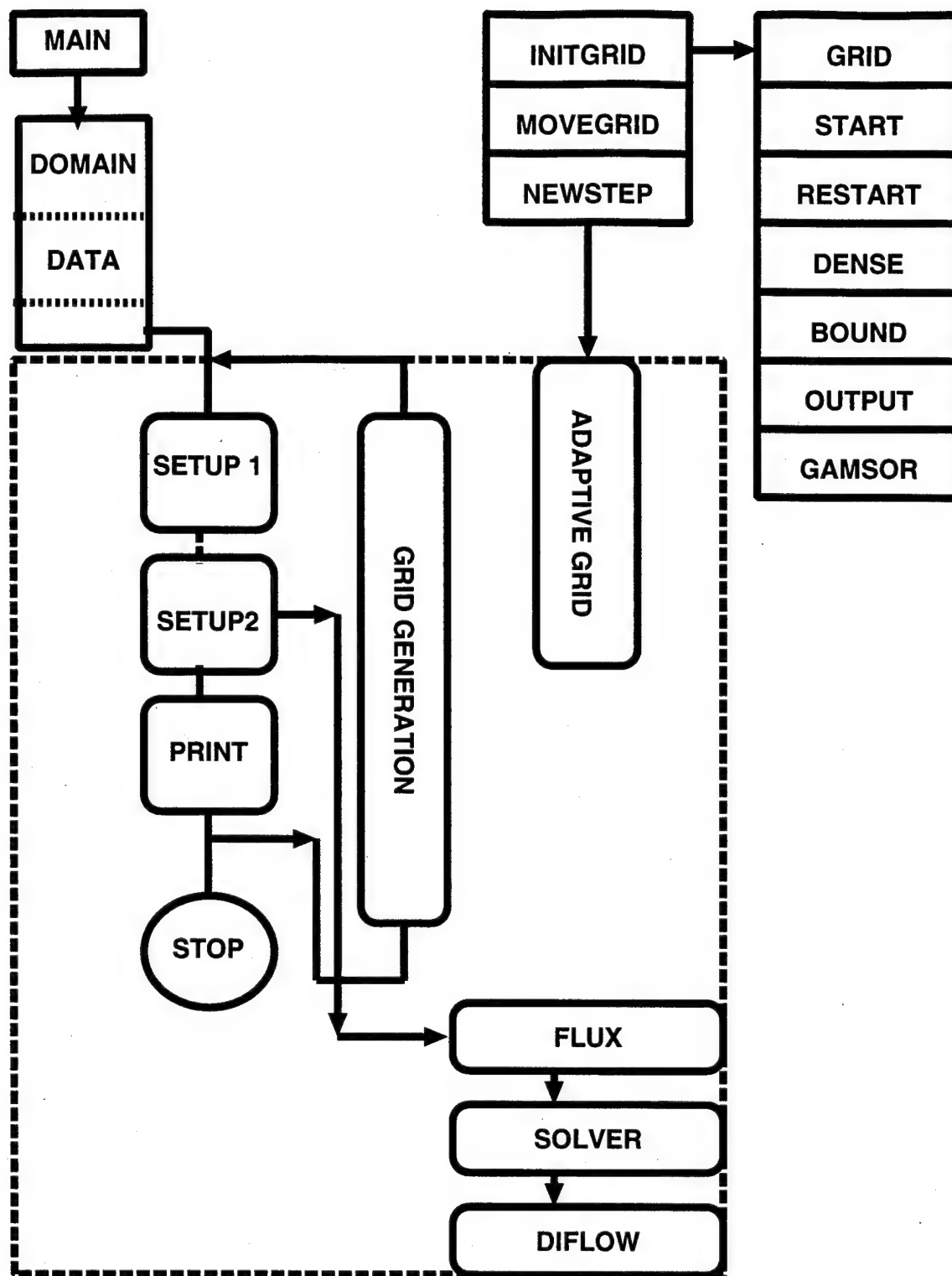


Figure 0.1: Flow diagram for MASTRAPP2d 1.0

4. MULTIZONE ADAPTIVE GRID GENERATION

4.1. General Formulation

Numerical grid generation is an algorithmic procedure that distributes the computational nodes over a physical field in an orderly fashion such that the physical phenomena in the entire field can be calculated more accurately and efficiently. Implied in this general definition is that arbitrarily-shaped domain boundaries coincide with grid lines of constant indices. In other words, numerical grid generators, in general, discretize the physical domain with natural or boundary-fitted coordinates. This attribute, which has been used to refer to some of the first generation of elliptic grid generators specifically, is now considered to be a generic characteristic of the numerical grid generators.

Recent research efforts have been mainly focused on generation of grid systems with special characteristics; namely, adaptivity and multizoning. The grid generation technique used in this work has both of these characteristics; therefore, a description of these features are provided here, before the grid generation technique is explained in detail.

In the context of numerical grid generation, adaptive or dynamically adaptive characteristic refers to the capability of the grid generating algorithm to cluster and disperse the grid nodes automatically based on temporal and/or iterative development of the solutions. The grid distribution is readjusted dynamically to concentrate the points in regions of large variations of a dependent variable(s), without reliance on the prior knowledge of the locations of such variations. Multizone grid generation is employed in situations when the problem domain is composed of regions/zones with vastly different physical properties and/or internal moving boundaries (*e.g.*, problems involving phase-change, solid combustion, heterogeneous chemical reaction, etc.). Under these conditions, it is desirable to generate the grid system for different zones separately such that, the grid lines with constant indices coincide with the internal boundaries separating these zones. This can facilitate the enforcement of internal boundary conditions, implementation of their movement which is usually governed by an auxiliary nonlinear equation(s), and application of different physical properties to the adjacent zones.

There are several competing, and some times conflicting, considerations involved in generating a grid system over which a convection-diffusion problem is to be solved numerically. The grid points must be concentrated in some regions, and yet, no region can be allowed to be void of points. The grid distribution must retain a sufficient degree of smoothness, and the grid must not become too skewed, or else the truncation error will increase. Numerical stability and convergence are other important considerations in formulating a grid generator.

Keeping the above requirements in mind, a robust grid generation technique has been developed based on the variational method, that minimizes an integral function

which is a measure of grid characteristics; namely the smoothness, I_s , orthogonality, I_o , weighted cell area, I_w , and inertia, I_m of the grids. Viewing the grid generation as the mapping $x(\xi, \eta)$, $y(\xi, \eta)$ in which the points corresponding to integer values of ξ and η are the grid nodes $x(i, j)$, $y(i, j)$ these integrals may be written as

$$I_s = \iint \left(\frac{x_\xi^2 + x_\eta^2 + y_\xi^2 + y_\eta^2}{Ja} \right) d\xi d\eta , \quad (0.14)$$

$$I_o = \iint G (x_\xi x_\eta + y_\xi y_\eta)^2 d\xi d\eta , \quad (0.15)$$

$$I_w = \iint W Ja^2 d\xi d\eta , \quad (0.16)$$

$$I_m = \iint M(\xi, \eta) (u_g^2 + v_g^2) d\xi d\eta , \quad (0.17)$$

where, W and G are weight functions that are to be specified to control grid volumes (area) and orthogonality, respectively; M is the inertia coefficient; u_g , v_g are the grid speeds at the present or last time step; and Ja is the Jacobian of the mapping, $Ja = x_\xi y_\eta - x_\eta y_\xi$, with subscripts denoting the variables with respect to which the partial differentiation is performed.

A grid generator may be made part of an algorithm to adapt the grid distribution to data generated by the solution of the finite difference equations by using an appropriate weight function $W(x, y)$ (e.g., some measure of the solution variation or error); resulting in a finer grid where the weight is large. The formulation of Brackbill and Saltzman [10] did not include an orthogonality weighting function since $G(x, y)$ was taken as unity. The choices of the weighting functions W and G are generally problem dependent as will be discussed later.

The grid generation system is formed by minimizing a weighted sum of integrals (14) to (17),

$$I = I_s + \bar{\lambda}_o(N/L)^4 I_o + \bar{\lambda}_w(N/L)^4 I_w + \bar{\lambda}_m(N/L)^4 I_m = \iint F d\xi d\eta , \quad (0.18)$$

where N is the characteristic number of grid nodes, L is the characteristic length of the physical domain, $\bar{\lambda}$'s are positive constants between 1 and 100, and F is the kernel of the function which is also referred to as the overall "performance function" of the optimization problem. The Euler's equations for the variational problem of equation (18) form a system of partial differential equations from which the coordinates of grid nodes are calculated,

The Euler-Lagrange equations for the variational problem form a system of PDEs:

$$\left(\frac{\partial}{\partial x} - \frac{\partial}{\partial \xi} \frac{\partial}{\partial x_\xi} - \frac{\partial}{\partial \eta} \frac{\partial}{\partial x_\eta} \right) F = 0 ,$$

$$\left(\frac{\partial}{\partial y} - \frac{\partial}{\partial \xi} \frac{\partial}{\partial y_\xi} - \frac{\partial}{\partial \eta} \frac{\partial}{\partial y_\eta} \right) F = 0 . \quad (0.19)$$

Performing the indicated differentiation and collecting coefficients of the highest derivatives yield the following equations

$$b_1 x_{\xi\xi} + b_2 x_{\xi\eta} + b_3 x_{\eta\eta} + a_1 y_{\xi\xi} + a_2 y_{\xi\eta} + a_3 y_{\eta\eta} + d_1 - 2\lambda_m M(x - x_0) = 0 , \quad (0.20)$$

$$a_1 x_{\xi\xi} + a_2 x_{\xi\eta} + a_3 x_{\eta\eta} + c_1 y_{\xi\xi} + c_2 y_{\xi\eta} + c_3 y_{\eta\eta} + d_2 - 2\lambda_m M(y - y_0) = 0 , \quad (0.21)$$

where the coefficients a_i , b_i , c_i , and d_i are functions of the first derivatives of x and y , as well as of W and G and their derivatives, and are given by

$$a_i = a_{si} + 2W \lambda_w a_{wi} + G \lambda_o a_{oi} , \quad (0.22)$$

$$b_i = b_{si} + 2W \lambda_w b_{wi} + G \lambda_o b_{oi} , \quad (0.23)$$

$$c_i = c_{si} + 2W \lambda_w c_{wi} + G \lambda_o c_{oi} , \quad (0.24)$$

$$d_1 = \lambda_w \cdot [Ja \cdot (y_\eta W_\xi - y_\xi W_\eta)] + \lambda_o \cdot [(y_\eta G_\xi - y_\xi G_\eta) \cdot (x_\xi x_\eta + y_\xi y_\eta)^2 / 2Ja - (x_\xi G_\eta + x_\eta G_\xi) \cdot (x_\xi x_\eta + y_\xi y_\eta)] \quad (0.25)$$

$$d_2 = \lambda_w \cdot [Ja \cdot (x_\xi W_\eta - x_\eta W_\xi)] + \lambda_o \cdot [(x_\xi G_\eta - x_\eta G_\xi) \cdot (x_\xi x_\eta + y_\xi y_\eta)^2 / 2Ja - (y_\xi G_\eta + y_\eta G_\xi) \cdot (x_\xi x_\eta + y_\xi y_\eta)] \quad (0.26)$$

The coefficients appearing in equations (20) and (21) are given in Table 2.

A proper choice of the weighting function $W(x, y)$ brings adaptivity to the grid system with the solution development. By using $G = 1$, orthogonality of the larger grid cells is favored over the smaller ones. It has been found that with $G = Ja^{-2}$ or $G = W$ the orthogonalization effect would equally apply to all cells. In a moving boundary problem, although Dirichlet boundary conditions may exist for some or all of the dependent variables, the motion of the boundary is usually governed by an auxiliary nonlinear equation which involves fluxes of one or more of the dependent variables. Therefore, a more orthogonal grid near a moving boundary is conducive to more accurate calculations of the interface fluxes, and consequently, smaller errors in the evaluation of the boundary movement. The multiplier $G(x, y)$ may be used for this purpose, or it may be made a function of the grid cell area (volume) Ja , to relate the smoothness and orthogonality characteristics more dynamically, for example, $G = W^2$.

The grid characteristic function I_v attracts the grid nodes to a specified region x_0 . Here, x_0 may assume the role of a given mesh in which case it becomes a function of the

Table 0.2: Coefficients of Euler Equations (20-21)

$a_{s1} = -AX$	$b_{s1} = BX$	$c_{s1} = CX$
$a_{s2} = 2AY$	$b_{s2} = -2BY$	$c_{s2} = -2CY$
$a_{s3} = -AZ$	$b_{s3} = BZ$	$c_{s3} = CZ$
$a_{o1} = x_\eta y_\eta$	$b_{o1} = x_\eta^2$	$c_{o1} = y_\eta^2$
$a_{o2} = x_\xi y_\eta + x_\eta y_\xi$	$b_{o2} = 2(x_\xi x_\eta + y_\xi y_\eta)$	$c_{o2} = 2(x_\xi x_\eta + 2y_\xi y_\eta)$
$a_{o3} = x_\xi y_\xi$	$b_{o3} = x_\xi^2$	$c_{o3} = y_\xi^2$
$a_{w1} = -x_\eta y_\eta$	$b_{w1} = y_\eta^2$	$c_{w1} = x_\eta^2$
$a_{w2} = x_\xi y_\eta + x_\eta y_\xi$	$b_{w2} = -2y_\xi y_\eta$	$c_{w2} = -2x_\xi x_\eta$
$a_{w3} = -x_\xi y_\xi$	$b_{w3} = y_\xi^2$	$c_{w3} = x_\xi^2$
$A = x_\xi y_\xi + x_\eta y_\eta$	$B = y_\xi^2 + y_\eta^2$	$C = x_\xi^2 + x_\eta^2$
$X = (x_\eta^2 + y_\eta^2) / Ja^3$	$Y = (x_\xi x_\eta + y_\xi y_\eta) / Ja^3$	$Z = (x_\xi^2 + y_\xi^2) / Ja^3$

spatial location rather than the eventual grid point counters ξ and η . In the region of large $M(\xi, \eta)$, the diagonal dominance is intensified. In the limit, the system approaches a simple diagonal form and this causes each current grid point $\mathbf{x}(\xi, \eta)$ to approach the corresponding specified grid point $\mathbf{x0}(\xi, \eta)$. The attractor function M may be selectively chosen such that the specified grid is approached at a nonuniform rate.

4.2. Boundary Node Distribution

The required boundary conditions of the grid generation problem formulated above are position of the grid points along the ordinary boundaries (Dirichlet boundary condition), and zero normal derivative (Neumann boundary condition) along the symmetrical ones. If special features of the boundary or solution there need resolving, the boundary node distribution can be controlled by adding boundary smoothness and concentration to equation (18).

The position of the boundary nodes are calculated using the 1-D adaptive grid generator. With the total number of points along a boundary segment c_1 ($\eta = \eta_b$) given, the boundary curve is parameterized with the arc length s such that $x = x(s)$ and $y = y(s)$ where $s = s(\xi)$ coincides with $\eta = \eta_b$.

The grid redistribution along the boundary is determined by minimizing

$$I = I_s + \lambda_w I_w + \lambda_v I_v, \quad (0.27)$$

To preserve the shape of the moving boundary along which the grid points change, an accurate curve fitting procedure needs to be used. Euler's equation corresponding to the

variational problems (27) is

$$\frac{\partial}{\partial s} - \frac{\partial}{\partial \xi} \frac{\partial}{\partial s_\xi} [s_\xi^{-1} + \lambda_w w(s) s_\xi^2 + \lambda_v V(\xi)(s-r)^2] = 0 , \quad (0.28)$$

or

$$[1.0 + \lambda_v w s_\xi^3] s_{\xi\xi} + 0.5 \lambda_w w s s_\xi^5 = \lambda_v s_\xi^3 V(\xi)(s-r) . \quad (0.29)$$

This equation is highly nonlinear and does not render converged solution easily. For numerical convenience, $\lambda'_w = \lambda_w s_\xi^3$ and $V' = s_\xi^3 V$ are assumed. Equation (29) is then simplified to

$$(1.0 + \lambda'_w w) s_{\xi\xi} + 0.5 \lambda'_w w s_\xi s_\xi = \lambda_v V'(s-r) . \quad (0.30)$$

4.3. Adaptive Grid Generation for Internal Interfaces

A MAGG technique distributes a fixed number of grid points in the computational domain such that grid lines correspond to the interfaces between different zones. Implied in this definition is that while the grid distribution in different zones are allowed to adjust to the development of the solution and movement of the internal boundaries, the interfaces between the zones are preserved (i.e., not defined by the grid generator). In other words, the grid points are only permitted to move along these interfaces. A methodology is employed in MAGG as follows. This grid generation routine is formulated via the variational problem equation (19) for the entire domain, with the exception of the zonal interfaces along which the grid distribution is obtained by the same 2-D variational problem (19) subject to constraints of the form

$$g_I \equiv g_I(x, y) = 0, \quad \text{for } I = I_1, I = I_2, \dots \quad \text{with } I_{min} < I_i < I_{max} , \quad (0.31)$$

where g_I 's are known real-valued functions with respect to arguments x and y which are implicit functions of ξ and η , and define the interfaces for constant η_I values. The above constrained optimization problems are converted to unconstrained ones by introducing Lagrange multipliers Λ_I to form augmented functionals

$$I = \int \int (F + \Lambda_I g_I) d\xi d\eta . \quad (0.32)$$

Applying the Euler-Lagrange equation yields the following equations:

$$R_x - \Lambda_I \frac{\partial g_I}{\partial x} = 0 , \quad (0.33)$$

$$R_y - \Lambda_I \frac{\partial g_I}{\partial y} = 0 , \quad (0.34)$$

where R_x and R_y are the left hand sides of equations (20) and (21). Equation (32) along with the constraint (31) provide the necessary conditions for finding the grid distribution $(x(\xi, \eta_I), y(\xi, \eta_I))$ and the Lagrange multipliers Λ_I . After eliminating Λ_I between (33) and (34), the grid distribution along an internal boundary $\eta = \eta_I$ is the solution of the system of equations comprising of (31) and

$$\frac{\partial g_I}{\partial y} R_x - \frac{\partial g_I}{\partial x} R_y = 0 . \quad (0.35)$$

The interface position function and its derivatives are determined using an accurate curve fitting procedure in order to preserve its shape, while the grid points move along the interface.

The MAGG technique formulated here is more efficient and has better characteristics than the previous ones. This is mainly due to the direct and dynamic link between the zonal and interfacial grid generation routines that is provided by the presence of second order derivatives (e.g., $x_{\eta\eta}$ and $y_{\eta\eta}$) in this formulation. The finite difference approximation of Euler's equations are formed and solved by SOR method to determine the coordinates of the grid points.

5. CURVILINEAR FINITE VOLUME DISCRETIZATION

5.1. General Formulation

Computational analyses of transport phenomena in multiphase transport processes usually require that the field variables be calculated in an irregular domain with free and moving interfaces. This requires an innovative algorithm that permits: (a) true representation of free boundaries (with options for variable pressure boundary conditions), and (b) accurate treatment of moving boundaries (boundary relaxation technique for nonlinear auxiliary equations defining the boundary motions).

Conservation equations can be written in the following general form (equation 1):

$$\frac{\partial}{\partial t}(r^n \rho \phi) + \frac{\partial}{\partial x}(r^n u \rho \phi) + \frac{\partial}{\partial r}(r^n v \rho \phi) = \frac{\partial}{\partial x}(r^n \Gamma \frac{\partial \phi}{\partial x}) + \frac{\partial}{\partial r}(r^n \Gamma \frac{\partial \phi}{\partial r}) + r^n S . \quad (0.36)$$

where ϕ is the generalized variable, S is the volumetric source, and Γ is the diffusion coefficient. The index n is set to zero if a Cartesian coordinate system is used, and to unity if the polar cylindrical coordinates are employed.

The conservation equation can be integrated over each finite volume in the physical domain as,

$$\frac{\partial}{\partial t} \int_V (r^n \rho \phi) dV + \oint_s \mathbf{J} \cdot d\mathbf{s} = \int_V (r^n S) dV , \quad (0.37)$$

where \mathbf{J} includes both the diffusion and convection fluxes. The finite volume method can handle any type of mesh except that the difficulties are associated with how to calculate the surface values of these fluxes as well as how to treat the velocity and pressure coupling if a fluid flow problem is considered. Two type of grids are generally used in a finite volume method; structured "finite difference" mesh and unstructured "finite element" mesh. Structured grids are simpler and more advantageous (less memory and better matrix structure) than the unstructured grids in developing a solution procedure. However, as is well-known, it is far more difficult to construct a structured mesh for an irregular domain. The MAGG provides a great advantage in this respect, and allows an easy implementation of structured grids for an irregular geometry.

The advantages of CFV are that a unified code can be developed for different kinds of geometries and modifications in the physical process models can be easily implemented in the computer algorithm. The grids used here are a structured trapezoidal mesh, as shown in Fig. 2.

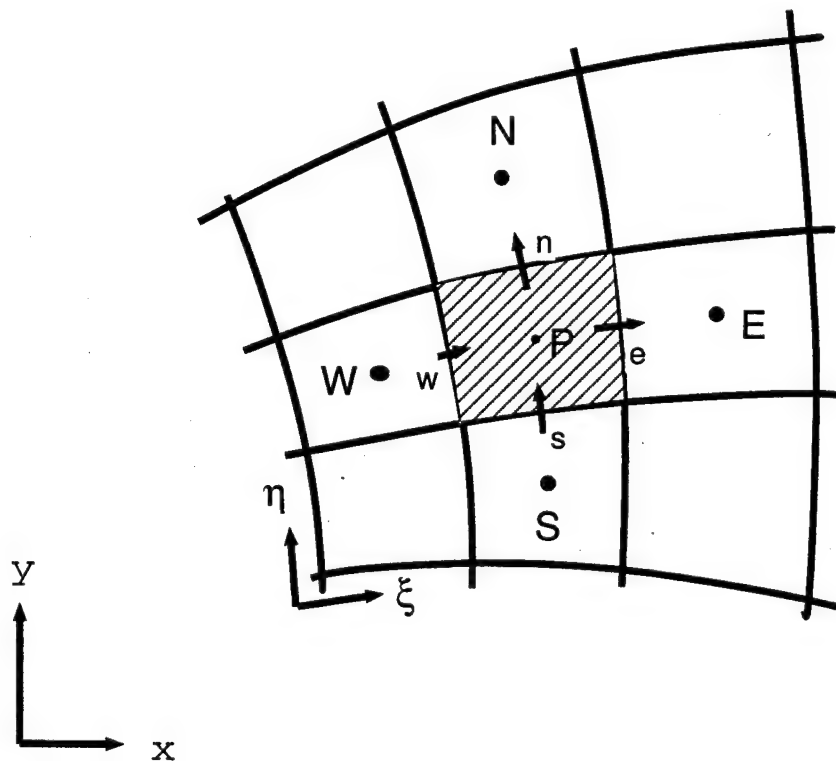


Figure 0.2: Curvilinear finite volume grid arrangement.

For a typical primary node P , the conservation equation in a generalized coordinate

system (ξ, η) can be written as,

$$\frac{(r^n Ja \rho \phi - r_o^n Ja^o \rho^o \phi^o)_P \Delta \xi \Delta \eta}{\Delta t} + (\alpha_\xi J_\xi - \beta_\xi J_\eta)_e \Delta \eta - (\alpha_\xi J_\xi - \beta_\xi J_\eta)_w \Delta \eta + (\alpha_\eta J_\eta - \beta_\eta J_\xi)_n \Delta \xi - (\alpha_\eta J_\eta - \beta_\eta J_\xi)_s \Delta \xi = (r^n Ja \hat{S})_P \Delta \xi \Delta \eta, \quad (0.38)$$

$$h_\xi = \left[\left(\frac{\partial x}{\partial \xi} \right)^2 + \left(\frac{\partial y}{\partial \xi} \right)^2 \right]^{1/2}, \quad h_\eta = \left[\left(\frac{\partial x}{\partial \eta} \right)^2 + \left(\frac{\partial y}{\partial \eta} \right)^2 \right]^{1/2}, \quad (0.39)$$

$$\alpha_\xi = r^n h_\xi h_\eta^2 / Ja, \quad \alpha_\eta = r^n h_\eta h_\xi^2 / Ja, \quad (0.40)$$

$$\beta_\xi = (\vec{e}_\xi \cdot \vec{e}_\eta) r^n h_\xi h_\eta^2 / Ja, \quad \beta_\eta = (\vec{e}_\xi \cdot \vec{e}_\eta) r^n h_\eta h_\xi^2 / Ja, \quad (0.41)$$

and

$$\vec{e}_\xi = \left[\frac{\partial x}{\partial \xi} \vec{e}_x + \frac{\partial y}{\partial \xi} \vec{e}_y \right] / h_\xi, \quad \vec{e}_\eta = \left[\frac{\partial x}{\partial \eta} \vec{e}_x + \frac{\partial y}{\partial \eta} \vec{e}_y \right] / h_\eta. \quad (0.42)$$

$$J_\xi = \rho u_\xi \phi - \frac{\Gamma}{h_\xi} \frac{\partial \phi}{\partial \xi}, \quad J_\eta = \rho u_\eta \phi - \frac{\Gamma}{h_\eta} \frac{\partial \phi}{\partial \eta}. \quad (0.43)$$

The above equation represents an overall conservation of ϕ in a finite volume in terms of its fluxes at the auxiliary nodes, and is referred to as the flux discretization equation. The source term \hat{S} is the original term $S(\xi, \eta)$ plus the terms consisting of the grid velocity components

$$r^n Ja \hat{S} = r^n Ja S + \frac{\partial}{\partial \xi}(\rho r^n u_g \phi) + \frac{\partial}{\partial \eta}(\rho r^n v_g \phi). \quad (0.44)$$

where the grid velocities are defined as

$$u_g = \frac{\partial y}{\partial \eta} \frac{\partial x}{\partial t} - \frac{\partial x}{\partial \eta} \frac{\partial y}{\partial t}, \quad v_g = \frac{\partial x}{\partial \xi} \frac{\partial y}{\partial t} - \frac{\partial y}{\partial \xi} \frac{\partial x}{\partial t}. \quad (0.45)$$

It is important to note some of the properties of coefficients α and β in Equation (38). Both of these coefficients have units of area, and while α 's are always positive; β 's may be positive, negative or zero. The absolute magnitude of β_ξ is always less than α_ξ ; and if the coordinates (ξ, η) are orthogonal, then $\beta_\xi = 0$, and $\alpha_\xi = h_\eta$. These coefficients can be conceptually regarded as areas, and in view of their properties, α 's are referred to as the primary areas, and β 's are called the secondary areas. The subscript ξ in these coefficients denote that they are corresponding to a $\xi = \text{constant}$ line. With this interpretation, the flux across a finite-volume face may be thought of to be composed of

two components. For example, on the face of a finite-volume east of P (denoted by e, and corresponding to a $\xi = \xi_1$), the primary flux is J_ξ and the secondary flux is J_η . This interpretation of the flux discretization equation signifies the effect of the orthogonality of the grid system, as all the secondary fluxes vanish for an orthogonal grid.

A discretized formulation and solution procedure is implemented by using the finite volume approach in general curvilinear coordinates, and the convective and diffusive fluxes are discretized in the physical domain.

5.2. Discretization Formulation

To obtain the finite difference equations in terms of ϕ at the centers of finite volumes P, the *Power-Law* interpolation profile of Patankar [8] is used. The final expression can be written as

$$a_P \phi_P = a_E \phi_E + a_W \phi_W + a_N \phi_N + a_S \phi_S + b, \quad (0.46)$$

where

$$\begin{aligned} a_E &= D_e A(|P_e|) \alpha_{\xi e} \Delta \eta + \max[0, -F_e], \\ a_W &= D_w A(|P_w|) \alpha_{\xi w} \Delta \eta + \max[0, F_w], \\ a_N &= D_n A(|P_n|) \alpha_{\xi n} \Delta \xi + \max[0, -F_n], \\ a_S &= D_s A(|P_s|) \alpha_{\xi s} \Delta \xi + \max[0, F_s], \\ a_P^0 &= \rho^0 (Ja)_P^0 / \Delta t, \end{aligned} \quad (0.47)$$

$$a_P = a_E + a_W + a_N + a_S + a_P^0 - S_P Ja \Delta \xi \Delta \eta. \quad (0.48)$$

The remaining terms from the substitution are included in constant b . In order to identify the origins of these terms, b is expressed as

$$b = b_s + b_{no}, \quad (0.49)$$

where

$$b_s = a_P^0 \phi_P^0 + S_c Ja \Delta \xi \Delta \eta, \quad (0.50)$$

$$\begin{aligned} b_{no} &= [(\beta_\xi J_\eta)_e - (\beta_\xi J_\eta)_w] \Delta \eta + [(\beta_\eta J_\xi)_n - (\beta_\eta J_\xi)_s] \Delta \xi \\ &\quad - \phi_P [(\rho u_\xi \alpha_\xi)_e - (\rho u_\xi \alpha_\xi)_w] \Delta \eta \\ &\quad - \phi_P [(\rho u_\eta \alpha_\eta)_n - (\rho u_\eta \alpha_\eta)_s] \Delta \xi, \end{aligned} \quad (0.51)$$

Here b_s contains the contribution from the original volumetric source S , and b_{no} contains the contributions which do not appear in the orthogonal coordinate system, so

the subscript *NO* is used to indicate the origin of these terms -- the non-orthogonality of the coordinate system.

In equation (47), D_e is the diffusion conductance,

$$D_e = \Gamma_e / h_{\xi e}, F_e = (\rho \tilde{u}_{\xi})_e, P_e = F_e / D_e, \Gamma_e = \bar{P}E / (\bar{P}e / \Gamma_P + \bar{e}E / \Gamma_E), \quad (0.52)$$

and the function $A(P_e)$ is defined by Patankar (1980) as

$$A(P_e) = \max[0, (1 - 0.1|P_e|)^5] . \quad (0.53)$$

The other coefficients in positions, w, n, s are similar to equation (52).

5.3. Momentum Equation and Momentum Interpolation Method

From the discretization of the momentum equations, the Cartesian velocity components can be written as follows (with the underrelaxation expressed explicitly):

$$u_P = (H_u)_P + (1 - \omega)u_P^{n-1} - (D_{u\xi})_P(dp/d\xi)_P - (D_{u\eta})_P(dp/d\eta)_P, \quad (0.54)$$

$$v_P = (H_v)_P + (1 - \omega)v_P^{n-1} - (D_{v\xi})_P(dp/d\xi)_P - (D_{v\eta})_P(dp/d\eta)_P, \quad (0.55)$$

where

$$H_u = \frac{\omega (\sum_{nb} a_{nb}^u u_{nb} + b_u)}{a_P^u}, \quad H_v = \frac{\omega (\sum_{nb} a_{nb}^v v_{nb} + b_v)}{a_P^v}, \quad (0.56)$$

$$D_{u\xi} = \frac{\omega}{a_P^u} \frac{\partial y}{\partial \eta}, \quad D_{u\eta} = -\frac{\omega}{a_P^u} \frac{\partial y}{\partial \xi}, \quad D_{v\xi} = -\frac{\omega}{a_P^v} \frac{\partial x}{\partial \eta}, \quad D_{v\eta} = \frac{\omega}{a_P^v} \frac{\partial x}{\partial \xi}. \quad (0.57)$$

In these equations, ω is the underrelaxation factor and the superscript (n-1) denotes the previous iteration level.

Before presenting the momentum interpolation formulation, the linear interpolation is reviewed through which the velocity at a control volume face may be expressed as,

$$u_e = f_e^- u_E + (1 - f_e^-) u_P. \quad (0.58)$$

where $f_e^- = \delta x_e^- / \delta x_e$.

The momentum interpolation scheme assumes a linear variation between the nodes only for the first part of H_u in equation (54) and (55). The quantity $1/a_P^u$ and the pressure difference across the control volume are written directly as the difference of the nodal values of p_E and p_P . The momentum equations for Cartesian velocity components at the control volume face locations can then be written as,

$$\begin{aligned} u_e &= (H_u)_e - (D_{u\xi})_e(dp/d\xi)_e - (D_{u\eta})_e(dp/d\eta)_e + (1 - \omega)u_e^{n-1} , \\ v_e &= (H_v)_e - (D_{v\xi})_e(dp/d\xi)_e - (D_{v\eta})_e(dp/d\eta)_e + (1 - \omega)v_e^{n-1} , \end{aligned} \quad (0.59)$$

and

$$\begin{aligned} u_n &= (H_u)_n - (D_{u\xi})_n(dp/d\xi)_n - (D_{u\eta})_n(dp/d\eta)_n + (1 - \omega)u_n^{n-1} , \\ v_n &= (H_v)_n - (D_{v\xi})_n(dp/d\xi)_n - (D_{v\eta})_n(dp/d\eta)_n + (1 - \omega)v_n^{n-1} . \end{aligned} \quad (0.60)$$

In the scheme used in this work, these control volume face Cartesian velocity components are obtained through interpolation of the momentum equations for the neighboring control volume centered Cartesian velocity components. The following assumptions are introduced to evaluate control volume face velocities, for u_e at the east face:

$$\frac{1}{(a_P^u)_e} = \frac{f_e^-}{(a_P^u)_E} + \frac{(1 - f_e^-)}{(a_P^u)_P} , (H_u)_e = f_e^-(H_u)_E + (1 - f_e^-)(H_u)_P . \quad (0.61)$$

Similar formulation can be obtained and used for the evaluation of the other face velocities. It needs to be mentioned here that in u_e (equation 59), $u_e^{n-1} \neq f_e^-u_E^{n-1} + (1 - f_e^-)u_P^{n-1}$.

The momentum equations for the covariant velocity components at the control volume face are obtained through algebraic manipulation of the momentum equations to yield

$$\begin{aligned} (u_\xi)_e &= (H_\xi)_e + (D_\xi)_e(p_P - p_E) + (1 - \omega)(u_\xi^{n-1})_e , \\ (u_\eta)_n &= (H_\eta)_n + (D_\eta)_n(p_P - p_N) + (1 - \omega)(u_\eta^{n-1})_n , \end{aligned} \quad (0.62)$$

where

$$H_\xi = \left(\frac{\partial x}{\partial \xi} H_u + \frac{\partial y}{\partial \xi} H_v \right) / h_\xi , H_\eta = \left(\frac{\partial x}{\partial \eta} H_u + \frac{\partial y}{\partial \eta} H_v \right) / h_\eta , \quad (0.63)$$

and

$$D_\xi = \left(\frac{\partial x}{\partial \xi} D_{u\xi} + \frac{\partial y}{\partial \xi} D_{v\xi} \right) / h_\xi , D_\eta = \left(\frac{\partial x}{\partial \eta} D_{u\xi} + \frac{\partial y}{\partial \eta} D_{v\xi} \right) / h_\eta . \quad (0.64)$$

5.4. Treatment of Pressure-Velocity Coupling

In the present study, the coupling between the continuity and the momentum equations is solved using the SIMPLER algorithm. The integrated continuity equation for a control volume around a grid point P can be written as

$$(\rho U)_e - (\rho U)_w + (\rho V)_n - (\rho V)_s = 0 , \quad (0.65)$$

This can be expressed in terms of the covariant velocity components as follows:

$$(\rho u_\xi \alpha_\xi)_e - (\rho u_\xi \alpha_\xi)_w + (\rho u_\eta \alpha_\eta)_n - (\rho u_\eta \alpha_\eta)_s = b_{no} , \quad (0.66)$$

where b_{no} is a source term due to the nonorthogonality of the grid system, and can be expressed as

$$b_{no} = (\rho u_\eta \beta_\xi)_e - (\rho u_\eta \beta_\xi)_w + (\rho u_\xi \beta_\eta)_n - (\rho u_\xi \beta_\eta)_s . \quad (0.67)$$

The velocity components that are needed for evaluation of b_{no} are oriented along the control-volume faces. The non-orthogonal mass source terms are obtained by averaging the corresponding covariant velocity components at the neighboring auxiliary points and are treated in an explicit manner.

5.5. Pressure Correction Equation

The velocity components u_ξ and u_η obtained from the solution of momentum equations will generally not satisfy the mass conservation unless the pressure field is correct. These imperfect velocities are denoted by u_ξ^* and u_η^* . The velocity correction equation can be obtained by u_ξ equation subtracted from u_ξ^* as

$$(\Delta u_\xi)_e = (D_\xi)_e(p_{P'} - p_{E'}) , \quad (0.68)$$

$$(\Delta u_\eta)_n = (D_\eta)_n(p_{P'} - p_{N'}) , \quad (0.69)$$

where p' is the pressure correction. The continuity equation can now be written as

$$a_P p_{P'} = \sum a_{nb} p_{nb'} + b_c + b_{no} , \quad (0.70)$$

where

$$b_c = (\rho u_\xi \alpha_\xi)_w^* - (\rho u_\xi \alpha_\xi)_e^* + (\rho u_\eta \alpha_\eta)_s^* - (\rho u_\eta \alpha_\eta)_n^* , \quad (0.71)$$

where the source term b_{no} should be evaluated from equation (67) using a continuity-satisfying velocity field from the previous iteration. Such a practice exhibits a much better convergence behavior compared to a method in which the currently available imperfect velocities are used to calculate these terms. The pressure correction equation is solved three or four times with updated source terms.

5.6. Pressure Equation

The steps in the derivation of the pressure equation are similar to those for the pressure correction outlined previously. The only difference is that the starred velocities used earlier are replaced by the pseudo-velocities, defined as,

$$\hat{u}_\xi = H_\xi + (1 - \omega)u_\xi^{n-1} , \quad (0.72)$$

$$\hat{u}_\eta = H_\eta + (1 - \omega)u_\eta^{n-1} , \quad (0.73)$$

therefore, the source term b_c in the pressure equation is calculated using the pseudo-velocities. However, the source term b_{no} should still be based on the actual velocities

5.7. Solution Procedure

The solution procedure for the fluid flow calculations in general curvilinear coordinate system is basically similar to the SIMPLER algorithm which consists of solving the pressure equation to obtain pressure field and solving the pressure-correction equation only to correct velocities, but it becomes more complicated here because velocity directions are continually changed along the coordinate lines. A non-staggered grid layout is used and the sequence of operations are as follows:

- Start with guessed velocity field.
- Calculate the coefficients for the x-direction and y-direction momentum equations and hence calculate $(\rho u_{\xi} \alpha_{\xi})_e$, $(\rho u_{\xi} \alpha_{\xi})_w$, $(\rho u_{\eta} \alpha_{\eta})_n$, $(\rho u_{\eta} \alpha_{\eta})_s$, from \hat{u}_{ξ} and \hat{u}_{η} equations (72) and (73).
- Calculate the coefficients for the pressure equation and solve the pressure equation, similar to equation (70), to obtain the pressure p^* , where * refers to the value related to \hat{u}_{ξ} and \hat{u}_{η} .
- Use the latest pressure P^* to correct interface mass fluxes using equations such as

$$(\rho u_{\xi} \alpha_{\xi})_e = (\rho \hat{u}_{\xi} \alpha_{\xi})_e + (\rho D_{\xi} \alpha_{\xi})_e (p_P^* - p_E^*) \quad (0.74)$$

Use the p^* field to obtain the pressure at the control volume faces by interpolation. Solve both x-direction and y-direction momentum equations, equation (54) and (55), to obtain the velocities u^* and v^* .

- Use the new u^* , v^* fields, repeat the momentum interpolation procedure, obtain the mass fluxes $(\rho u_{\xi} \alpha_{\xi})^*$ and $(\rho u_{\eta} \alpha_{\eta})^*$ at the interfaces. Calculate the coefficients for the pressure-correction equation. Solve the pressure-correction equations (70) to obtain the p' field.
- Use p' to correct the interface mass fluxes by using equations such as

$$(\rho u_{\xi} \alpha_{\xi})_e = (\rho u_{\xi} \alpha_{\xi})_e^* + (\rho D_{\xi} \alpha_{\xi})_e (p_P' - p_E') , \quad (0.75)$$

linear interpolate p' field to obtain p' at the control-volume face. Correct the velocities u^* , v^* at the primary nodes by the use of equation as follow

$$u_P = u_P^* + (D_{u\xi})_P (p_w' - p_e') + (D_{u\eta})_P (p_s' - p_n') , \quad (0.76)$$

$$v_P = v_P^* + (D_{v\xi})_P (p_w' - p_e') + (D_{v\eta})_P (p_s' - p_n') . \quad (0.77)$$

- Return to step (2) and repeat until convergence.

5.8. Treatment of Multistep and Multizone Problems

In the numerical solution of the transient flow problems, the fluid variables are calculated at a finite number of coordinates, and the flow equations are approximated by finite differences, which are then marched in time. The accuracy of the difference equations

depends on the fineness of the mesh. As importantly, the accuracy of the solution depends on the resolution of the flow gradients. If the flow gradients are large, the absolute error in the difference approximation to derivatives will be large. When the number of mesh points is fixed, a greater overall accuracy can often be obtained by concentrating the mesh points where gradients are strong and dispersing them where gradients are weak. In addition, the mesh should maintain sufficient smoothness to avoid instability of the solution and satisfy the conditions that were discussed earlier.

By choosing an appropriately defined weighting function, the mesh generator can be made part of an algorithm to adapt a computational mesh dynamically to the data generated by the solution of the finite difference equations. The weighting function must depend on the data in such a way that numerical errors are reduced.

One of the choices of weighting function is

$$w = \omega \left(\frac{1}{\phi} \nabla \phi \right)^4 + (1 - \omega) w_{geom} . \quad (0.78)$$

where ϕ is the dependent variable that is being solved on the grid, and the w_{geom} is the weighting function based on the geometric considerations of the domain. The weighting function calculated from the data is smoothened to spread the influence of a single data point over a region of the mesh, then w is scaled between prescribed maximum and minimum values.

For transient problems, both marching in time and boundary movements are required. Here, the current field values, the geometric coefficients, and interface position are solved simultaneously in an iterative fashion. At a given time $t + \Delta t$, a tentative new position of the interface, $F^n(t + \Delta t)$, is extrapolated from the positions of the interface at the two previous time steps t and $t - \Delta t$. Adaptive grid generation is invoked with the newly calculated weight function, and the geometric coefficients are updated. The governing equations are then solved, and the interface movement formulation using the current field values yields a corrected position $F^{n+1}(t + \Delta t)$ for the interface. If

$$|F^{n+1}(t + \Delta t) - F^n(t + \Delta t)| < \epsilon , \quad (0.79)$$

where ϵ is a small value, then an acceptable position is predicted, and the calculation proceeds to the next time step. Otherwise, the calculations are repeated for the interface position $F^{n+1}(t + \Delta t)$ until the above condition (79) is satisfied. Few iterations are needed in most cases. The major consequence of accounting for the movement of the grid and the implicit update of the interface is in the choice of the time step. The restrictions normally placed on the time step in an explicit scheme are strongly alleviated. In fact, large time steps can be used with no loss in accuracy, resulting in efficient calculations.

6. SUBROUTINES OF MASTRAPP2d 1.0

- main** The main subroutine provides information on the selection of the *demon*, iteration and time step, laminar or turbulent flow, initial or restart run, and the solution architecture. For example, run zone1 then zone3 then zone2 and set more iteration number between zone1 and zone3. This subroutine also arranges when and where the interface movement is permitted. This is the heart of the multiphase architecture of the algorithm.
- grid** This part belongs to the subroutine *user*. It defines the number of grids in each zone, length of the curve, and initial shape of the curve. *ib* is the number of points used to define the curve, and *bx*, *by* are the points used to define the curve.
- start** This part also belongs to the subroutine *user*. It initializes the logical variables, and defines relaxation values and iteration control parameters. Information on governing parameters, e.g., Reynolds and Grashof numbers, are supplied in this part. Initial field variables (all prime variables) are also defined here. The scale of nondimensionalization can be calculated here, if necessary. For example, *cfo* is the time scale. $cfo \times dtm$ (nondimensional time) becomes real time in seconds. If *init*=1, *restart* is called and initialization is skipped.
- restart** This part belongs to the subroutine *user*. It reads the variables used for the restart run.
- bound** This part belongs to the subroutine *user* and gives the flux boundary conditions. Boundary conditions for the prime variables are specified in *gamsor*.
- output** This part belongs to the subroutine *user*.
- dense** This part also belongs to the subroutine *user*. Turbulence viscosity is calculated here. The density variation can be given here, for example, $\rho = \rho(T)$. However, this code can not be used for strongly fluctuating density or highly compressible flows.
- gamsor** This part is the heart of the subroutine *user*. *Gamsor* calculates the main coefficients for various transport problems, via, diffusivity *GAM* and source term *S* in the governing equations, as well as the boundary conditions. For example, eight equations are solved which are labeled as *nf* (1 = u, 2 = v, 3 = p, 4 = pc, 5 = t, 6 = rw, 7 = tk, 8 = te) For each transport equation specified by an *nf*, there is an independent part for diffusivity, source term and boundary conditions. It should be noted that $gam(i,1)=0.0$ means the gradient is zero at wall $j=1$, although it

is straight forward to use $u(i,1)=u(i,2)$. However, The convergence rate is much more rapid for first treatment than the second one. Therefore, $gam(i,1)=0.0$ for zero gradient is recommended. This is also why the boundary condition is included in Gamsor. The source term is linearized as $CON + AP \times \phi$. AP is required to be a negative quantity. Patankar [8] elaborates on it.

initgrid This part belongs to the subroutine *imgrid*, and generates the initial grids xc , yc . The initial grids are optimized by the grid generation (call *adaptive*).

movegrid This part belongs to the subroutine *imgrid*, calculates new position of the interface and free surface and regenerates grids by calling *adaptive*. Equations for moving interfaces are solved here. It is heart of the moving interface solver.

initl This part belongs to the subroutine *setup*, and finds the initial guess for pressure at the interface of the control volume. It also calculates the initial guess for the flux quantities $\rho u_\xi, \rho u_\eta$.

setup1 This part belongs to the subroutine *setup*. *setup1* calculates all the geometric parameters needed for the model. It includes position (x,y) of primary nodes, h_ξ, h_η , Jacobian, and calculates areas of the control-volume faces as well as $\alpha_\xi, \beta_\xi, \alpha_\eta, \beta_\eta$.

setup2 This part belongs to the subroutine *setup* and is the heart of the program. *Setup2* calculates the coefficients for all equations and solves them. Most of the subroutines are called here. The most important one is the *flux*.

flux All fluxes are calculated in this subroutine. This is the basic subroutine for CFV.

extra Extra constructs additional source term CON for non-orthogonal coordinate system, i.e., b_{no} for the velocity and transport correction equations.

solve Block corrected TDMA solver.

reset initializes (set to 0) source terms.

awrite Temporary storage of coefficients.

aread Reading from temporary storage.

stream calculates the streamfunction.

print print screen monitoring information.

diflow specifies the numerical scheme used in the code. Power law, Central Difference, Upwind, Hybrid, EDS are all included and can be selected as desired.

adaptive MAGG is executed here.

lineinp does a spline interpolation on the boundary curve, which has only a few points, in order to fill the grid along the boundary curve. This subroutine is only called by *adaptive*.

findp finds the boundary nodes if Neumann boundary condition is used for grid generation. This subroutine is also called by *adaptive* only.

turbsu calculates the production term for turbulence and adds turbulent source term in the u,v equations.

prodtk calculates the source term for the kinetic energy equation.

dissip calculates the source term for the energy dissipation equation.

walluv calculates the wall function for u,v equations.

wallt calculates the wall function for temperature equation.

sodiss calculates the wall function for dissipation equation.

gradnt calculates the gradients from the field values.

7. LIST OF VARIABLES

ael(ni,nj)	coefficient α_η (s,e, n,w)
ae2(ni,nj)	coefficient β_η (s,e, n,w)
aim(ni,nj)	coefficient $a_{i-1,j}$
aip(ni,nj)	coefficient $a_{i+1,j}$
ajm(ni,nj)	coefficient $a_{i,j-1}$
ajp(ni,nj)	coefficient $a_{i,j+1}$
ak1(ni,nj)	coefficient α_ξ (s,e, n,w)
ak2(ni,nj)	coefficient β_ξ (s,e, n,w)
ap(ni,nj)	coefficient $a_{i,j}$
ap0(ni,nj)	temporary storage of $a_{i,j}$
aratio	aspect ratio of melt
b	crucible radius
b1jbl(nj)	heat flux at the solid side at the vicinity of the interface
b2jbl(nj)	heat flux at the melt side
b3jbl(ni)	heat flux
birad	coefficient Bi_r
bpeta(ni,nj)	bpeta is temporary saving of peta, pressure eq.
bpksi(ni,nj)	bpksi is temporary saving of p_ξ
cappa	constant in wall function
cd	constant in wall function
cfo	1/time scale, dimensional time scale, $cfo \times dt$ is time in second.
cl	heat capacity C_p of liquid
cmu	constant in k- ϵ model $\mu_t = c_\mu k^2/\epsilon$
con(ni,nj)	a generic part of the source term
con0(ni,nj)	represents the old con and is also used as temporary savings.
cs	heat capacity C_p of solid
delt	dimesionless time step
dtm	time step
epsil	a small number .0001, used to define convergence
ewall	constant in wall function
f(ni,nj,nk)	3D array which stores physical variables: u,v,w,p,pc,t
f(ni,nj,1)	u, axial momentum equation
f(ni,nj,2)	v, r-momentun equation
f(ni,nj,3)	p, pressure equation
f(ni,nj,4)	pc, pressure correction
f(ni,nj,5)	t, temperature
f(ni,nj,6)	wr, swirl

f(ni,nj,7)	tk, kinetic energy equation
f(ni,nj,8)	te, turbulent dissipation equation
f(ni,nj,9)	psi, electrical streamfunction, from magnetic field
fcsl	cs/cl: viscosity parameter
fjbil(nj,ns)	value $J = \rho u + \gamma \times \text{grad } u$ on $i=1$ boundary
fjbjl(ni,ns)	value $J = \rho u + \gamma \times \text{grad } u$ on $j=1$ boundary
fjbl1(nj,ns)	J on $i=11$, or right hand side
fjbm1(ni,ns)	J on $j=m1$
fjeta(ni,nj)	flux \mathbf{J}_η (implicit)
fjksi(ni,nj)	flux \mathbf{J}_ξ
fkl	conductivity of liquid
fks	conductivity of solid
fksl	fks/fkl: viscosity parameters
fluxm	wall heat fluxes, used for output
fluxm1	same
fluxm2	same
fma	Marangoni number (f for float)
fo(ni,nj,nk)	storage of variables for old grid system for unsteady calculation
fr	Froude number
frsl	ρ_s/ρ_l
gam(ni,nj)	transport coefficients, viscosity or diffusion
grash	Grashof number
grav	gravity
grre	Gr/Re^2
hamag	Hartmann number in magnetic field
heta(ni,nj)	curve length in eta direction
hf	latent heat of fusion
hksi(ni,nj)	curve length in ξ direction
idemon	=0:cavity;=1: CZ crystal growth for flat interface; =2: CZ crystal growth
init	= 0: initializing
init	= 1: restart
ipref	i coordinate for pressure reference point
iter	iteration counter
izone	zone number
jpref	j coordinate for pressure reference point
l0	same role as of l1
l1	grid size in i direction (vertical)
l2	= l1 -1
l3	= l2 -1 = l1 -2
lblk	flag for block-correction
lconv	specifies if the problem has converged

lortho	false: orthogonal; true curvilinear
lpgrid	specifies if grid needs to be printed
lprint	specifies if output is required for a problem
lsave	specifies if something has to be saved
lsolve	specifies if a problem needs to be solved
lst	specifies end of crystal in horizontal direction
lst2	specifies end of crystal in vertical direction
lstop	specifies if the program should terminate
ltpr	logical switch in print
m0	same role as of m1
m1	grid size in j direction (horizontal)
m2	= m1 - 1
m3	= m2 - 1 = m1 - 2
mode	= 0: Cartesian problem
mode	= 1: cylindrical problem
ndt	number of time steps
nf	nf: specifies problem to be solved
nfmax	nfmax: max number of problems
ni=84	number of gridblocks in i (vertical direction)
nj=84	number of gridblocks in j (horizontal direction)
nk=12	max number of problems to be solved (see f(i,j,k))
nmaxij=84	dimension pt and qt array
np	identifier for pressure (3)
npc	identifier for corrected pressure (4)
ns	number of variables
nrho	identifier for density (7)
ns=9	number of problems to be solved
nsolve(ns)	number of iteration for solving equations
ntimes(ns)	number of iteration for flux correction
p(ni,nj)	pressure
pc(ni,nj)	corrected pressure
peta(ni,nj)	p gradient in η directon
pksi(ni,nj)	p gradient in ξ directon
pr	Prandl number
pres0	reference pressure
r(ni,nj)	radial coordinate
ra	Rayleigh number = $Gr \times Pr$
rbd	Ma/Ra
rbo	reciprocal of Bond number
rdtm	another time step

re	Reynolds number
recb	crucible Reynolds number
rect	crystal Reynolds number
relax(ns)	relaxation coefficient
res(ns)	max error for equation ns
rho(ni,nj)	density
rhocon	density reference=1.0
rho1	density of liquid
rhos	density of solid
rpr	$=1/(re * pr)$
rre	inverse of Reynolds number
rueta(ni,nj)	ρu_η
ruksi(ni,nj)	ρu_ξ
sige	constant in turb model
sigk	constant in turb model
sigma	surface tension
sigt	constant in turb model
smax	maximum local mass imbalance
ssum	total mass imbalance
stel	liquid Stefan number
stes	solid Stefan number
t(ni,nj)	temperature
tanca	tangent of contact angle near the crystal
tanca2	tangent of contact angle near the wall
tend	time end
tf	fusion (melting) temperature of crystal
tinit	initial time
tpass	run time
tw	wall temperature
u(ni,nj)	u component velocity
u0	characteristic velocity
v(ni,nj)	v component velocity
vol(ni,nj)	volume of the control element
w(ni,nj)	angular velocity
weber	Weber number
x(ni,nj)	x coordinate of primary nodes
xc(ni,nj)	x coordinate of the corner of the control volume
xlen	length in x direction
y(ni,nj)	y coordinate of primary nodes
yc(ni,nj)	y coordinate of the corner of the control volume
ylen	length in y direction

8. CONCLUDING REMARKS

As a final note, the code is being continually updated and improved versions will be available in future. The manual will also be updated every 3-4 months. Please send your comments and suggestions. A two-dimensional parallel code as well as a three-dimensional code are under development.

Bibliography

- [1] H. Zhang, and V. Prasad, 1995, "A Multizone Adaptive Process Model for Crystal Growth at Low and High Pressures," *Journal of Crystal Growth* (in press).
- [2] H. Zhang, V. Prasad, and M. K. Moallemi, 1995, "Application of MAGG - A Multizone Adaptive Generation technique - for Simulations of Moving and Free Boundary Problems," *Numerical Heat Transfer* (submitted).
- [3] H. Zhang, and M. K. Moallemi, 1995, *Numerical Heat Transfer, Part B, Vol. 27*, pp. 255-276.
- [4] H. Zhang, Ph.D. Dissertation, Polytechnic University 1994.
- [5] H. Zhang, V. Prasad, and D. Bliss, 1995, "Transport Phenomena in a High Pressure Crystal Growth System: In-situ Synthesis for InP Melt," *Journal of Crystal Growth* (submitted).
- [6] H. Zhang, V. Prasad, and D. Bliss, 1995, "Transport Phenomena in High Pressure Crystal Growth Systems for III-V Compounds," *Journal of Crystal Growth* (submitted).
- [7] V. Prasad, D. F. Bliss and J. A. Adamski, *J. Crystal Growth* 142 (1994) 21.
- [8] S. V. Patankar, *Numerical Heat Transfer and Fluid Flow*, Hemisphere (1980).
- [9] B. E. Launder, *Turbulence, Topics in Applied Physics, 12* (Springer, Berlin, 1978).
- [10] Brackbill, J. U., and Saltzman, J. S., 1982, Adaptive Zoning for Singular Problems in Two Dimensions, *Journal of Computational Physics*, Vol. 46, pp. 342-368.
- [11] G. Muller, *Crystals*, 12, Springer-Verlag, Berlin (1988).
- [12] D.T.J. Hurle and B. Cockayne, *Handbook of Crystal Growth*, Vol. 2a, Ed. D.T.J. Hurle (North-Holland, New York, 1994).
- [13] R. A. Brown, *AIChE J.* 43 (1988) 881.
- [14] S. J. Motakef, *J. Appl. Mech.* 54 (1987) 813.
- [15] F. Dupret and N. Van den Bogaert, in: *Handbook of Crystal Growth*, Vol. 2b, ed. D.T.J. Hurle (North-Holland, New York, 1994).

- [16] T. A. Kinney, D. E. Bornside, R. A. Brown and M. K. Kim, J. Crystal Growth 126 (1993) 413.
- [17] Y. T. Chan, H.J. Gibeling and H. L. Grubin, J. App. Phys. 64, 1425 (1988).
- [18] J. J. Derby and R. A. Brown, J. Crystal Growth 74 (1986) 605.
- [19] H. Kopetsch, PhysicoChem. Hydrodyn. 11 (1989) 357.
- [20] A. Anselmo, V. Prasad, J. Koziol and K. P. Gupta, J. Crystal Growth 134 (1993) 116.
- [21] P. Sabhapathy and M. E. Salcudean, J. Crystal Growth 104 (1994) 371.

Appendix I

The physical phenomena and melt/crystal gas system for a high pressure crystal growth [1-20] under consideration is shown in Fig. 3 and a schematic for computational domain is presented in Fig. 4. The shape and motion of the melt/crystal and melt/encapsulant interfaces depend on heat flow in the melt and encapsulant and the temperature distribution in the crystal. There are two choices to solve this multiphase problem: one, to perform computations in various phases and satisfy interface/boundary conditions between adjacent zones, and second, to use a single domain approach and allow the parameters to vary with respect to the materials. The second approach has been adopted here because this method allows much more accurate and faster computations since no matching of conditions is required at the melt/crystal, melt/gas or crystal/gas interface.

With the assumptions that the system is two-dimensional, axisymmetric, and quasi-steady; the fluids are Newtonian; the flows are laminar; thermodynamic equilibrium is maintained locally, and the Boussinesq approximation is valid; Equation (1) yields the following set of equations for conservation of mass, momentum and heat:

$$\frac{\partial}{\partial t}(\gamma) + \frac{\partial}{\partial x}(\gamma u) + \frac{1}{r} \frac{\partial}{\partial r}(r\gamma v) = 0, \quad (0.80)$$

$$\begin{aligned} \frac{\partial}{\partial t}(\gamma u) + \frac{\partial}{\partial x}(\gamma uu) + \frac{1}{r} \frac{\partial}{\partial r}(r\gamma vu) &= \frac{\partial}{\partial x}(\zeta \frac{\partial u}{\partial x}) + \\ &\frac{1}{r} \frac{\partial}{\partial r}(r\zeta \frac{\partial u}{\partial r}) - \frac{\partial p}{\partial x} + \gamma Gr\theta, \end{aligned} \quad (0.81)$$

$$\begin{aligned} \frac{\partial}{\partial t}(\gamma v) + \frac{\partial}{\partial x}(\gamma uv) + \frac{1}{r} \frac{\partial}{\partial r}(r\gamma vv) &= \frac{\partial}{\partial x}(\zeta \frac{\partial v}{\partial x}) + \\ &\frac{1}{r} \frac{\partial}{\partial r}(r\zeta \frac{\partial v}{\partial r}) - \frac{\partial p}{\partial r} - \frac{v}{r^2} + \frac{w^2}{r}, \end{aligned} \quad (0.82)$$

$$\begin{aligned} \frac{\partial}{\partial t}(\gamma rw) + \frac{\partial}{\partial x}(\gamma urw) + \frac{1}{r} \frac{\partial}{\partial r}(r\gamma vrw) &= \frac{\partial}{\partial x}(\zeta \frac{\partial rw}{\partial x}) + \\ &\frac{1}{r} \frac{\partial}{\partial r}(r\zeta \frac{\partial rw}{\partial r}) - \frac{2}{r} \frac{\partial(rw)}{\partial r}, \end{aligned} \quad (0.83)$$

$$\begin{aligned} Rc \frac{\partial}{\partial t}(\gamma \theta) + Rc \frac{\partial}{\partial x}(\gamma u \theta) + Rc \frac{1}{r} \frac{\partial}{\partial r}(r\gamma v \theta) &= \frac{\partial}{\partial x}(\frac{\zeta Rc}{Pr} \frac{\partial \theta}{\partial x}) + \\ &\frac{1}{r} \frac{\partial}{\partial r}(r \frac{\zeta Rc}{Pr} \frac{\partial \theta}{\partial r}) - \nabla \cdot \mathbf{q}'' . \end{aligned} \quad (0.84)$$

Similarly, the equations for turbulent quantities and electric-magnetic field can be obtained from Table 1 and equation 11. In equation (84), the radiation heat flux is given by,

$$\mathbf{q}'' = \epsilon \sigma_r (T^4 - T_\infty^4) b / k Pr_o (T_h - T_f) = Bi_r (\theta - \theta_\infty). \quad (0.85)$$

The current radiation model does not account for the view factors and emissivities of various surfaces in the puller. The dimensionless parameters in the above equations, Gr_i , Pr_i , γ_i , ζ_i and Rc_i are defined in the nomenclature and i represents the phase/zone of the system. For example, in a HPCG system, Gr_i will have three values: Gr_l , Gr_e and Gr_g , for the melt, encapsulant and gas phases, respectively; whereas γ will have four values: γ_s , γ_l , γ_e and γ_g . These parameters will again vary from node to node in each subdomain if the thermophysical properties are allowed to vary depending on temperature and pressure. It should be noted that the definition of the Grashof number is based on ν_o ; $Gr_i = g\beta_i b^3(T_h - T_f)/\nu_o^2$.

Solidification of a pure substance is modeled with a fixed fusion temperature T_f , implying that the solid and liquid phases are separated by a sharp interface, $s(x, r, t) = H_1(r, t) - x = 0$, where H_1 is the dimensionless height of the melt/crystal interface. The energy balance at the interface defines its position and motion, and can be derived as,

$$\rho_s h_{sl}(U_{int,n} - U_s(t)\mathbf{e}_x \cdot \mathbf{n}) = k_s \frac{\partial T_s}{\partial n} - k_l \frac{\partial T_l}{\partial n}, \quad (0.86)$$

where the densities of the crystal and melt phases are assumed to be equal, \mathbf{n} is the unit normal vector from solid to melt, \mathbf{e}_x is unit vector in x-direction, $U_{int} = \partial H_1 / \partial t \mathbf{e}_x$ is the velocity of the crystal/melt interface movement in its normal direction, and $U_s(t)$ is the pull velocity. An expression for the movement of melt/crystal interface can be obtained as follows [19]:

$$\frac{\partial H_1}{\partial t} - U_s(t) = \frac{Ste_l}{Pr_l} (\kappa_s \frac{\partial \theta_s}{\partial n} - \kappa_l \frac{\partial \theta_l}{\partial n}) [1 + (\frac{\partial H_1}{\partial r})^2], \quad (0.87)$$

and the pull rate, $U_s(t)$, can be calculated from

$$U_s(t) = -(1 - Rr^2) \left\{ \frac{Ste_l}{Pr_l} (\kappa_s \frac{\partial \theta_s}{\partial n} - \kappa_l \frac{\partial \theta_l}{\partial n}) [1 + (\frac{\partial H_1}{\partial r})^2] \right\}_{r=Rr}, \quad (0.88)$$

where Rr is the radius ratio. This equation is based on the assumption that the crystal and melt are not separated at the tri-junction. Detailed equations for interface movement can be found in Kopetsch [19].

At the free surface, the required hydrodynamic conditions are: (1) fluid particles at the surface must remain attached (kinematic condition); (2) stress tangential to the surface is approximated as zero; and (3) stress normal to the surface must be exactly balanced by the externally applied normal stress [17]. Denoting the free surface position as $x = H_2(r, t)$, and enforcing orthogonality at the free surface, these conditions reduce to

$$u = \frac{\partial H_2}{\partial t} + v \frac{\partial H_2}{\partial r}, \quad (0.89)$$

$$\frac{\partial v}{\partial n} - \frac{\partial u}{\partial \tau} = \frac{Ma}{Pr} \frac{\partial \theta}{\partial n}, \quad (0.90)$$

where n and τ are the unit normal and tangential direction.

For a HPCG system, the shapes of the melt/encapsulant and encapsulant/ambient gas are determined by solving following equations simultaneously along with equations (1)-(5):

$$\begin{aligned} & \frac{\partial^2 H_2 / \partial r^2}{[1 + (\partial H_2 / \partial r)^2]^{3/2}} + \frac{\partial H_2 / \partial r}{r[1 + (\partial H_2 / \partial r)^2]^{1/2}} \\ & = Bo (H_2 - \Delta p \cdot Fr + 2\partial u / \partial n \cdot Fr), \end{aligned} \quad (0.91)$$

$$\frac{\partial H_{2,ls}}{\partial r} = \tan(\phi_{ls} - 90^\circ) , \quad \frac{\partial H_{2,lc}}{\partial r} = \tan(\phi_{lc} - 90^\circ) , \quad (0.92)$$

$$\int_{Rr_s}^1 (H_3 - H_2) r dr = \text{Constant} , \quad (0.93)$$

where H_2 and H_3 are the heights of the melt/encapsulant and encapsulant/ambient gas interfaces, respectively. The interface of the encapsulant/ambient gas is assumed to be flat since the viscosity B_2O_3 is very high. Ma is considered to be zero in the above equations while considering the high pressure growth. .

It should be noted that the accuracy of the solutions strongly depends on orthogonality at the interface and free surface. Much more complex expressions will be required to impose the interface and boundary conditions if the grids are non-orthogonal [17]. The melt meniscus connects to the edge of the growing crystal at the junction between melt, solid, and ambient gases or encapsulant. At the tri-phase point, the meniscus pins to the edge of the crystal and wets its own solid at a specified angle. Some of the important conditions are,
melt/crystal interface:

$$u = v = 0 , \quad w = Re_s r , \quad \theta = 0 ; \quad (0.94)$$

melt/encapsulant interface:

$$u = \frac{\partial H_2}{\partial t} + v \frac{\partial H_2}{\partial r} , \quad \frac{\partial v}{\partial x} = 0 , \quad \frac{\partial w}{\partial x} = 0 , \quad (0.95)$$

$$-\kappa_l \frac{\partial \theta_l}{\partial x} + \kappa_e \frac{\partial \theta_e}{\partial x} = Bi_{r,le} (\theta_{le} - \theta_\infty) ; \quad (0.96)$$

free surface of encapsulant:

$$\frac{\partial w}{\partial x} = 0 , \quad -\kappa_e \frac{\partial \theta_e}{\partial x} + \kappa_g \frac{\partial \theta_g}{\partial x} = Bi_{r,eg} (\theta_{eg} - \theta_\infty) ; \quad (0.97)$$

top and side wall of crystal:

$$u = U_s , \quad v = 0 , \quad w = Re_s r , \quad -\kappa_s \frac{\partial \theta_s}{\partial r} + \kappa_g \frac{\partial \theta_g}{\partial r} = Bi_{r,s} (\theta_s - \theta_\infty) ; \quad (0.98)$$

bottom and side wall of crucible:

$$u = v = 0 , \quad w = Re_c r , \quad \theta = 1 ; \quad (0.99)$$

Other interface and boundary conditions are quite standard as shown in Fig. 3 [20, 21]. It is evident that the problem is characterized by several dimensionless parameters, κ_i , Ste_j , Re_j , Ma_j , Fr_j , Bo_j , $Bi_{r,j}$, and geometric parameters, $Ar_j = h_j^*/b$ and $Rr_j = R_j^*/b$, where j represents the interface or boundary in the geometry in addition to Gr_i , Pr_i , γ_i , ζ_i , and Rc_i .

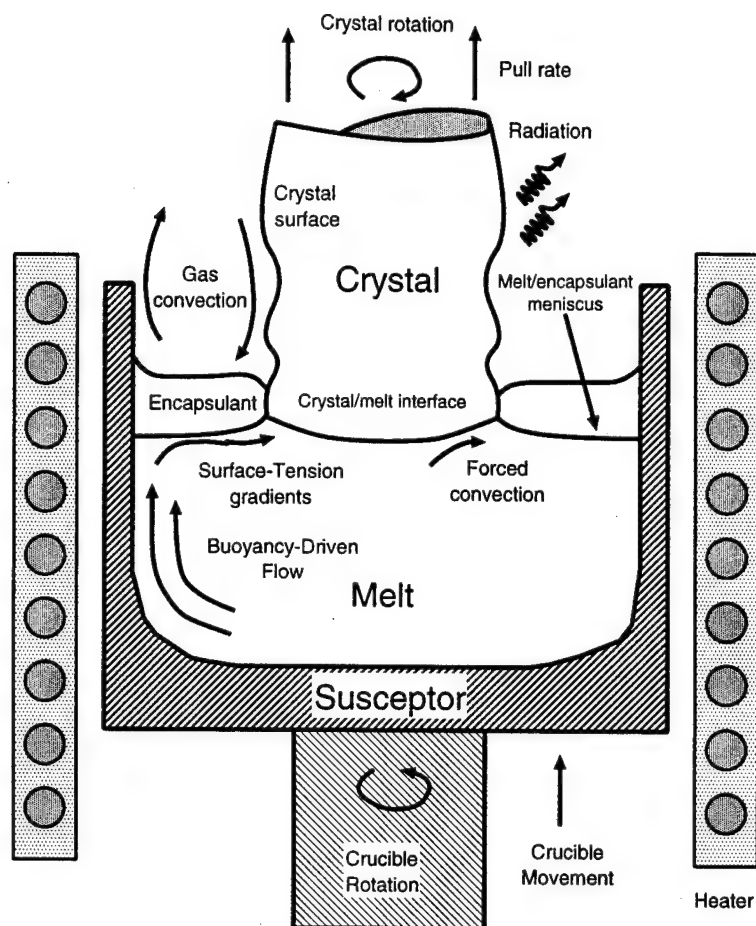


Figure 0.3: Schematic of a high pressure crystal growth system.

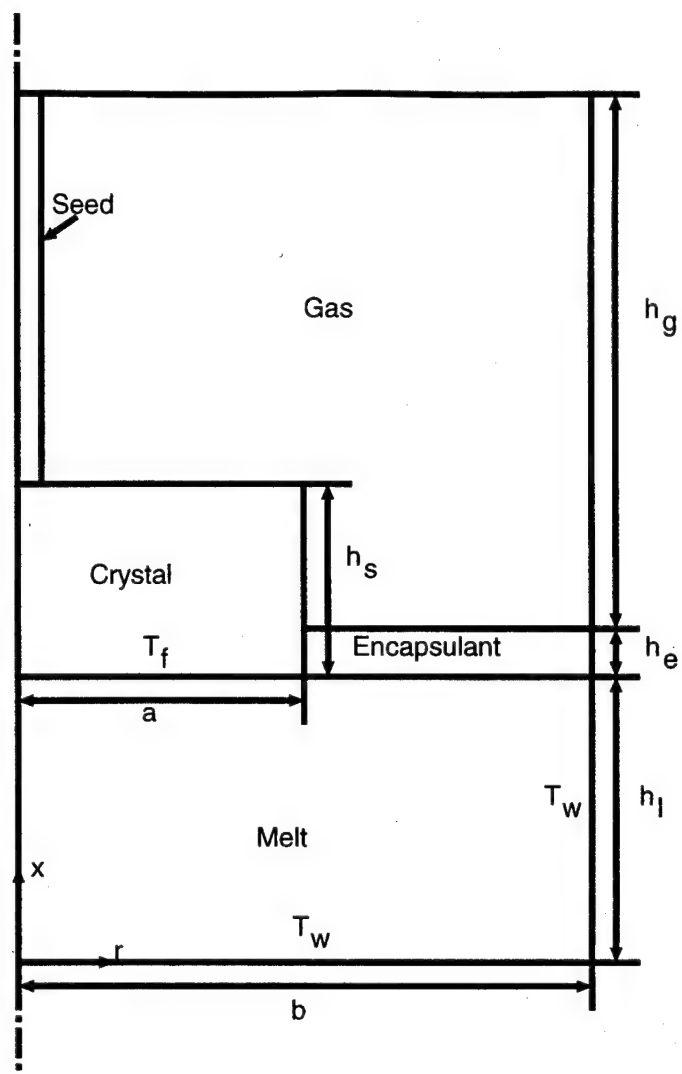
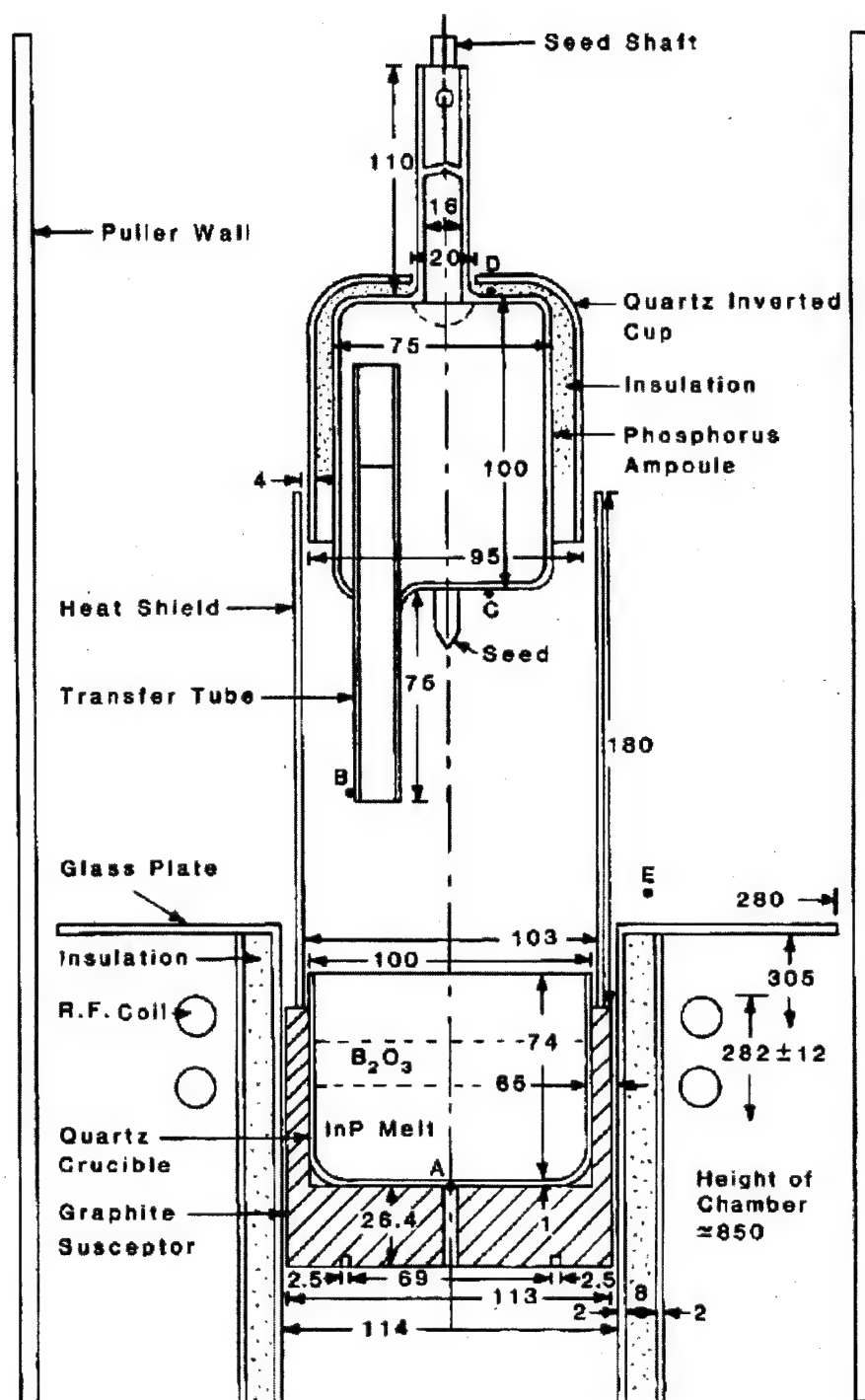


Figure 0.4: Schematic of a high pressure crystal growth system.



• Thermocouples A,B,C,D,E

Figure 0.5: Schematic of a high pressure system used for one-step synthesis and MLEK growth of indium phosphide crystals at Rome Laboratory.

Phase Dimensionless Parameters (i-phase)

Parameter	Definition
Grashof number	$Gr_i = g\beta_i b^3 (T_w - T_f) / \nu_i^2$
Prandtl number	$Pr_i = \nu_i / \alpha_i$
Density ratio	$\gamma_i = \rho_i / \rho_l$
Conductivity ratio	$\kappa_i = k_i / k_l$
Specific heats ratio	$Rc_i = C_{pi} / C_{pl}$
Viscosity ratio	$Rv_i = \mu_i / \mu_l$
Stefan number	$Ste_l = C_{pl} (T_l - T_f) / h_{sl}$
Froude number	$Fr_l = \nu_l^2 / gb^3$
Bond number	$Bo_l = \rho_l gb^2 / \sigma_l$
Hartmann number	$Ha_l = B_o b (\sigma_l / \mu_l)^{1/2}$

Geometric Dimensionless Parameter (j-surface)

Parameter	Definition
Reynolds number	$Re_j = \omega_j b / \nu_l$
Biot number	$Bi_{r,j} = \epsilon_{eff,j} \sigma_{rad} (T_j^2 + T_\infty^2) (T_j + T_\infty) b / k_l$
Aspect ratio	$Ar_j = h_j / b$
Radius ratio	$Rr_j = R_j / b$

Nomenclature for Appendix I

Ar	aspect ratio, melt height-to-crucible radius	h/b
Bi_r	radiation Biot number	$\epsilon_{eff}\sigma_r(T_{surf}^2 + T_\infty^2) \times (T_{surf} + T_\infty)b/k$
Bo	Bond number	$\rho gb^2/\sigma$
C_p	specific heat	J/kgK
Fr	Froude number	ν_o^2/gb^3
G	weight function of grid orthogonality, equation (25)	
Gr	Grashof number	$g\beta b^3(T_h - T_f)/\nu_o^2$
H_1	melt/crystal interface height	H_1^*/b
H_2	melt/encapsulant interface height	H_2^*/b
H_3	encapsulant/ambient gas interface height	H_3^*/b
Ja	Jacobian of transformation	$x_\xi y_\eta - x_\eta y_\xi$
M	grid inertial coefficient, equation (25)	
Ma	Marangoni number	$(d\sigma/dT)(T_h - T_f)b/\nu_o\alpha_o$
Pr	Prandtl number	ν_o/α_o
Rc	specific heat ratio	C_p/C_{po}
Re	Reynolds number	$\omega b^2/\nu_o$
Rr	radial ratio	R/b
S	source term	
Ste_l	liquid Stefan number	$C_{pl}(T_h - T_f)/h_{sl}$
Ste_s	solid Stefan number	$C_{ps}(T_\infty - T_f)/h_{sl}$
T	temperature, K	
W	weight function of grid concentration, equation (24)	
Γ	diffusion coefficient	
a	crystal radius, m	
b	crucible radius, m	
h	surface axial distance	h^*/b
h_{sl}	latent heat of fusion, J/kg	
g	acceleration due to gravity, m^2/s	
k	thermal conductivity, $W/(mK)$	
p	pressure	$P^*b^2/\rho_o\nu_o^2$
r	radial distance	r^*/b
t	time	$t^*\nu_o/b^2$
u	velocity in axial direction	u^*b/ν_o
v	velocity in radial direction	v^*b/ν_o
w	velocity in swirl direction	w^*b/ν_o
u_g, v_g	grid covariant velocity components	
x	axial distance	x^*/b

e_x	unit vector in x-direction	
n	unit normal vector	
α	thermal diffusivity, m^2/s	
β	thermal expansion coefficient, $1/K$	
$\alpha_\xi, \beta_\xi, \alpha_\eta, \beta_\eta$	geometric quantities	
γ	density ratio	ρ/ρ_o
ζ	viscosity ratio	μ/μ_o
λ	positive coefficient	
ξ, η	axes of curvilinear coordinates	
τ	unit tangential direction	
ρ	density, kg/m^3	
ϕ	general variable	
κ	thermal conductivity ratio	k/k_o
ϵ	emissivity	
ν	kinematic viscosity, m^2/s	
σ	Stefan-Boltzman constant, $W/(m^2 K^4)$	
θ	dimensionless temperature	$(T - T_f)/(T_h - T_f)$

Subscripts

P	node P
c	crucible
e	encapsulant
eff	effective
f	freezing temperature
g	gas
h	crucible temperature
i	index of phase
int	interface
j	surface
l	melt
m	inertia
o	reference
r	radiation
s	crystal
w	weight
ξ, η	curvilinear coordinates
∞	infinity

Superscripts

$*$	dimensional
-----	-------------

APPENDIX B

**TRANSPORT PHENOMENA IN A HIGH PRESSURE CRYSTAL
GROWTH SYSTEM: IN-SITU SYNTHESIS FOR InP MELT**

H. Zhang and V. Prasad

Department of Mechanical Engineering
State University of New York at Stony Brook
Stony Brook, NY 11794-2300

and

D.F. Bliss

US Air Force Rome Laboratory
Hanscom AFB, MA 01731

(submitted to *Journal of Crystal Growth*)

Abstract

The physical phenomena underlying the "one-step" in-situ synthesis and high pressure growth of indium phosphide crystals are complex. A high resolution computer model based on multizone adaptive grid generation and curvilinear finite volume discretization has been used to predict the flow and temperature fields during the synthesis of the InP melt. Simulations are performed for a range of parameters, including Grashof number, crucible rotation, location and temperature of the seed as well as the injector. These parameters affect the gas flow in a HPCG system in a complex manner, and have significant influence on thermal conditions in the furnace. Simulation for high pressure growth are presented in a companion paper [1].

Research sponsored by Air Force Office of Scientific Research
and GT Equipment Technologies, Inc.

1. INTRODUCTION

III-V semiconductor crystals are crucial to many important technological applications such as light-wave communications, fiber optics, lasers, sensors, solar cells and micro-electro-mechanical systems. Many new technologies, e.g., micro- and millimeter wave HEMT and HBT transistors and communication systems and MESFETS require these compound crystals (e.g., GaP, InP, GaN and AlN) that can be grown only at high and ultra-high pressures. To meet these demands, the crystal growth technology is moving in new directions leading to improvement in quality and size of the crystals and reduction in their costs. For example, GaAs crystals are being grown at much higher than the atmospheric pressure from an in-situ synthesized melt, high pressure systems are being designed for one-step synthesis and growth of binary and ternary compound crystals (e.g., InP, InGaAs) and bulk growth of ultra-high pressure compounds are being considered [2-4].

The in-situ compounding of InP and GaP by careful heating of the elements (solid phosphorus and indium) under the encapsulant layer (B_2O_3) as done in the case of GaAs is not readily possible because of the difference in melting point of InP and sublimation temperature of solid P. It is, however, possible to inject phosphorus vapor into either In or Ga melt. The equilibrium vapor pressure of phosphorus is very high (≈ 2.75 MPa) at the melting point of InP (1063°C). To produce InP crystals, high purity indium and phosphorus are synthesized in a high pressure chamber to produce InP polycrystalline raw material and then, melted in a high pressure crystal growth (HPCG) furnace to grow single crystals by the liquid-encapsulated Czochralski (LEC) method. These two-step methods are expensive and have generally hindered the broad use of InP substrates. This has motivated many researchers to propose and investigate one-step "in-situ" synthesis and growth technique, i.e., pulling a single crystal from an "in-situ" synthesized melt.

Antypass [5, 6] designed a process in which the P-vapor from an ampoule is injected into the B_2O_3 encapsulated In melt to produce InP melt which is then allowed to solidify after the synthesis is completed. After removing the P-ampoule, the chamber is resealed, evacuated

and pressurized, and a crystal is grown. Antypass succeeded in growing a twin-free InP crystal of 7.4 cm in diameter. Later, Dowling et al. [7] grew ingots of 20.3 cm in diameter by this process. Farges [8] improved this process by designing the seed rod pass through the P-ampoule thereby eliminating the need for its removal from the chamber. The P-injector is lifted after the synthesis and the seed rod is brought down for crystal growth. Farges succeeded in growing InP ingots using his new design. However, he could not grow single crystals due to the problems of twinning and surface decomposition. Bliss et al. [9, 10] have further improved the furnace and conducted successful "in-situ" syntheses, and have grown many single crystals of approximately 7.6 cm in diameter. In their process, the heat radiated by the melt can be absorbed by solid P for melting and/or sublimation. The temperature inside the P-injector can therefore be controlled by changing the vertical location of the injector [11]. The ampoule is placed directly above the melt and the vapor is transferred to indium melt by a quartz tube (Fig. 1).

The one-step synthesis and LEC (or MLEK) growth is very attractive for the following reasons: (a) elimination of expensive high pressure equipment for the synthesis of polycrystalline charge, (b) the charge is crucible shaped therefore optimizing the furnace capacity for single crystal growth, (c) no need to solidify and remelt the charge, (d) no possibility of contamination since the polycrystalline InP does not have to be taken out from the synthesis chamber and placed into a HPCG furnace, (e) possibility of increasing the size of the crucible and grow single crystals of larger diameters, and (f) significant savings in processing time and operation cost. Although this process has been successful in producing polycrystalline ingots of large sizes and is being used commercially for this purpose, only limited success has been achieved in growing crystals from the synthesized InP melt in a continued operation due to several problems. Many times, a stoichiometric InP melt is not obtained because (a) the required amount of P-vapor cannot be injected into the melt due to poor thermal conditions in the furnace, (b) the P-vapor leaving the injector tube reacts locally to produce InP but the melt cannot sustain a temperature higher than 1063°C resulting in local freezing, (c) the

fluctuation in temperature inside the injector may at some point decrease the volume of the inert gas or P-vapor/gas mixture resulting in suction of the melt inside the injection tube and freezing, or (d) a large amount of P-vapor may leave the melt without reaction due to local supersaturation. The phosphorus vapor released due either to the local supersaturation or after the reaction is completed can also obstruct the visibility for control of the crystal growth process.

The success of "in-situ" synthesis therefore strongly depends on thermal conditions in the HPCG furnace, the inert gas flow phenomena and the rate at which the injector is moved up and down. Indeed, the movement of P-injector changes the temperature field significantly by modifying the radiation exchange between various surfaces and by changing the convective gas flow rate and its structure [11]. The temperature at injector bottom may oscillate during the vaporization process. The energy generated into the melt due to exothermic reaction, and the volume increase ($\rho_{In} = 7310 \text{ kg/m}^3$ and $\rho_{InP} = 4787 \text{ kg/m}^3$) also affect the heat transfer and the gas velocity. To our knowledge, almost nothing has been reported on this topic. An estimate of the strength of radiation and gas convection as well as temperature measurements in a HPCG furnace has been reported recently by Prasad *et al.* [11]. Other notable works on this topic are by Muller *et al.* [12] and Volkl *et al.* [13].

Since the difficulties associated with in-situ synthesis and growth at high pressures are considered to be a roadblock to the technological advancements in the field of compound crystals, it is important to improve our understanding of the mechanisms of energy transport and flow phenomena in the HPCG system. The transport phenomena associated with the in-situ synthesis for InP melt is studied in this paper using a high resolution computer code, MASTRAPP2d [14-16]. The effect of Grashof number and crucible rotation on gas convection has been investigated for selected cases. The variation in flow pattern and temperature distribution with a change in the location of P-injector is also demonstrated. The transport phenomena associated with the growth process is presented in detail in a companion paper [1].

2. MATHEMATICAL MODEL

A schematic of the HPCG system under consideration is presented in Fig. 1. It is assumed that the system is axisymmetric; the thermodynamic equilibrium is maintained locally; the thermophysical properties of the crystal, the melt and the encapsulant are constant; and the properties of the inert gas change with temperature and pressure. In addition, the crystal and the melt are considered to be grey bodies and each of them exchange radiation only with the HPCG walls which are treated as isothermal blackbodies. The encapsulant is considered transparent to radiation. The encapsulant/gas interface is assumed to be flat, and the thermocapillary effects due to the surface tension gradients in the melt/encapsulant and encapsulant/inert gas are neglected. (The viscosity of the encapsulant B_2O_3 is very high.) In this model, the crucible side wall and bottom are assumed to be at a constant temperature, and the pull rate is adjusted to maintain a desired crystal diameter. The model considers turbulent flows in the gas, but only laminar flows in the melt that may oscillate. While simulating the convective flows during synthesis, the effects of exothermic reaction and volume change due to reduction in density ($\rho_{InP} < \rho_{In}$) are neglected. It should be noted that these properties strongly influence the synthesis part of the "one-step" process [11] and determine the melt quality. However, the objective of present calculations is to first understand the global transport mechanism in a HPCG system.

With these assumptions, the conservation equations for mass, momentum, and energy in the melt, the encapsulant (B_2O_3) and the inert gas, and energy equation in the solid can be written in a general form as

$$\frac{\partial}{\partial t}(\bar{\rho} r \phi) + \frac{\partial}{\partial z}(\bar{\rho} r u \phi) + \frac{\partial}{\partial r}(\bar{\rho} r v \phi) = \frac{\partial}{\partial z}(r \Gamma_{\phi} \frac{\partial \phi}{\partial z}) + \frac{\partial}{\partial r}(r \Gamma_{\phi} \frac{\partial \phi}{\partial r}) + r S_{\phi} . \quad (1)$$

where ϕ is the generalized variable (Table 1), S is the volumetric source, Γ is the diffusion coefficient. Equation (1) is used for the entire multiphase, multicomponent domain with the provision to account for local properties and abrupt changes in transport properties across

Table 1: Variables for generalized governing equation (1).

Equations	Variable ϕ	Diffusivity Γ_ϕ	Source S_ϕ
Continuity	1	0	0
z - momentum ⁺	u_i	$\bar{\mu}_{i,eff}$	$-\partial p/\partial z + \bar{\rho}Gr\theta + S_{turb}$
r - momentum ⁺	v_i	$\bar{\mu}_{i,eff}$	$-\partial p/\partial r - v/r^2 + w^2/r + S_{turb}$
rw - angular momentum ⁺	rw_i	$\bar{\mu}_{i,eff}$	$-(2/r) \partial(rw)/\partial r + S_{turb}$
Energy ⁺	$\bar{C}_{pi}\theta_i$	$\bar{k}_{i,eff}/Pr_o$	$-\nabla \cdot \mathbf{q}'' + S_{turb}$
k - kinetic energy	k	$\bar{\mu}_{eff}/\sigma_k$	$\bar{G} - \bar{\rho}\epsilon$
ϵ - dissipation	ϵ	$\bar{\mu}_{eff}/\sigma_\epsilon$	$C_1\bar{G}\epsilon/k - C_2\bar{\rho}\epsilon^2/k$

⁺ The terms, S_{turb} refers to the source terms from turbulence.

the zone boundaries, and their possible movements. The conventional $k - \epsilon$ turbulence model is used in the gas phase [18].

The following scales have been used to non-dimensionalize the governing equations; length: b , velocity: ν_o/b , pressure: $\rho_o\nu_o^2/b^2$, time: b^2/ν_o , density: ρ_o , dynamics viscosity: μ_o , conductivity: k_o , specific heat: C_{po} , and temperature: $\theta = (T - T_\infty)/(T_h - T_\infty)$. where subscript 'o' refers to the gas properties at environment temperature T_∞ . In above equations, $\bar{\mu}_{i,eff}$ and $\bar{k}_{i,eff}$ are the effective dimensionless viscosity and conductivity, respectively, and have both laminar and turbulent components,

$$\bar{\mu}_{i,eff} = \bar{\mu}_i + C_\mu \bar{\rho} k^2 / \epsilon, \quad \bar{k}_{i,eff} = \bar{k}_i + C_\mu \bar{\rho} k^2 / \epsilon \cdot Pr_o / Pr_{turb}. \quad (2)$$

where Pr_{turb} is the turbulent Prandtl number. The radiation heat flux in energy equation is given by:

$$q'' = \epsilon \sigma_r (T^4 - T_\infty^4) b / k_o Pr_o (T_h - T_\infty) = Bi_r (\theta - \theta_\infty). \quad (3)$$

In the above equations, the governing parameters are Gr_i , Pr_i , $\bar{\rho}_i$, $\bar{\mu}_i$, \bar{C}_{pi} , where i represents the phase/zone of the system. It should be noted that the temperature is nondimensionalized

using temperature difference between the crucible and the cold walls of the furnace. The dimensionless temperature and Gr_g are based on $(T_h - T_\infty)$ and Gr_m is based on $(T_h - T_f)$ which is commonly used in the modeling of the CZ growth. Some of the boundary conditions used for the simulation of the synthesis can be written as follows:

bottom of the crucible:

$$u = v = 0, \quad w = Re_c r, \quad \theta = 1; \quad (4)$$

free surface of the encapsulant:

$$\frac{\partial w}{\partial z} = 0, \quad -\bar{k}_e \frac{\partial \theta_e}{\partial z} + \bar{k}_g \frac{\partial \theta_g}{\partial z} = Bi_{r,eg} (\theta_{eg} - \theta_\infty); \quad (5)$$

bottom surface of the injector:

$$u = w = 0, \quad v = V_{inj}, \quad -\bar{k}_{inj} \frac{\partial \theta_{inj}}{\partial z} + \bar{k}_g \frac{\partial \theta_g}{\partial z} = F_{inj} Bi_{r,inj} (\theta_{injg} - \theta_\infty); \quad (6)$$

top surface and side wall of the puller:

$$u = v = w = 0, \quad \theta = \theta_\infty; \quad (7)$$

central axis:

$$\frac{\partial u}{\partial z} = v = \frac{\partial w}{\partial z} = 0, \quad \frac{\partial \theta}{\partial z} = 0. \quad (8)$$

where F_{inj} is the view factor between the bottom of the injector and the encapsulant/melt interface, and is obtained from an expression for the two parallel cylindrical disks [17]. As the injector moves downward, the view factor increases, thereby enhancing the radiation heat gained by the injector. A formulation for wall function correction has been used for all walls in the gas phase to incorporate the turbulence model [18]. The quartz heat shield is considered fully transparent to radiation. These conditions indicate that the problem is characterized by several other governing parameters, \bar{k}_j , Re_j , $Bi_{r,j}$, Fr_j , Bo_j and geometric parameters, Ar_j and Rr_j , where j represents the interface/boundary. Both the dimensional and nondimensional variables are defined in nomenclature and their values for present calculations are given in Table 2.

The synthesis process is therefore governed by a large number of parameters such as Grashof and Prandtl numbers; crucible Reynolds number; Biot number for radiation heat transfer; density, thermal conductivity and specific heat ratios for solid and gas phases; parameters to govern thermophysical property variation in the gas; geometric variables, and so on. These parameters vary greatly with a change in the phase/zone, as well as with the surface characteristics and injector location.

For present simulations, we have used a high resolution two-dimensional computer code, MASTRAPP2d, developed for transport and phase-change processes associated with time-varying domains and irregular boundaries. The numerical scheme employs (a) a multizone adaptive grid generation technique (MAGG) for the discretization of physical domains of arbitrary shape, and (b) the curvilinear finite-volume (CFV) approach for the discretization of the governing partial differential equations and development of the finite difference equations. The MAGG scheme is based on constrained adaptive optimization of grid characteristics. One of the major advantages of this scheme is that it preserves internal interfaces separating various zones and always makes them coincide with some grid lines. The scheme allows grids to move adaptively as the solutions progress and/or domains change. The generated grids are always smooth and orthogonal, maintain slope continuity, and cluster in the regions of interfaces/free surfaces and large gradients. The CFV approach is based on flux discretization in the physical domain which makes the change of domain boundaries in the process model easy and less costly. A detailed description of the numerical scheme and its suitability for crystal growth processes at both low and high pressures can be found in Zhang et al. [14-16].

3. RESULTS AND DISCUSSION

Figure 1 presents the schematic of the furnace being used by the US Air Force Rome Laboratory to develop the "one-step" process [9, 11]. In this system, the furnace walls and the seed shaft are cooled by circulating water from a constant temperature bath. A small gap exists between the shaft and the injector through which the seed rod passes, and hence,

the injector can be moved up or down independent of the seed shaft. A quartz shield is used to separate the strong convective flows in regions close to the cold wall from the buoyant flow directly above the melt. Another small gap exists between the outer surface of the injector and the heat shield. This geometric configuration produces a complex gas flow pattern in the system which strongly affects the phosphorus vaporization, injection and synthesis.

The computational domain including the melt and gas phases used for present simulations is shown in Fig. 2. The thermophysical properties of the gas (N_2) are allowed to vary with temperature at a constant high pressure (600 psi) while the properties of the melt and the crystal are considered to be constant. Although precise information on most of the thermophysical properties for InP is lacking, estimates have been obtained from Jordan [19]. For the calculations presented in Fig. 3, the governing equations in the melt region (consisting of the melt, encapsulant and crystal) and in the gas region (consisting of the injector, heat shield, seed shaft and crystal) are solved separately, followed by matching at the encapsulant /inert gas and crystal/inert gas interfaces. The procedure used here requires iterations between the two solutions. This approach may not be computationally efficient due to a weak link between the field variables in two domains. However, it reduces the number of nodes and CPU requirements, and focus this research on transport phenomena. The results reported here provide a basic understanding of the heat transfer and flow mechanisms in the HPCG furnace.

Figure 3 presents the temperature and stream function distributions in the gas, melt and crystal phases when the flow is induced by buoyancy at $Gr_g = 10^8$, $Gr_m = 10^7$ and rotation rates of $Re_c = -Re_s = 10^4$. The gas convection heat transfer at the encapsulant/gas and crystal/gas interfaces have been considered through the solution iterations. Heat is also lost by radiation from the crystal/gas interface. However, no radiation loss takes place at the encapsulant surface. The primary objective of the results presented in Fig. 3 is to demonstrate the effectiveness of MASTRAPP in performing simulations for a highly complex system with various phases and different materials as well as to show the general

flow pattern. Figure 3(b) exhibits the capability of the present algorithm to allow interface distortion due to energy release and phase-change. It also allows for the meniscus formation and its deformation at the crystal and crucible walls. A multicellular flow is produced in the melt and the melt/crystal interface is concave with respect to the crystal. Due to $Gr_m/Re_c^2 = 0.1$, the rotational forces are dominant in the melt which is clearly evident from the velocity field. A counter-rotating vortex develops beneath the crystal, in which the fluid flows upwards along the axis of symmetry and downward near the edge of the crystal. In fact, the rotation of the crystal induces the flow in a direction opposite to the flow produced by the buoyancy effect on the crucible wall. The upward flow along the axis of symmetry pushes the isotherms towards the crystal, thereby increasing the concavity of the interface (Fig. 3b). The concavity of the interface extends very close to the crystal periphery, yielding a monotonic concave shape. Figure 3(b) clearly demonstrates almost zero flow conditions in the encapsulant layer due to extremely high viscosity of B_2O_3 , as well as a large temperature drop due to much smaller thermal conductivity of B_2O_3 in comparison with the InP melt. Radial and axial temperature gradients are also evident in the crystal which is considered to be the primary cause for stresses in the crystal.

Figure 3(a) shows the corresponding temperature distribution and velocity field in the inert gas. Due to a low temperature at the seed shaft (cooled by circulating cold water) and a small gap between the shaft and the injector through which it passes, the gas flows downward along the seed. If the flow field reaches steady state, the same amount of gas must leave the inner region, through the opening between the shield and the P-injector to maintain continuity. A multicellular flow is produced in the region underneath the injector. These cells are slender and demonstrate strong flows with turning in the bottom and top regions while in the core the flow is somewhat parallel. Note that this flow is strongly influenced by counter-rotations of the crystal and the heat shield. (The heat shield sits on the graphite susceptor.) Correspondingly, an upward flow of hot gases is also established outside the heat shield which is further strengthened by the buoyancy effects induced by the

Table 2: Governing Parameters used in the simulation

Parameter	Definition	Value
Density ratio	$\bar{\rho}_s = \rho_s / \rho_m$	1.0
Conductivity ratio	$\bar{k}_s = k_s / k_m$	0.40
Specific heat ratio	$\bar{C}_{ps} = C_{ps} / C_{pl}$	1.0
Melt aspect ratio	$Ar_m = h_m / b$	0.68
Crystal radius ratio	$Rr = a / b$	0.5
Melt Grashof No.	$Gr_m = \frac{g\beta_m b^3 (T_h - T_f)}{\nu_m^2}$	10^7
Gas Grashof No.	$Gr_g = \frac{g\beta_g b^3 (T_h - T_\infty)}{\nu_g^2}$	10^8
Reynolds number		
for Crucible	$Re_c = \omega_c b^2 / \nu_m$	10^4
for Crystal	$Re_s = \omega_s b^2 / \nu_m$	-10^4
Melt Prandtl number	$Pr_m = \nu_m / \alpha_m$	0.015
Biot number	$Bi_r = \epsilon \sigma_r b / k_m Pr_m \times (T^2 + T_\infty^2)(T + T_\infty)$	—
Froude number	$Fr_m = \nu_m^2 / gb^3$	10^{-9}
Bond number	$Bo_m = \rho_m gb^2 / \sigma_m$	1000
Contact angles	ϕ_{sl}	45°

cold furnace walls. This produces a large recirculation in the furnace outside the heat shield and P-injector. A small convective roll is formed in the stagnation region directly above the injector as shown in Fig. 3(a).

From Fig. 3, it is evident that an intense gaseous convection is induced in the furnace and takes heat away from the surfaces of the crystal and encapsulant. The temperature distribution in the crystal and the shape of the crystal/melt interface are therefore strongly influenced by the gas flow. The existence of the liquid encapsulant and the high pressure gas make the transport mechanism much more complex than that observed in the case of CZ melt flow for Si. An extensive study of the gas flow is therefore necessary to develop an understanding of the high pressure crystal growth and control of the crystal quality, and is presented in a companion paper [1]. Based on a series of experiments, a quartz shield was found to be an effective way to suppress the gaseous convection. Computations to examine the effect of heat shield on gas flow are also presented in this paper. As noted earlier, the synthesis for InP melt is affected by many different operating parameters, The effects

of Grashof number, crucible rotation, and position and temperature of the seed as well as injector are studied next.

Figure 4(a) presents the flow field and temperature distribution for $Gr_g = 10^8$ and $Re_c = 0$. The surface of the injector bottom is assumed grey and is allowed to exchange radiation only with the melt surface. Because we are more concerned with the heating/cooling effect and dynamic characteristics of the injector, crystal and encapsulant surfaces, and this is the region where the distribution of field variables are more complex (Fig. 3), only lower part of the gaseous region is shown in most of the figures. It should, however, be noted that computations for all cases presented here are performed for the entire gas domain. In contrast with the previous case (Fig. 3), the solid crystal is removed from the computational domain for flow simulations during the synthesis. The primary flows, downward along the seed and upward along the heat shield, is similar to that observed in Fig. 3(a). The flow structure underneath the injector is, however, very complex. A higher temperature at the encapsulant surface and low temperature in the upper region produces a Benard-type convective roll in this region. This cell is strengthened by the downward flow along the seed, and after turning, a part of the gas moves up towards the opening. This induces two slender convective rolls on top of the primary recirculating cell. Interestingly, these two cells exhibit somewhat centrosymmetric behavior due to the symmetric nature of the inward and outward flows. Even though the gas flows out through the gap between the heat shield and the injector, the flow along the inner surface of the shield is mostly downward. This complex flow field produces a complicated temperature distribution directly above the encapsulant surface. Radial and vertical inversions in temperature gradients are evident in Fig. 4(a). There exist strong temperature gradients in the vicinity of the seed rod and the heat shield. The temperature distribution outside the heat shield is straight-forward, and the temperature is quite low, which qualitatively agrees with the experimental observation [11].

Effects of the crucible rotation on gas flows are shown in Figs. 4(b) and 4(c) for $Re_c = 10^3$ and 10^4 , respectively. Both the encapsulant surface and heat shield rotate when the crucible

is rotated, while other parts of the system remain stationary. Figs. 4(a)-(c) show that the three-cell flow structure changes drastically due to the centrifugal action, as Re_c is increased beyond zero. In Fig. 4(b), a small secondary cell has been created on the heat shield because of the separation of the downward flow from the wall. This cell grows in vertical direction and finally occupies a large region in the vicinity of the heat shield when $Re_c = 10^4$. The Benard-type bottom cell becomes weak as the rotation rate increases and gives rise to four slender cells in Fig. 4(c). The two small cells are located in the vicinity of the seed in lower portion while other two large cells occupy the entire space.

The temperature distribution is also modified significantly by the rotation rate and changing flow field. The transport of heat to the upper region increases significantly with the rotational speed. There exist sharp radial and axial temperature gradients and strong temperature inversions above the encapsulant surface. The bottom temperature of the injector is also changed as the rotation rate increases. Figure 5(a) presents the non-dimensional temperature with respect to the radius at the injector bottom for $Re_c = 0, 10^3$ and 10^4 . The temperature distribution for $Re_c = 10^3$ is quite close to that for $Re_c = 0$. The temperature increases with the radius, and it is lowest near the cold seed rod. The temperature increases as the rotation rate increases. Since the radiation heat transfer is almost constant (loss to isothermal surfaces of the furnace) in this simulation, higher temperatures on the surface mean large heat transfer from the crucible walls due to convective effects. The temperature goes drops the heat shield. The right end of the curve in Fig. 5 represents temperature at the internal surface of the heat shield. This non-uniform temperature profile is expected to dramatically affect the vaporization process inside the phosphorus injector.

To present the buoyancy effects on gas flows, velocity and temperature fields for $Gr_g = 10^7, 10^9$ and 10^{11} with $Re_c = 10^3$ are plotted in Figs. 6(a) to 6(c), respectively. The bottom temperature of the injector is shown in Fig 5(b). These results reveal that the three-cell structure again changes to a multi-cell structure, as Gr is increased. The buoyancy force produces much stronger temperature gradients close to the encapsulant surface and a recir-

culatory flow in this region. However, the rotational effects attempt to destroy this behavior and complicate the temperature field.

Effects of injector movement on temperature and flow fields are presented in Fig. 7 for Grashof number, $Gr_g = 10^{10}$, and Reynolds number, $Re_c = 10^3$. The temperature profiles at the injector bottom are shown in Fig. 5(c) for different positions. The temperature at the injector bottom increases as it moves down due to an increase in radiation heat transfer. Temperature at the upper end of heat shield remains almost the same. As the injector moves downward (Figs. 7a, 7b and 7c), the recirculating cells in the region between the injector and encapsulant lose their slenderness and become smaller. The strength of the convective flows depend on the location and temperature of the injector. A strong temperature field covers the entire domain particularly when the injector is at its lowest position. This is desirable for synthesis and supports the experimental observation that the heat transfer to solid P in the injector increases as the injector moves towards the melt surface [11]. These figures further indicate that the flow on top of the injector is also complex and can create a vortex when it is at a lower location.

To present the effects of the seed on gas flows, velocity field and isotherms for $Gr_g = 10^8$ and $Re_c = 10^4$ are plotted in Figs. 8(a) and 8(b) for two different sizes of the seed length. A comparison between Figs. 4(c) and Fig. 8 show that the flow structure changes significantly as the seed moves upward. From these figures it is evident that the seed position can have important effects on flow and temperature fields in the region below the injector, and implies that the movement of the injector tube will also dramatically change the flow field.

The quartz heat shield plays an important role in separating the flows underneath the injector and outside of the shield as observed in the experiment. To investigate this effect, simulations without the heat shield are presented in Fig. 9 for $Gr_g = 10^{10}$ and $Re_c = 10^3$. The gas flows in Fig. 9 are much stronger and complex in comparison with the results in Fig. 5(b). One large convection cell sits above the surface of the encapsulant layer and the size of the cell is exactly fitted into the cavity place. Gas flows upward along the seed shaft

although the seed shaft is still cold. This is primarily because the downward gas flow along the cold side wall is very strong and in the absence of a barrier, turns inward and moves upward in the vicinity of the seed shaft. Several secondary cells are produced inside this large cell making the flow structure further complex and unpredictable.

4. CONCLUDING REMARKS

Various stages of the "one-step" in-situ synthesis and high pressure LEK growth of indium phosphide crystals have been simulated for the first time. The numerical results demonstrate the complexity of the flow structure and temperature field in a HPCG system. The flow structure reported here agrees qualitatively with the visually observed flow behavior. However, calculations presented here are only preliminary and are not ready to be compared with the experimental data at this time due to lack of information on boundary conditions and process variables, as well as since the phosphorus vaporization and exothermic reaction have been neglected by the model. The results clearly indicate that the thermal conditions in a HPCG system are extremely complex. The quartz shield is very useful in isolating the strong convective flows in regions close to the cold wall from the buoyant flow directly above the melt, and to reduce the intensity of the gas flow along the seed shaft. The buoyancy dominated flow pattern in the system changes significantly with the rotation of the crucible and heat shield. It stabilizes the gas flow and increases the heat transfer between the injector bottom and gas flows. The positions of the seed and injector also affect the thermal field in the furnace dramatically. As the injector moves downward, the temperature of the injector bottom increases which is helpful for the synthesis. Since the injector temperature is controlled by an energy balance between radiation and convection heat transfer and vaporization of phosphorus, the model needs further improvement. Simulation of this kind can provide a better understanding of the HPCG process and can help the process designer to develop a process or redesign the system to achieve improved synthesis and growth conditions.

The "one-step" synthesis and high pressure growth is one of the most challenging materials processes, particularly from the modeling standpoint, and a numerical methodology

suitable for this process will have a potential for the development of a robust and versatile tool for modeling and simulation of many other complex materials processes. Present simulations demonstrate the effectiveness of the MASTRAPP algorithm to simulate multiphase systems with more than one material, and free and moving interfaces, and show the complexity of the flow structure and temperature field for the synthesis in a HPCG system that will ultimately determine the success of the "one-step" process and crystal quality.

ACKNOWLEDGMENTS

This research has been supported by the AFOSR program in computational mathematics, and GT Equipment Technologies (through a small business technology transfer grant from AFOSR). Acknowledgments are also due to A. Anselmo for helpful discussions.

Nomenclature

Ar	aspect ratio, h^*/b
Bi_r	radiation Biot number, $\epsilon\sigma_r(T^2 + T_\infty^2) \times (T + T_\infty)b/k_o Pr_o$
C_p	specific heat ($J kg^{-1}K^{-1}$)
F	view factor
G	turbulence product ($J m^{-3}s^{-1}$)
Gr	Grashof number, $g\beta b^3(T_h - T_\infty)/\nu^2$
P	pressure, $P^*b^2/\rho_o\nu_o^2$
Pr	Prandtl number, ν/α
Re	Reynolds number, $\omega b^2/\nu_o$
Rr	radius ratio, a/b
S	source term in equation (1)
T	temperature (K)
V	velocity of injector movement
a	crystal radius (m)
b	crucible radius (m)
g	acceleration due to gravity (m^2/s)
k	thermal conductivity ($W m^{-1}K^{-1}$) also, turbulence kinetic energy, k^*b^2/ν_o^2
r	radial distance, r^*/b
t	time, $t^*\nu_o/b^2$
u	velocity in axial direction, u^*b/ν_o
v	velocity in radial direction, v^*b/ν_o
w	velocity in swirl direction, w^*b/ν_o
z	axial distance, z^*/b
Γ	diffusion coefficient
α	thermal diffusivity (m^2s^{-1})
β	isobaric coefficient for thermal expansion (K^{-1})
ρ	density (kg/m^3)
μ	dynamic viscosity ($kg m^{-1}s^{-1}$)
ν	kinematic viscosity (m^2s^{-1})
σ	Stefan-Boltzman constant ($W m^{-2}K^{-4}$) also, turbulence parameters
ϵ	emissivity turbulence dissipation rate, ϵ^*b^4/ν_o^3
ϕ	generalized variable, equation (1)
θ	dimensionless temperature, $(T - T_\infty)/(T_h - T_\infty)$

Subscripts

c	crucible
e	encapsulant
eff	effective

f	freezing temperature
g	gas
k	kinetic energy
h	hot wall
inj	injector
m	melt
o	reference temperature
r	radiation
s	crystal
t	temperature
$turb$	turbulence
ϕ	generalized variable
ϵ	dissipation rate
∞	infinity

Superscripts

*	dimensional
—	nondimensional properties

References

- [1] H. Zhang and V. Prasad, "Transport Phenomena in a High Pressure Crystal Growth System: Growth of III-V Compound Crystals," *J. Crystal Growth* (submitted).
- [2] D.T.J. Hurle and B. Cockayne, in: *Bulk Crystal Growth*, Ed. D.T.J. Hurle (North-Holland, New York, 1994).
- [3] F. Dupret and N.V.D. Bogaert, in: *Bulk Crystal Growth*, Ed. D.T.J. Hurle (North-Holland, New York, 1994).
- [4] V. Prasad and H. Zhang, Challenging Issues in Bulk Crystal Growth Modeling, Proceedings, American Ceramic Society Annual Meeting, Cincinnati (1995).
- [5] G. A. Antypass, 2nd NATO Workshop on Material Aspects of InP, 1 (1983) 8.1.
- [6] S. B. Hyder and G. A. Antypass, 3rd NATO Workshop on Material Aspects of InP, 1 (1986).
- [7] D. J. Dowling, R. A. Brunton, D. A. E. Crouch, A. J. Thompson and J. E. Wardill, *J. Crystal Growth* 87 (1988) 37.
- [8] J. P. Farges, *J. Crystal Growth*, 59 (1982) 665.
- [9] D. F. Bliss, R. M. Hilton, S. Bachowski and J. A. Adamski, *J. Electronic Materials* 20 (1991) 967.
- [10] D. F. Bliss, R. M. Hilton and J. A. Adamski, 4th Int. Conf. on Indium Phosphide and Related Materials, 262 (1992).
- [11] V. Prasad, D. F. Bliss and J. A. Adamski, *J. Crystal Growth*, 142 (1994) 21.
- [12] G. Muller, J. Volkl and E. Tomzig, *J. Crystal Growth*, 64 (1983) 40.
- [13] J. Volkl and G. Muller, European Materials Research Society Symposia Proceedings, 16 (1987) 141.
- [14] H. Zhang and V. Prasad, "A Multizone Adaptive Process Model for Czochralski Crystal Growth at Low and High Pressures," *J. Crystal Growth* (in press).
- [15] H. Zhang and V. Prasad, ASME/JSME Thermal Engineering Joint Conference, Maui, Hawaii (1995).
- [16] M. K. Moallemi and H. Zhang, "A Multizone Adaptive Grid Generation Technique for Simulation of Moving and Free Boundary Problems," *Numerical Heat Transfer* (in press).
- [17] M. F. Modest, *Radiative Heat Transfer* (McGraw-Hill, Inc., New York, 1993).
- [18] B. E. Launder, *Turbulence, Topics in Applied Physics*, 12 (Springer, Berlin, 1978).
- [19] A. S. Jordan, *J. Crystal Growth* 71 (1985) 551.
- [20] H. Kopetsch, *J. Crystal Growth* 102 (1990) 505.

- Figure 1 Schematic of a high pressure system used for one-step synthesis and MLEK growth of indium phosphide crystals at Rome Laboratory.
- Figure 2 Grid distribution for the entire system consisting of crystal, melt, encapsulant and gas phases.
- Figure 3 (a) Temperature distribution and velocity field in the gas region when $Gr_g = 10^8$ for $Re_c = 10^4$, (b) Temperature and stream function distributions in the melt for $Gr_m = 10^7$.
- Figure 4 Temperature distribution and velocity field for $Gr_g = 10^8$ and (a) $Re_c = 0$ (b) $Re_c = 10^3$ and (c) $Re_c = 10^4$.
- Figure 5 Temperature distribution at the bottom of the injector for (a) different Reynolds number ($Re_c = 0, 10^3, 10^4$), (b) different Grashof number ($Gr_g = 10^7, 10^9, 10^{11}$), and (c) different injector position (above the free surface, 150 mm, 100 mm, 50 mm).
- Figure 6 Temperature distribution and velocity field for $Re_c = 10^3$ and (a) $Gr_g = 10^7$ (b) $Gr_g = 10^9$ and (c) $Gr_g = 10^{11}$.
- Figure 7 Effects of location of moving injector on the gas flow field for $Gr_g = 10^{10}$ and $Re_c = 10^3$.
- Figure 8 Effects of location of seed shaft on the flow field for $Gr_g = 10^8$ and $Re_c = 10^4$.
- Figure 9 Gas flow and temperature with a heat shield, $Gr_g = 10^{10}$ and $Re_c = 10^3$.

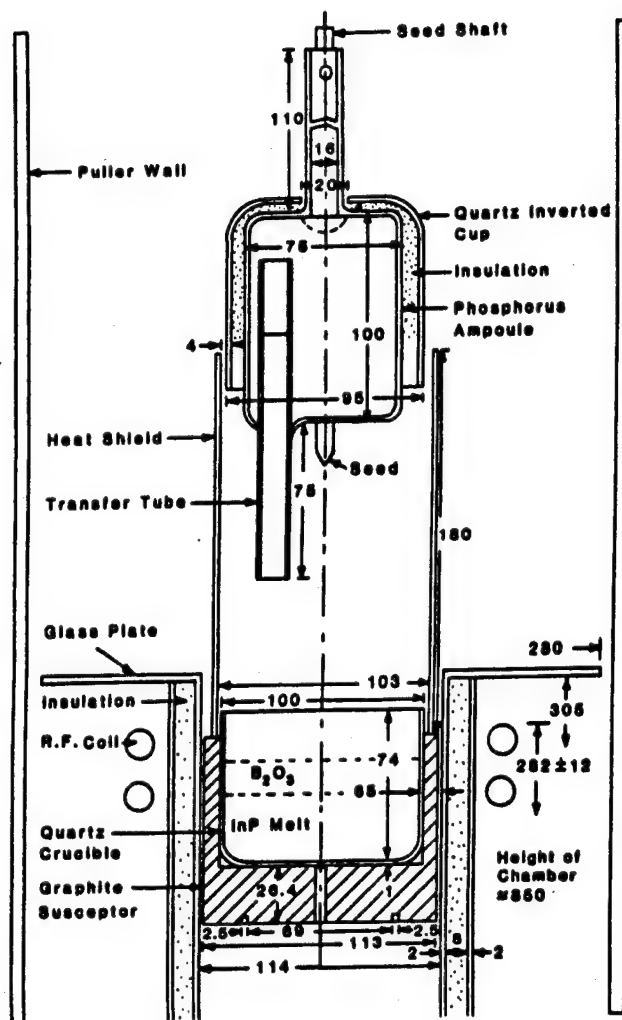


Figure 1

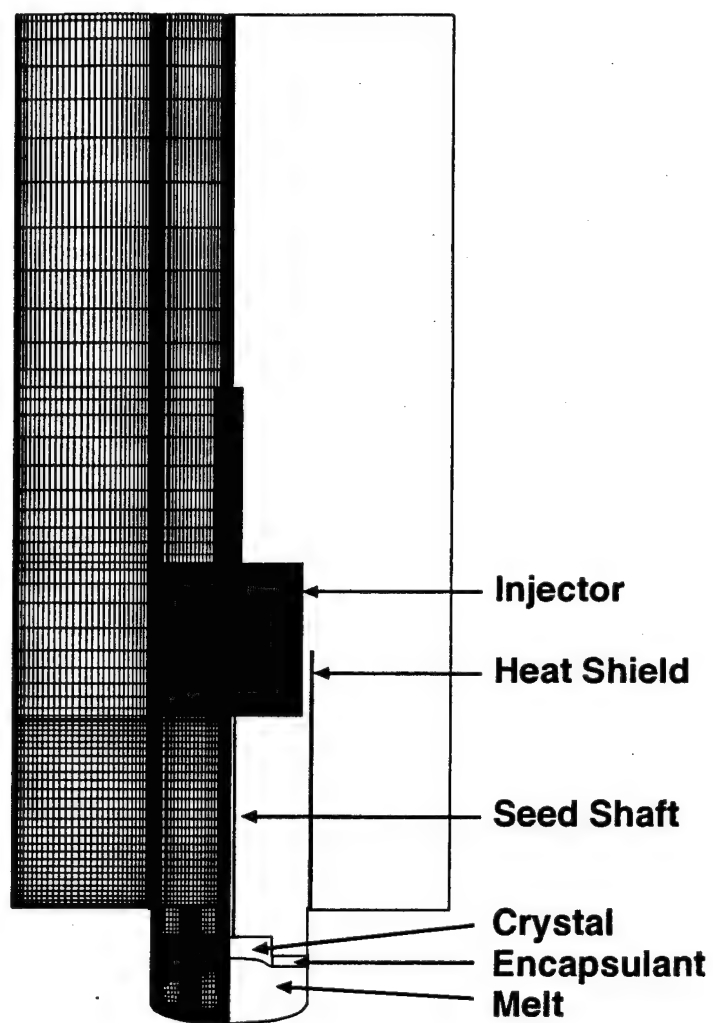
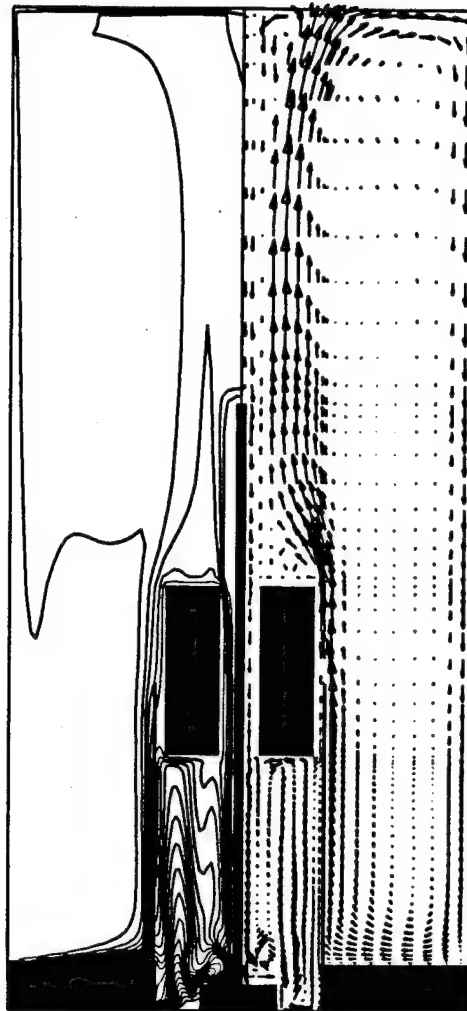
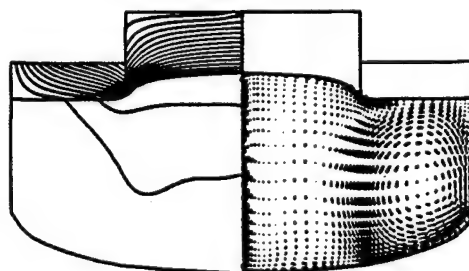


Figure 2

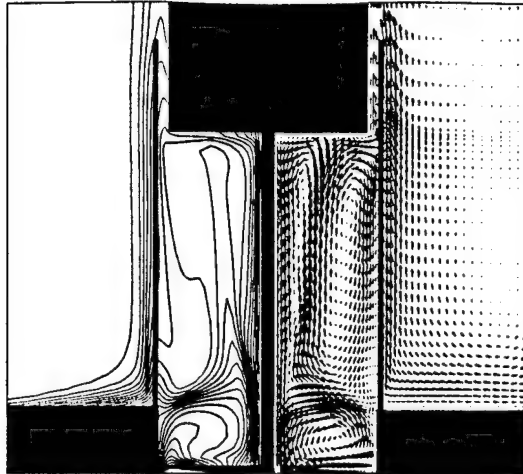


(a)

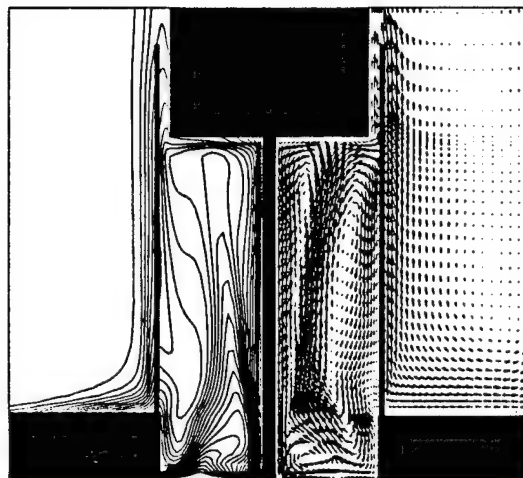


(b)

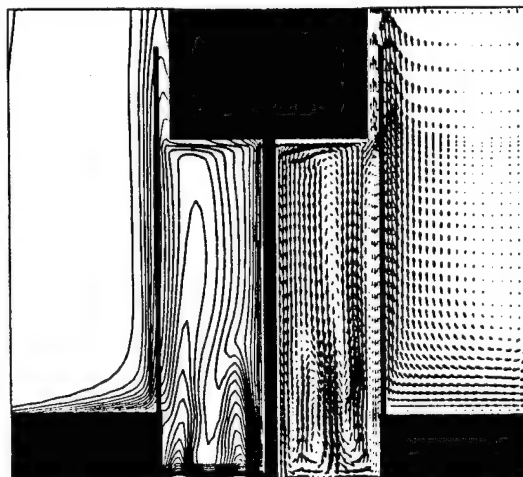
Figure 3



(a)



(b)



(c)

Figure 4

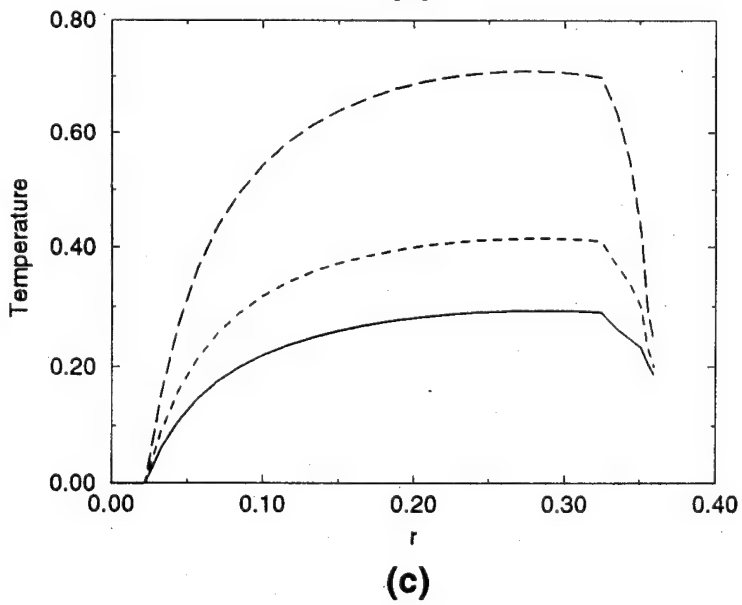
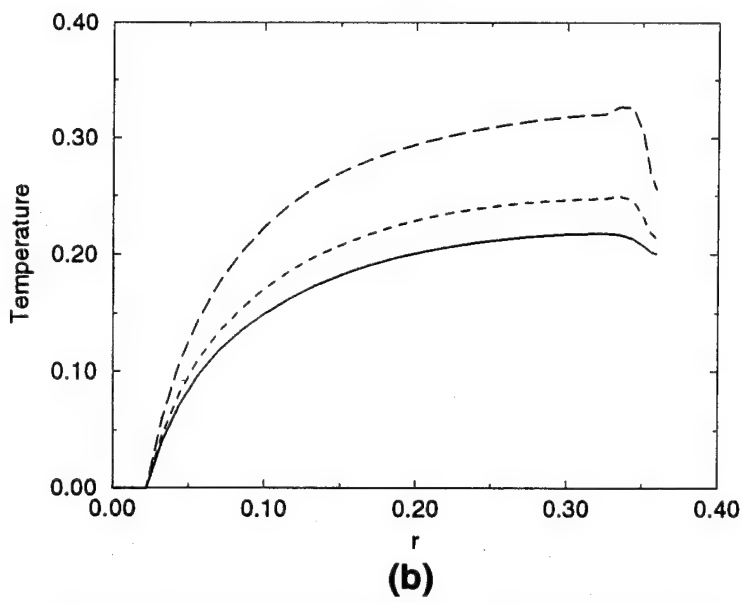
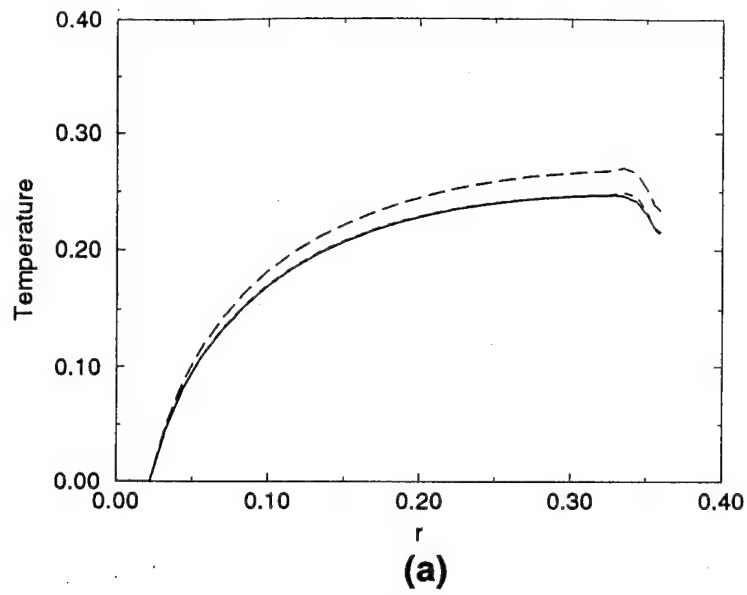
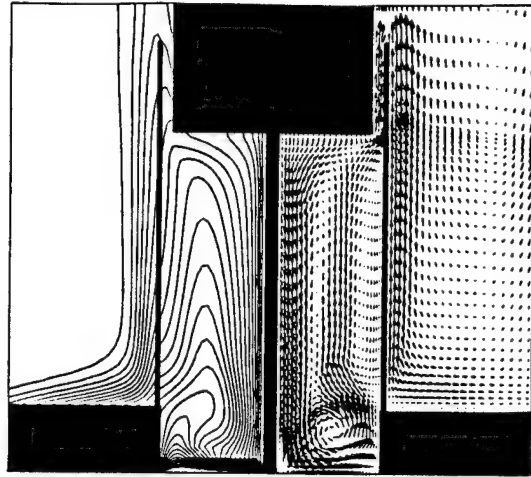
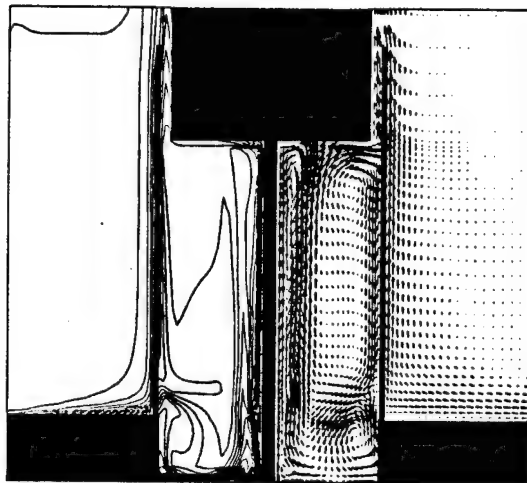


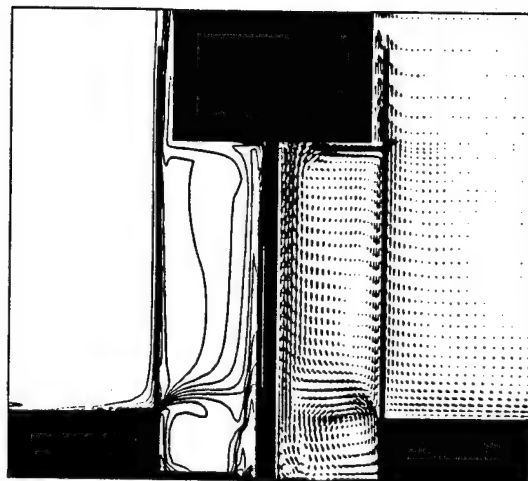
Figure 5



(a)

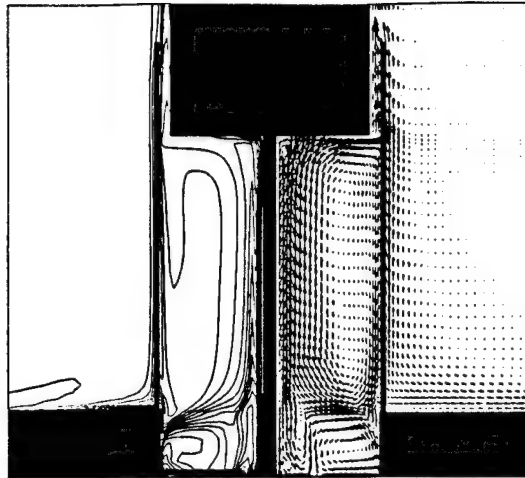


(b)

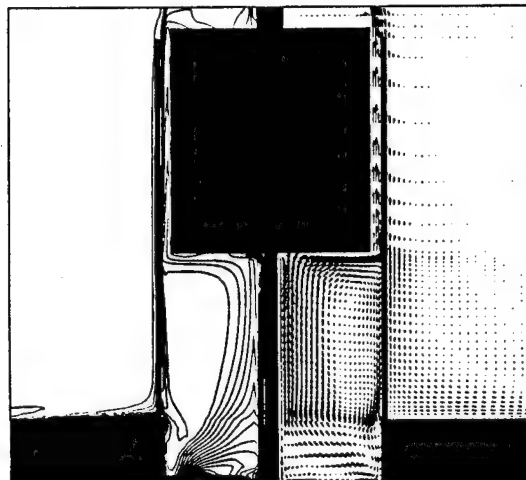


(c)

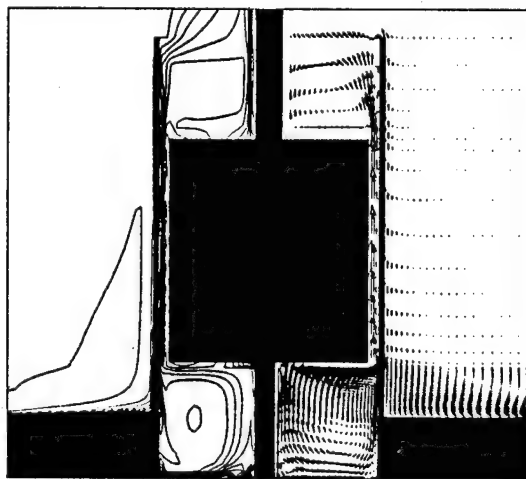
Figure 6



(a)

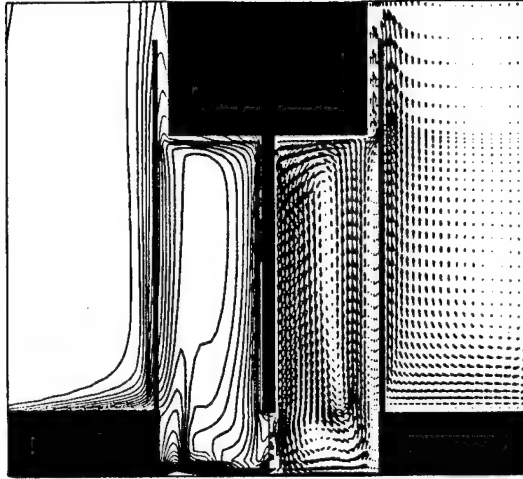


(b)

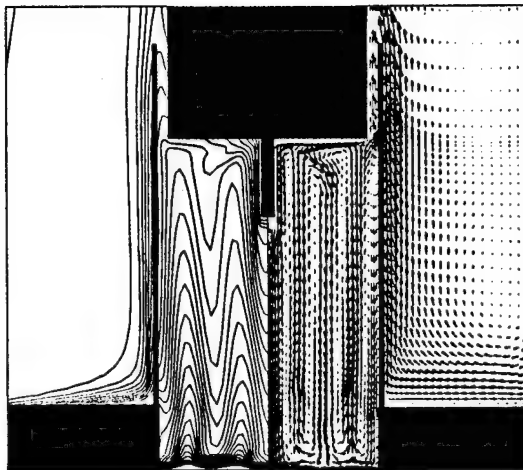


(c)

Figure 7



(a)



(b)

Figure 8

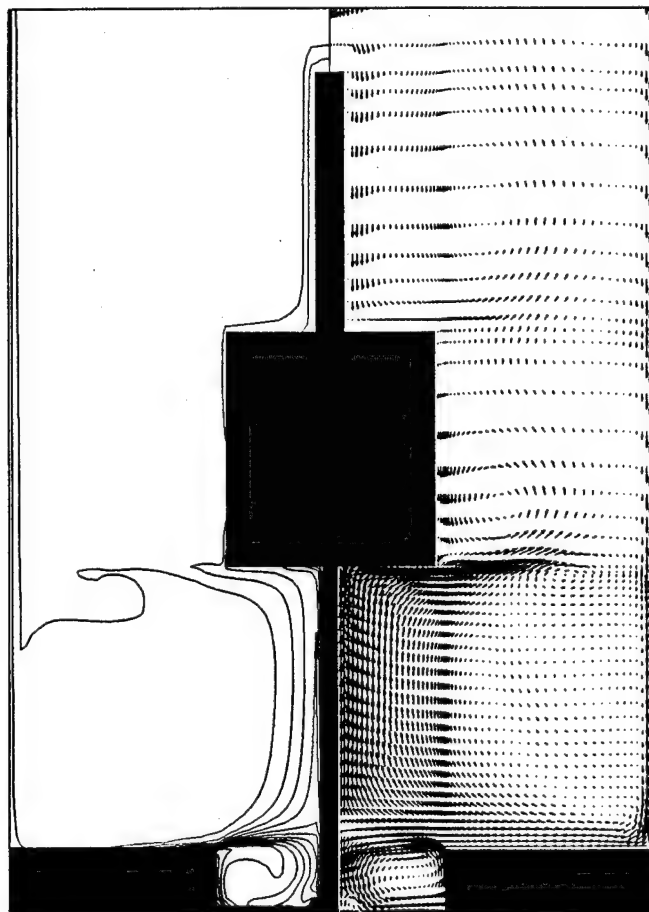


Figure 9

APPENDIX C

**TRANSPORT PHENOMENA IN HIGH PRESSURE
CRYSTAL GROWTH SYSTEMS FOR III-V COMPOUNDS**

H. Zhang and V. Prasad

Department of Mechanical Engineering
State University of New York at Stony Brook
Stony Brook, NY 11794-2300

and

D.F. Bliss

US Air Force Rome Laboratory
Hanscom AFB, MA 01731

(submitted to **Journal of Crystal Growth**)

Abstract

Transport phenomena in a high pressure crystal growth system (HPCG) are complex. A high resolution numerical scheme based on multizone adaptive finite volume discretization has been implemented to study the effect of gas recirculation on melt flow and interface shape. The model incorporates melt and gas flows induced by buoyancy and capillary forces and by crystal and crucible rotations, as well as the radiation heat loss from the melt and crystal surfaces. It is demonstrated that the thermal interaction between gas and melt must be accounted to predict the interface shape and dynamics accurately. The temperature distribution in the crystal and the shape of the melt/crystal interface also change significantly with the size of the crystal.

Research sponsored by Air Force Office of Scientific Research
and GT Equipment Technologies, Inc.

1. INTRODUCTION

Czochralski process to grow III-V compound crystals is much more complex than that for Si. It requires that the melt be covered by an encapsulant and the furnace be maintained at a high pressure to prohibit the separation of the volatile component from the melt. The presence of the gas and an encapsulant layer in a liquid-encapsulated Czochralski (LEC) or liquid-encapsulated Kyropoulos (LEK) process change the heat exchange pattern into the furnace as well as the interface and meniscus conditions and growth dynamics, compared to that in a CZ Si process. In such systems, the melt flow is oscillatory and the recirculatory inert gas flow is turbulent [1, 2]. It is therefore important to understand and analyze the mechanisms of energy transport and interaction between the gas and melt flows in moderate and high pressure crystal growth (HPCG) system which involve all modes of heat transfer, radiation, conduction and convection, and varying flow regimes. However, very little has been reported on thermal characteristics of these systems.

Numerical research on LEC growth has followed the research on CZ process for Si crystal growth [3-8]. Derby and Brown [8] developed a quasi-steady conduction model using a finite element method (FEM) that assumed an infinitely long cylindrical crystal and simplified radiation boundary conditions. Motakef and coworkers [9] studied the thermal control of LEC GaAs growth, and optimized growth conditions in conventional LEC systems through modeling effects of liquid encapsulant and boundary conditions on thermal stress. Nicodeme *et al.* [10] used a quasi-steady global finite element model in which radiation heat exchange is modeled as a surface phenomenon. Only natural convection in the melt was taken into account for the crystal/melt interface movement. Sabhapathy and Salcudean [11] used the finite volume scheme to develop a heat transfer model assuming that the encapsulant was semi-transparent to radiation and the ambient gas was maintained at a uniform and steady temperature. Also, the free surface and crystal/melt interface were assumed to be flat. Fontaine *et al.* [12] later used a commercial FEM code, FIDAP, and investigated the effects of crystal and crucible rotations.

Kinney *et al.* [13] recently developed a FEM-based integrated hydrodynamic thermal-capillary model (IHTCM) that accounts for the convection in the melt and calculates thermal stresses in the crystal. However, they had to use an artificial viscosity to force the solutions to convergence when the melt flows were strong. Dupret *et al.* [7] have also developed a computer model based on the combined use of finite element for energy equations and radiation model for surface or internal radiation heat exchange. The global models to simulate the CZ and LEC processes therefore couple the convection and radiation in the melt with the conduction in the furnace in an indirect manner (local-global iterations). The detailed procedure can be described as follows: (i) calculate global heat transfer within the furnace without the melt convection; (ii) retain the temperatures on the crucible boundary and heat fluxes on top of the melt and along the wall of the crucible; (iii) with those boundary conditions, calculate the convection in the melt and the temperature field in the crystal; (iv) use this fixed velocity field in the melt to calculate global heat transfer; and (v) return to step (ii). Typically, 4-5 iterations are needed to obtain the results.

Interestingly, numerical research on LEC growth has neglected the gas convection, and all of these studies have focused on LEC growth of GaAs crystals where the gas pressure inside the furnace was not considered to be high. In the case of InP crystal growth the chamber pressure is very high (much above 27.5 atm [14, 15]) and the flow and heat transfer interaction between the recirculating gas, the B_2O_3 surface and the crystal is highly complex and affect the crystal quality significantly [16]. Prasad *et al.* [2] have observed experimentally that the gas flow is turbulent and oscillatory in a HPCG system. Note that even the GaAs crystals are now grown at moderately high pressure (100-300 psi). There are several difficulties in using the numerical methods described above to the high pressure growth of InP and other compounds. One problem is that the energy equation for the system is decoupled from the equations of motion. When the gas flow is considered in the computational domain, temperature of various elements of the furnace are strongly coupled with the turbulent flow of the gas. The schemes based on iterative coupling between the flow and heat transfer

are expensive and many times impossible to provide converged solutions for the subdomains when a domain decomposition and/or parallel scheme is employed. Thousands of iterations may be required to achieve convergence within each time step, particularly when the gas flow is turbulent. An efficient scheme is therefore desirable for the HPCG simulation.

To simulate the transport phenomena associated with moderate and high pressure crystal growth, a high resolution computer model has been developed based on body-fitted coordinate system, multizone adaptive grid generation (MAGG) and curvilinear finite volume discretization [19-21]. In the area of multizone adaptive finite volume algorithm it concentrates on the development of an efficient algorithm for clustering of grids in the interface regions as the solutions progress, for problems involving irregular domains and free as well as moving boundaries and interfaces. A generalized set of two-dimensional governing equations for the entire multiphase crystal growth system has been derived in curvilinear coordinate system, and transformation relations for coefficients and equations for moving interfaces have been obtained. An efficient numerical scheme based on finite volume flux discretization, non-staggered grids, power law for convective fluxes, and pressure correction formulation has been implemented. The model incorporates both melt and gas flows induced by buoyancy and capillary forces and by crystal and crucible rotations, as well as the radiation heat transfer from melt and crystal surfaces. High pressure growth conditions are investigated for a wide range of parameters and interesting effects of melt/gas thermal interaction are demonstrated.

2. MATHEMATICAL MODEL

A single domain simulation has been performed to simulate the coupled melt and gas flows together with the energy transport in encapsulant and crystal. Only a limited portion of the gas region is considered here. Although gas flow will change significantly if the computational domain extends to the top surface of the HPCG furnace, the purpose of the calculations presented here is to demonstrate the robustness of the scheme, and to show the important effects of gas recirculation on high pressure crystal growth. A schematic of the HPCG system under consideration is shown in Fig. 1. The model assumes that the

system is axisymmetric, thermophysical properties in each phase are constant, the flow is incompressible, and the crystal and melt surfaces are grey and exchange radiation with the furnace walls considered as isothermal surfaces. The encapsulant/inert gas interface is assumed to be flat, and thermocapillary effects due to the gradients in the melt/encapsulant and encapsulant/inert gas interfacial tension are assumed to be negligible. (The viscosity of the encapsulant B_2O_3 is very high.) In addition, the crucible side wall and bottom are considered to be isothermally heated. The crystal pull rate is adjusted to maintain a desired crystal diameter in the simulation.

With the above assumptions, the LEC growth process is governed by conservation equations for mass, momentum, and energy in the melt, the encapsulant (B_2O_3), and the inert gas, and energy equation in the seed and crystal, which can be written in a general form as:

Continuity

$$\frac{\partial \bar{\rho}_i}{\partial t} + \nabla \cdot \bar{\rho}_i \mathbf{u}_i = 0, \quad (1)$$

Momentum conservation in axial direction

$$\frac{\partial \bar{\rho}_i u_i}{\partial t} + \nabla \cdot (\bar{\rho}_i u_i \mathbf{u}_i) = \nabla \cdot (\bar{\mu}_{i,eff} \nabla u_i) - \frac{\partial P}{\partial z} + \bar{\rho}_i Gr_i \theta, \quad (2)$$

Momentum conservation in radial direction

$$\frac{\partial \bar{\rho}_i v_i}{\partial t} + \nabla \cdot (\bar{\rho}_i v_i \mathbf{u}_i) = \nabla \cdot (\bar{\mu}_{i,eff} \nabla v_i) - \frac{\partial P}{\partial r}, \quad (3)$$

Momentum conservation in swirl direction

$$\frac{\partial \bar{\rho}_i w_i}{\partial t} + \nabla \cdot (\bar{\rho}_i w_i \mathbf{u}_i) = \nabla \cdot (\bar{\mu}_{i,eff} \nabla w_i), \quad (4)$$

Energy conservation

$$\frac{\partial \bar{\rho}_i \bar{C}_{pi} \theta}{\partial t} + \nabla \cdot (\bar{\rho}_i \bar{C}_{pi} \mathbf{u}_i \theta) = \frac{1}{Pr_m} \nabla \cdot (\bar{k}_{i,eff} \nabla \theta), \quad (5)$$

In above equations, over bar refers to the dimensionless properties and subscript i represents the various substances and phases. The equations are suitable for the entire multiphase, multicomponent domain with the provision to account for local properties and abrupt changes in transport properties across the zone boundaries, and their possible movements.

The following scales have been used to non-dimensionalize the governing equations; length: b , velocity: ν_m/b , pressure: $\rho_m \nu_m^2/b^2$, time: b^2/ν_m , density: ρ_m , dynamics viscosity: μ_m , conductivity: k_m , specific heat: C_{pm} , temperature: $\theta = (T - T_f)/(T_h - T_f)$, turbulence kinetic energy: ν_m^2/b^2 , and dissipation rate: ν_m^3/b^4 ; where subscript 'm' refers to dimensional melt properties. Here $\bar{\mu}_{i,eff}$ and $\bar{k}_{i,eff}$ are the effective dimensionless dynamic viscosity and thermal conductivity, respectively.

In the laminar melt phase, $\bar{\mu}_{i,eff} = \bar{\mu}_i$ and $\bar{k}_{i,eff} = \bar{k}_i$, and in the turbulent gas phase,

$$\bar{\mu}_{i,eff} = \bar{\mu}_i + C_\mu \bar{\rho} k^2 / \epsilon, \quad \bar{k}_{i,eff} = \bar{k}_i + C_\mu \bar{\rho} k^2 / \epsilon \cdot Pr_m / Pr_{turb}, \quad (6)$$

where Pr_{turb} is the turbulent Prandtl number.

The dimensionless turbulent kinetic energy k and its dissipation rate are obtained from the following conservation [22] equations:

$$\frac{\partial \bar{\rho}_i k}{\partial t} + \nabla \cdot (\bar{\rho}_i \mathbf{u}_i k) = \nabla \cdot \left(\frac{\bar{\mu}_{i,eff}}{\sigma_k} \nabla k \right) + S_k, \quad (7)$$

$$\frac{\partial \bar{\rho}_i \epsilon}{\partial t} + \nabla \cdot (\bar{\rho}_i \mathbf{u}_i \epsilon) = \nabla \cdot \left(\frac{\bar{\mu}_{i,eff}}{\sigma_\epsilon} \nabla \epsilon \right) + S_\epsilon, \quad (8)$$

The source terms S_k and S_ϵ are defined as

$$S_k = \bar{\mu}_t \bar{G} - \bar{\rho} \epsilon \quad (9)$$

$$S_\epsilon = C_1 \bar{\mu}_t \frac{\epsilon}{k} \bar{G} - C_2 \bar{\rho} \frac{\epsilon^2}{k} \quad (10)$$

where \bar{G} is expressed as follows in the case of the axisymmetric flows

$$\bar{G} = 2 \left[\left(\frac{\partial u}{\partial z} \right)^2 + \left(\frac{\partial v}{\partial r} \right)^2 + \left(\frac{v}{r} \right)^2 \right] + \left(\frac{\partial v}{\partial z} + \frac{\partial u}{\partial r} \right)^2 + \left(\frac{\partial w}{\partial z} \right)^2 + \left(\frac{\partial w}{\partial r} - \frac{w}{r} \right)^2. \quad (11)$$

Standard values for these constants were used in the simulation, and were obtained from [23].

The present model considers only surface radiation. The upper surface of the crystal is considered to exchange radiation with the top surface of the system using a view factor for parallel plates. Due to the computational cost, only the domain which is inside the heat shield and below the injector in the HPCG furnace for synthesis and growth of InP crystals [2, 19] has been considered in this paper. The geometric configuration considered here is quite relevant to GaAs growth furnace which is much more compact.

The boundary and interface conditions in a high pressure growth system of GaAs and InP crystals are extremely complex, and must be accounted for as accurately as possible. Most of the boundary conditions used for the present simulations are discussed in detail in [18, 19]. Some of the important conditions are as follows:

at the melt/crystal interface:

$$u = v = 0, \quad w = Re_s r, \quad \theta = 0; \quad (12)$$

at the bottom and side walls of the crucible:

$$u = v = 0, \quad w = Re_c r, \quad \theta = 1; \quad (13)$$

At the melt/crystal interface, an energy balance must consider the pull rate, the convection in the melt, the conduction in the crystal and the release of heat of fusion. For solidification of a pure substance with a definite fusion temperature T_f , implying that the solid and liquid phases are separated by a sharp interface, the position of the crystal/melt interface can be given by

$$\rho_s h_{sl} (U_{int,n} - U_s(t) \mathbf{e}_x \cdot \mathbf{n}) = k_s \frac{\partial T_s}{\partial n} - k_m \frac{\partial T_m}{\partial n}, \quad (14)$$

and the pull rate, $U_s(t)$, can be calculated from

$$U_s(t) = -(1 - Rr^2) \left\{ \frac{Ste_m}{Pr_m} \left(k_s \frac{\partial \theta_s}{\partial n} - \frac{\partial \theta_m}{\partial n} \right) \left[1 + \left(\frac{\partial s_1}{\partial r} \right)^2 \right] \right\} \Big|_{r=Rr}, \quad (15)$$

where Rr is the radius ratio. This equation is based on the assumption that the crystal and melt are not separated at the tri-junction. This implies that for given thermal boundary conditions, the pull rate is determined by the energy balance.

To obtain conditions at the melt/encapsulant and encapsulant/gas interfaces, we can assume the tangential stress at these interfaces to be zero and the normal stress exactly balanced by the externally applied stresses in the normal direction which can be written as

$$[(-p\mathbf{I} + \boldsymbol{\tau})_i \cdot \mathbf{n}] \cdot \mathbf{n} - [(-p\mathbf{I} + \boldsymbol{\tau})_{i+1} \cdot \mathbf{n}] \cdot \mathbf{n} = \frac{2H}{BoFr} \mathbf{n}, \quad (16)$$

where \mathbf{t} and \mathbf{n} are tangent and normal unit vectors, H is the mean interface curvature, \mathbf{I} is the unit tensor, Bo and Fr are the dimensionless Bond and Froude numbers, respectively, and $\boldsymbol{\tau}$ is the dimensionless stress tensor. A detailed discussion on these equations can be found in Zhang and Prasad [17, 18].

High pressure CZ processes are therefore governed by a large number of parameters such as Grashof and Prandtl numbers for the melt and gas flows; crystal and crucible Reynolds numbers; Biot number for radiation heat transfer; Froude and Bond numbers for surface tension; density, viscosity, thermal conductivity and specific heat ratios for solid and melt phases; thermophysical property variation in gas; geometric variables, and so on. These parameters vary greatly with a change in phase/zone, as well as with the surface conditions. Suitable values of these numbers need to be selected to perform realistic simulations. A major difficulty in calculating the relevant values of governing parameters in many cases is a lack of precise information on thermophysical properties as well as the variation in furnace configurations.

The governing equations for melt and crystal phases are solved iteratively and independently by invoking the quasi-steady assumption (within one time interval) for the crystal/melt interface. A successive approximation is used to track the movement of the interface. The procedure is as follows:

- (i) Assume an initial solidification and free surface locations, and generate the initial grid.

- (ii) Solve the governing equations for each phase based on the single domain system.
- (iii) Move the solidification interface based on an energy balance and move the free surface based on a normal stress balance. Underrelaxation may be needed to control large variations in the interface shapes.
- (iv) Regenerate the grids and return to step 2 until all equations and boundary conditions are satisfied.

3. NUMERICAL METHOD

To overcome the difficulties associated with time-varying domains and irregular boundaries, many different kinds of algorithms have been proposed based on the choice of (a) the numerical method, e.g., finite element, finite difference and finite volume, and (b) the selection of the mesh system, e.g., fixed and moving grid fields. Several commercial and non-commercial software are now available that can simulate these kinds of processes. Most of these computer models are based on finite element method [7] primarily because it is inherently suitable for complex geometries as well as for the stress calculations.

We have recently developed a high resolution numerical scheme, MASTRAPP, based on the finite volume scheme, that is specially suitable for multiphase, multicomponent transport systems. The numerical scheme employs (a) a multizone adaptive grid generation (MAGG) for the discretization of physical domains of arbitrary shapes by using an adaptive optimization of grid characteristics, and (b) a curvilinear finite volume (CFV) scheme for the discretization of the governing equations. The MAGG technique is much more efficient and has better characteristics for phase change and free surface problems than the methods commonly used, particularly by the commercial packages. The scheme allows smoothness and orthogonality in the vicinity of the internal interfaces, and has proved to be very powerful and robust for thermal and flow interactions at the melt/solid, melt/gas and solid/gas interfaces [17-21]. This is primarily because the equations for direct and dynamic link between

the zonal and interfacial grid generation have been developed based on a constrained variational optimal method. Since it uses a TDMA solver for the CFV, the memory requirement is small and the solution process is fast. The solution adaptivity further makes the solution procedure fast and accurate. More details can be found in Zhang and Prasad [17].

All simulations were performed on SparcStation 10. For 82×42 nodes, approximately 10 hours is required to attain convergence for steady solutions, and approximately 50 hours is required for periodic oscillatory solutions.

4. RESULTS AND DISCUSSION

Figure 1 shows a schematic and grid distribution for the system. A structured grid arrangement is used here. The grid lines maintain smoothness and continuity in the computational domain. The grids always remain clustered in the interface regions and near the boundaries. All of the interfaces, e.g., crystal/melt, encapsulant/melt, encapsulant/gas, side wall of the crystal, and upper surface of the crystal are preserved, allowing the grid points to move along these surfaces. The present algorithm also redistributes the grids automatically as the crystal is grown. e.g., a smaller number of nodes are used in the crystal when it is short, but they increase with the size of the crystal.

Figures 2 to 6 show the temperature and flow fields in a high pressure furnace for the growth of III-V compound crystals. The thermophysical parameters used in the simulation are $We = 2.5 \times 10^{-5}$, $Fr = 10^{-8}$, $\rho_s/\rho_m = 1.0$, $k_s/k_m = 0.40$ and $C_s/C_m = 0.96$ based on available data in the open literature for InP. The contact angles at both the side wall of the crystal and the side boundary are taken as 45 degrees, and are not allowed to change with the pull rate of the crystal. These parameters have not been changed for the calculations presented in this paper.

As noted earlier, in the growth of InP crystal the side boundary of the computational system is located on the quartz heat shield. The heat transfer takes place at this boundary by convection to the recirculating gas in the region outside the heat shield and also by radiation to the cold walls of the furnace. The entire gas furnace needs to be considered

to determine an accurate temperature distribution on the heat shield. However, large CPU time and memory are required to perform the calculations. In this paper, we focus on the region near the crystal/melt interface, and only a portion of the furnace is considered. However, we need to prescribe reasonable boundary conditions on the shield wall. Figure 2 shows the effects of the side wall boundary condition on crystal/melt interface as well as on temperature distribution in the crystal. Four kinds of boundary conditions have been considered and are shown in Fig. 2. The parameters used in the simulation are the Grashof Numbers, $Gr_m = Gr_g = 10^7$, and the rotation rates of the crystal and crucible, $Re_c = -Re_s = 10^3$. (Note that the Grashof number for the gas will be much higher if Gr_g is based on the height of the system.) The upper portion of the seed shaft remains at a cold temperature as in the real situation.

Figure 2(a) presents the velocity field and temperature distribution in the gas and melt phases when the side wall is maintained at a cold temperature. Heat loss takes place at the crystal/gas and melt/encapsulant interfaces. Due to strong cooling effect on the crystal surface, a concave shape of the crystal/melt interface is obtained. The flow field in the melt shows that the buoyancy is a dominant force. The melt flows upward along side wall of the crucible and downward in the central region of the crucible. The flow pattern underneath the crystal is quite complex and an oscillating behavior is observed in this region. The temperature profile in the melt is distorted. Figure 2(b) shows the velocity field and temperature distribution in the gas and melt phases when the side wall beyond the encapsulant height is considered cold. (The crystal extends beyond the encapsulant level.) A cold temperature is therefore maintained above the edge of the crucible, as shown in the figure. The upper portion of the crystal is now heated due to convective heat exchange with the hot wall of the crucible, while the lower portion of the crystal loses heat by diffusion through the encapsulant layer. The crystal/melt interface is now doubly curved. The flow pattern in the gas is quite complicated. The melt flow is very similar to that presented in Fig. 2(a).

Figure 2(c) shows the results for a given temperature profile on the side wall. This

represents the heat shield temperature distribution obtained in the companion paper [19]. A high temperature is used in a short distance just above the encapsulant, as a part of the crucible. A linear temperature with large gradient follows beyond the crucible wall and a smaller temperature gradient exists on the rest of the side wall. The crystal is again heated in the upper portion and cooled down in the bottom part. A convex shape of the crystal/melt interface is observed in this case. As shown in the figure, the gas flows downward along the seed shaft until it reaches the crystal, and one recirculatory cell is located directly above the encapsulant free surface while two slender cells exist in the upper region. The melt flow is again similar with that in Figs. 2(a)-(c). Figure 2(d), on the other hand, presents the results of an insulated heat shield wall. The flow pattern and temperature distribution are quite similar to those in Fig. 2(c). However, the interface shape is slightly changed due to the change in temperature distribution on the heat shield. These results confirm that the gas convection plays an important role in high pressure crystal growth, and an accurate boundary condition at the side wall has an important influence on the crystal/melt interface.

The effect of radiation loss from crystal/gas and melt/encapsulant interfaces is presented in Fig. 3. The parameters used in these simulations are the Grashof Numbers, $Gr_m = Gr_g = 10^7$, and the rotation rates of the crystal and crucible, $Re_c = -Re_s = 10^3$. A large and long crystal has been used in the simulation to accentuate the effect of radiation from the crystal surface. The encapsulant layer is considered as transparent, and the heat shield is insulated. The radiation coefficient, σ_r , is assumed to be 0.1, 0.2, and 0.4 in Fig. 3(a), 3(b) and 3(c), respectively. The temperature gradient in the region directly above the crystal/melt interface becomes large as the heat loss from the crystal surface increases due to an increase in the radiation coefficient. The center of the crystal/melt interface moves up, and the shape of the interface is changed from a convex to a concave profile. In the melt, one thin shallow cell is produced directly under the crystal due to its rotation. The primary cell in the melt is due to the combined effects of buoyancy and the crucible rotation. The flow moves up along the side wall of the crucible, turns to the center on the top of the melt, and

then goes downward under the crystal. A small cell is found at the bottom of the crucible in the central region. The melt flow is much stronger in Fig. 3(c) due to an increase in heat transfer and a larger melt volume. Calculations were also performed for a short crystal using the exact same parameters. The heat transfer phenomena and melt flow behavior due to a change in σ_r remain unchanged.

Previous models [30, 31, 32] using an average heat transfer coefficient have assumed that the effect of gas flow on crystal surface is to produce the cooling effect. Obviously, our simulation does not support this assumption and suggests that both heating and cooling may be produced in different regions of the crystal surface. The temperature distribution in the crystal will directly affect the stress distribution in the crystal and the shape of the crystal/melt interface. The present results demonstrate that this distribution is determined by the boundary condition of the side wall, interaction between the gas and melt convection, radiation heat exchange within the furnace, and conduction heat transfer in the encapsulant as well as in the seed.

Figure 4 presents the flow and temperature fields for three different gas Grashof numbers, $Gr_g = 10^6, 10^7$, and 10^8 with $Gr_m = 10^7$, $\sigma_r = 0.2$, and the rotation rates of the crystal and crucible, $Re_c = -Re_s = 4 \times 10^3$. The ratio of the crystal and crucible diameters is $1/3$. The overall flow pattern in the gas is quite similar to that observed in Fig. 3. However, the gas flow is much stronger in this case since the diameter and length of the crystal are smaller. Figure 4(c) shows the strongest gas flow. The shape of the crystal/melt interface is again changed from convex to concave. The temperature distribution in the gas as well as in the interface region of the crystal is further distorted as the gas flow becomes stronger. The flow field in the melt underneath the crystal is quite similar with that in Fig. 3. The rotation dominated flow patterns have been shown in Figs. 4(a) to 4(c) comparing with those in Figs 3(a) to 3(c). A similarity in the interface behavior and heat transfer phenomena between Fig. 3 and Fig. 4 is evident, and can be attributed to the enhancement in heat transfer from the crystal surface whether it is due to an increase in radiation or the gas

convection.

Figures 5 and 6 show the effect of the crystal size on velocity field and temperature distribution. The thermophysical parameters used in this case are similar to the one used earlier, with $Gr_m = Gr_g = 10^7$ and $Re_c = -Re_s = 10^3$. The side wall is insulated and top wall is cold. As is well known, the level of the melt continuously drops as the crystal is grown. As noted earlier, the number of nodes in the computational subdomain for crystal is small when the crystal is short, and it increases as the crystal is grown. As a result, the total number of nodes in the gas region decreases. On other hand, the number of nodes in the melt and in the encapsulant layer remains constant although the level of the melt drops in this case. The total number of nodes is also kept constant. An interpolation of field variables is employed after the grid redistribution. The success of the algorithm in node migration is demonstrated in Figs. 5(a) and 5(b).

Figure 6(a) shows the flow field and temperature distribution when the crystal is short. The level of the melt is highest at this time. There is one large cell under the free surface due to buoyancy and one small cell underneath the crystal due to combined effects of natural convection and rotation. The temperature distribution is again distorted. Figure 7 shows the non-dimensional heat flux (heat gain on the crucible wall) for a short period of time for case (a) in Fig. 6. The length of the crystal remains almost unchanged for this short time period. The oscillation seems periodic with at least two frequencies and small amplitudes.

As the crystal is grown, the level of the melt drops. The two-cell structure of the melt flow gradually changes to a three-cell structure. The temperature distribution also changes with respect to the flow field. The temperature on the top surface of the crystal decreases from Fig 6(a) to 6(f) due to an increase in the view factor. The crystal/melt interface changes gradually from a convex to a concave shape. The overall flow and temperature fields in the gas region change a little. The gas flows downward on the seed and the crystal, and after gaining heat from the encapsulant surface moves up along the side wall. When the crystal is short, the gas flow does not create a cell directly on the surface of the encapsulant, and

the cells are slender and extend to the top of the domain. In general, the size of the crystal has a complex effect on the gas and melt flow fields as well as on the crystal/melt interface.

5. CONCLUDING REMARKS

The growth of III-V compound crystals with a focus on InP has been simulated by a multizone adaptive process model (a) to demonstrate the effectiveness of the MAGG scheme to simulate multiphase systems with more than one material, and free and moving interfaces; and (b) to show the complexity of the flow structure and temperature field in a HPCG system. It is found that a portion of the crystal may be heated by convection from the hot crucible wall while the other portion of the crystal is cooled by convection losses to the cold walls. The radiation and conduction models, that neglect convection in the gas, and have been widely used in the literature are not valid for the HPCG growth. The convective heat transfer also plays a key role in setting up the interface and boundary conditions. The temperature distribution on the surface boundary is usually determined by both the convective and radiative heat transfer. Cooling on the top of the crystal also has a significant effect on the temperature distribution in the crystal, the shape and dynamics of the crystal/melt interface, and the pulling velocity. As the crystal is grown, the flow pattern as well as the shape of the crystal/melt interface are changed drastically. In the case of a small crystal, the convective heat transfer has a stronger influence due to a large volume of the gas and a short distance between the top surface of the crystal and the crystal/melt interface. On the other hand, the side wall boundary condition plays an important role in determining the crystal/melt interface and temperature distribution in the crystal when the crystal is long. Calculations presented here are only preliminary but they serve the purpose of demonstrating the strong effects gas convection can have on the high pressure growth.

ACKNOWLEDGMENTS

This research has been supported by the AFOSR program in Computational Mathematics and GT Equipment Technologies (through a small business technology transfer research grant

from AFOSR). Acknowledgments are also due to A. Anselmo at Rome Laboratory for helpful discussions.

Nomenclature

\mathbf{n}	normal unit vector
\mathbf{t}	tangential unit vector
\mathbf{u}	velocity vector
Ar	aspect ratio, h^*/b
Bi_r	radiation Biot number, $\epsilon\sigma_r F(T^2 + T_\infty^2) \times (T + T_\infty)b/k_m Pr_m$
Bo	Bond number, $\rho gb^2/\sigma$
C_p	specific heat ($J\ kg^{-1}K^{-1}$)
F	View factor
Fr	Froude number, ν^2/gb^3
G	turbulence product ($J\ m^{-3}s^{-1}$)
Gr	Grashof number, $g\beta b^3(T_h - T_\infty)/\nu^2$
H	curvature of the free surface
P	pressure, $P^*b^2/\rho_m\nu_m^2$
Pr	Prandtl number, ν/α
Re	Reynolds number, $\omega b^2/\nu_m$
Rr	radius ratio, a/b
S	source
Ste_m	liquid Stefan number, $C_{pl}(T_h - T_f)/h_{sl}$
T	temperature (K)
U_s	dimensionless pulling rate
a	crystal radius (m)
b	crucible radius (m)
g	acceleration due to gravity (m^2/s)
k	thermal conductivity ($W\ m^{-1}K^{-1}$) also, turbulence kinetic energy, k^*b^2/ν_m^2
h_{sl}	latent heat of fusion ($J\ kg^{-1}$)
r	radial distance, r^*/b
s_1	crystal/melt interface height, s_1^*/b
t	time, $t^*\nu_m/b^2$
u	velocity in axial direction, u^*b/ν_m
v	velocity in radial direction, v^*b/ν_m
w	velocity in swirl direction, w^*b/ν_m
z	axial distance, z^*/b
Γ	diffusion coefficient
α	thermal diffusivity (m^2s^{-1})
β	thermal expansion coefficient (K^{-1})
ρ	density (kg/m^3)
μ	dynamic viscosity ($kg\ m^{-1}s^{-1}$)
ν	kinematic viscosity (m^2s^{-1})
σ	Stefan-Boltzman constant ($W\ m^{-2}K^{-4}$) also, turbulence parameters
τ	stress tensor (Pa)

ϵ	emissivity also, turbulence dissipation rate, $\epsilon^* b^4 / \nu^3$
θ	dimensionless temperature, $(T - T_\infty) / (T_h - T_\infty)$

Subscripts

c	crucible
e	encapsulant
eff	effective
f	freezing temperature
g	gas
h	hot wall
int	interface
k	kinetic energy
m	melt
r	radiation
s	crystal
t	temperature
$turb$	turbulence
ϵ	dissipation rate
∞	infinity

Superscripts

*	dimensional
—	nondimensional properties

References

- [1] G. Muller, J. Volkl and E. Tomzig, *J. Crystal Growth*, 64 (1983) 40.
- [2] V. Prasad, D. F. Bliss and J. A. Adamski *J. Crystal Growth* 142 (1994) 21.
- [3] J. Volkl and G. Muller, *European Materials Research Society Symposia Proceedings*, 16 (1987) 141.
- [4] D.T.J Hurle, *J. Crystal Growth* 65 (1983) 124.
- [5] D.T.J. Hurle and B. Cockayne, in: *Bulk Crystal Growth*, Ed. D.T.J. Hurle (North-Holland, New York, 1994).
- [6] R. A. Brown, *AIChE Journal* 43 (1988) 881.
- [7] F. Dupret and N.V.D. Bogaert, in: *Bulk Crystal Growth*, Ed. D.T.J. Hurle (North-Holland, New York, 1994).
- [8] J. J. Derby and R. A. Brown, *J. Crystal Growth* 74 (1986) 605.
- [9] S. J. Motakef, *J. Applied Mechanics* 54 (1987) 813.
- [10] P. Nicodeme, F. Dupret, M. J. Crochet, J. P. Farges and G. Nagel, in: *Semi-Insulating III-V Materials*, proc. 5th Conf. Semi-Insulating III-V Materials (Malmo, Sweden, June, 1988), Eds. G. Grossman and L. Ledebro (Higer, Bristol, 1988).
- [11] P. Sabhapathy and M. E. Salcudean, *J. Crystal Growth* 97 (1989) 125.
- [12] J. P. Fontaine, A. Randriamampianina, G. P. Extremet and P. Bontoux, *J. Crystal Growth* 97 (1989) 453.
- [13] T. A. Kinney, D. E. Bornside, R. A. Brown and M. K. Kim, *J. Crystal Growth* 126 (1993) 413.
- [14] A. S. Jordan, *J. Crystal Growth* 71 (1985) 551.
- [15] A. S. Jordan, *J. Crystal Growth* 71 (1985) 559.
- [16] D. F. Bliss, R. M. Hilton, S. Bachowski and J. A. Adamski, *J. Electronic Materials* 20 (1991) 967.
- [17] H. Zhang and V. Prasad, "A Multizone Adaptive Process Model for Czochralski Crystal Growth at Low and High Pressures," *J. Crystal Growth* (in press).
- [18] H. Zhang and V. Prasad, *Proceeding (1995), ASME/JSME Thermal Engineering Joint Conference, Maui, Hawaii*, pp. 559-568.
- [19] H. Zhang, V. Prasad and D. F. Bliss, *Transport Phenomena in a High Pressure Crystal Growth System: In-situ Synthesis for InP Melt*, *J. Crystal Growth* (Submitted).
- [20] H. Zhang and M. K. Moallemi, "A Multizone Adaptive Grid Generation Technique for Simulation of Moving and Free Boundary Problems," *Numerical Heat Transfer* (in press).
- [21] H. Zhang, V. Prasad and M. K. Moallemi, "A Solution Adaptive Scheme for Deformable Free Surface Flow and Heat Transfer Problems," *National Heat Transfer Conference, Portland, August (1995)*.

- [22] B. Farouk and S. I. Guceri, *J. Heat Transfer*, 104 (1982) 228.
- [23] B. E. Launder, *Turbulence, Topics in Applied Physics*, 12 (Springer, Berlin, 1978).
- [24] J. R. Ristorcelli and J. L. Lumley, *J. Crystal Growth* 116 (1992) 447.
- [25] N. Ono, M. Kida, Y. Arai and Y. Sahira, *J. Crystal Growth* 137 (1994) 427.
- [26] K.C. Karki and S.V. Patankar, *Numerical Heat Transfer* 14 (1988) 295.
- [27] H.J. Kim and J.F. Thompson *AIAA Journal* 28 (1990) 470.
- [28] H. Kopetsch, *J. Crystal Growth* 102 (1990) 505.
- [29] K. Koai, A. Seidl, H.-J. Leister, G. Muller, A. Kohler, *J. Crystal Growth* 137 (1994) 41.
- [30] A.S. Jordan, R. Caruso, and A. R. Von Neida, *The Bell System Technical Journal* (1980), pp. 593-637.
- [31] A.S. Jordan, A.R. Von Neida and R. Caruso, *J. Crystal Growth* 70 (1984) 555.
- [32] K. W. Kelly, K. Koai and S. Motakef, *J. Crystal Growth* 113 (1991) 254.

- Figure 1 Grid distribution for a high pressure system.
- Figure 2 Effect of side wall boundary condition on the crystal/melt interface, flow field and temperature distributions for $Gr_m = Gr_g = 10^7$, $Re_c = -Re_s = 10^3$ and $\sigma_r = 0.2$, (a) cold temperature, (b) cold temperature beyond the crucible height, (c) a given temperature profile, and (d) zero heat flux.
- Figure 3 Effect of radiation loss from the crystal top and side walls for $Gr_m = Gr_g = 10^7$, $Re_c = -Re_s = 10^3$, and (a) $\sigma_r = 0.1$, (b) $\sigma_r = 0.2$, (c) and $\sigma_r = 0.4$.
- Figure 4 Effect of gas flow strength on crystal/melt interface for $Gr_m = 10^7$, $Re_c = -Re_s = 4 \times 10^3$, $\sigma_r = 0.2$ and (a) $Gr_g = 10^6$, (b) $Gr_g = 10^7$, and (c) $Gr_g = 10^8$.
- Figure 5 Grid distribution for $Gr_m = Gr_g = 10^7$, $Re_c = -Re_s = 10^3$, and $\sigma_r = 0.2$ with different crystal heights, (a) 15 mm and (b) 90 mm.
- Figure 6 Effect of crystal height on the crystal/melt interface for $Gr_m = Gr_g = 10^7$, $Re_c = -Re_s = 10^3$, and $\sigma_r = 0.2$ with different crystal height, (a) 15 mm, (b) 30 mm, (c) 45 mm, (d) 60 mm, (e) 75 mm, and (f) 90 mm.
- Figure 7 Oscillation in heat flux when the crystal is short, corresponding to the case in Fig. 6(a).

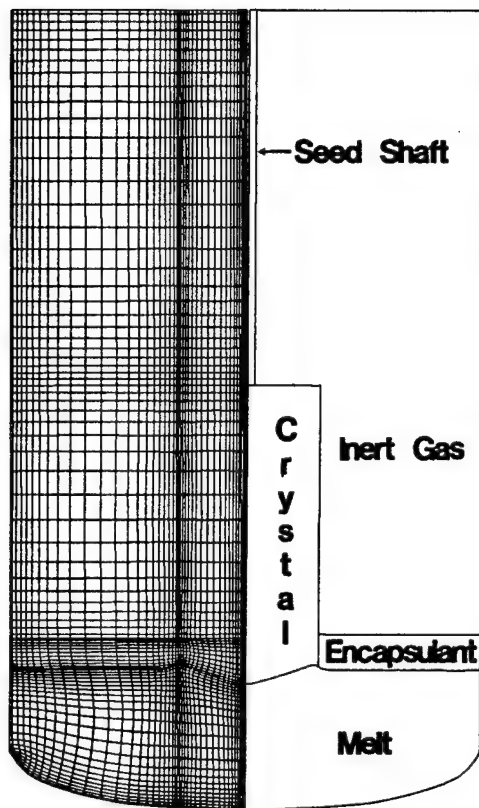
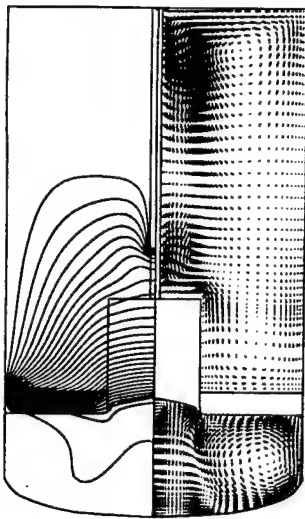
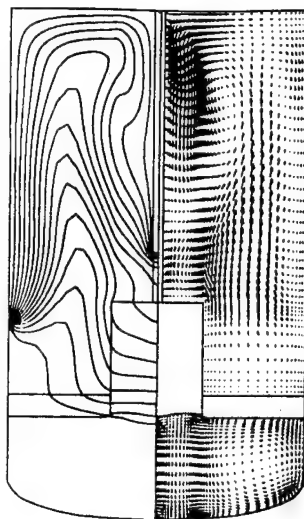


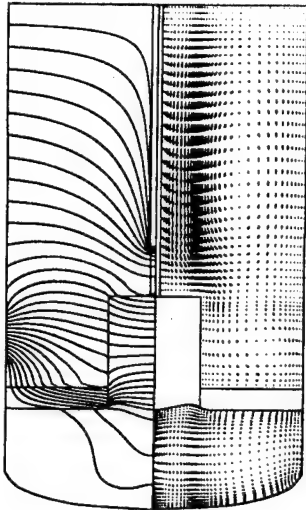
Figure 1



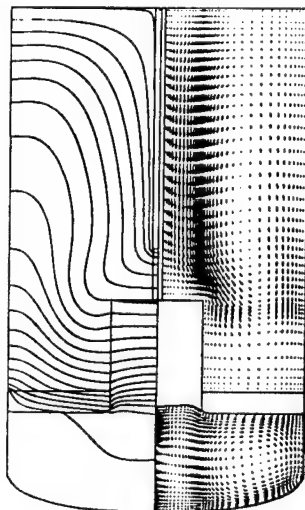
(a)



(b)



(c)



(d)

Figure 2

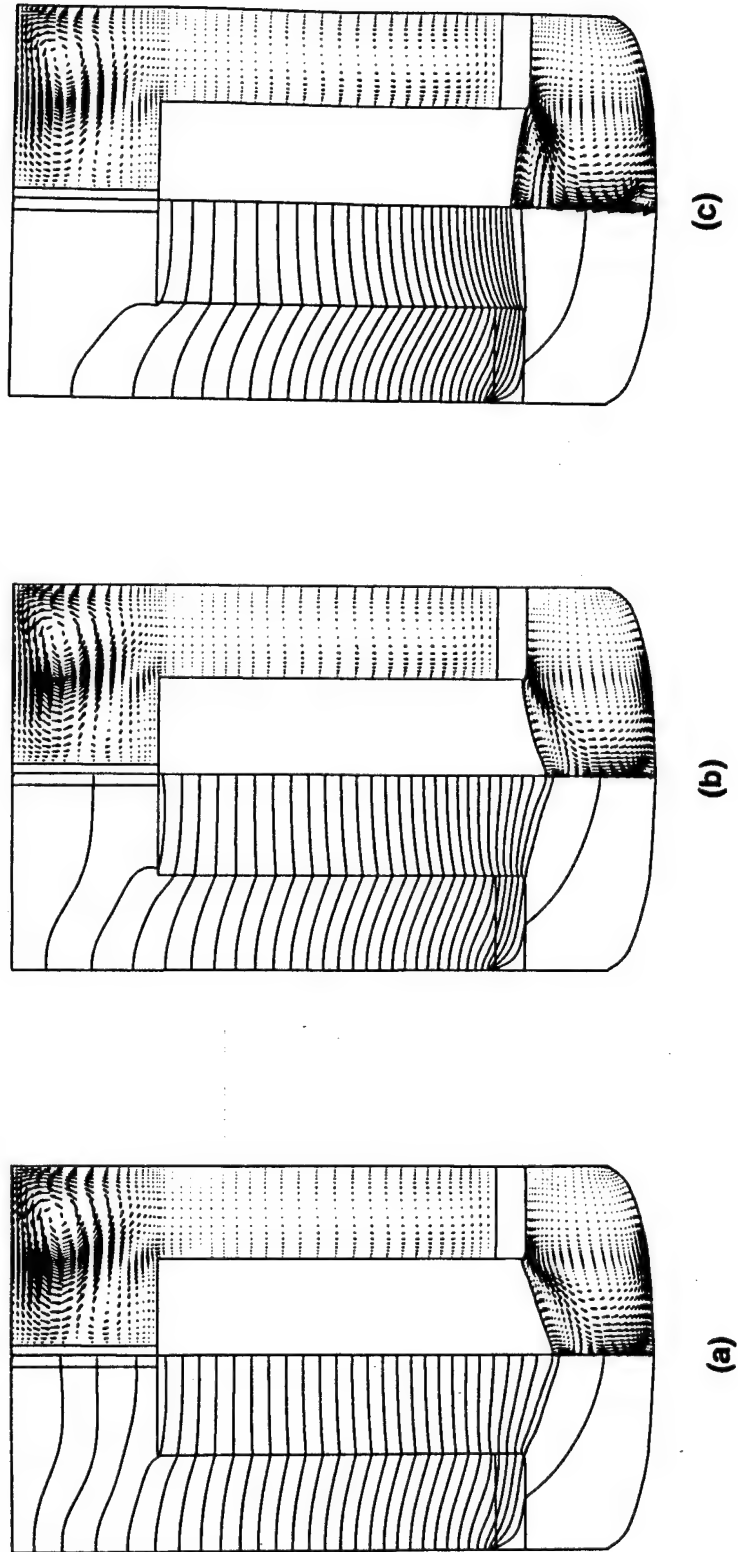


Figure 3

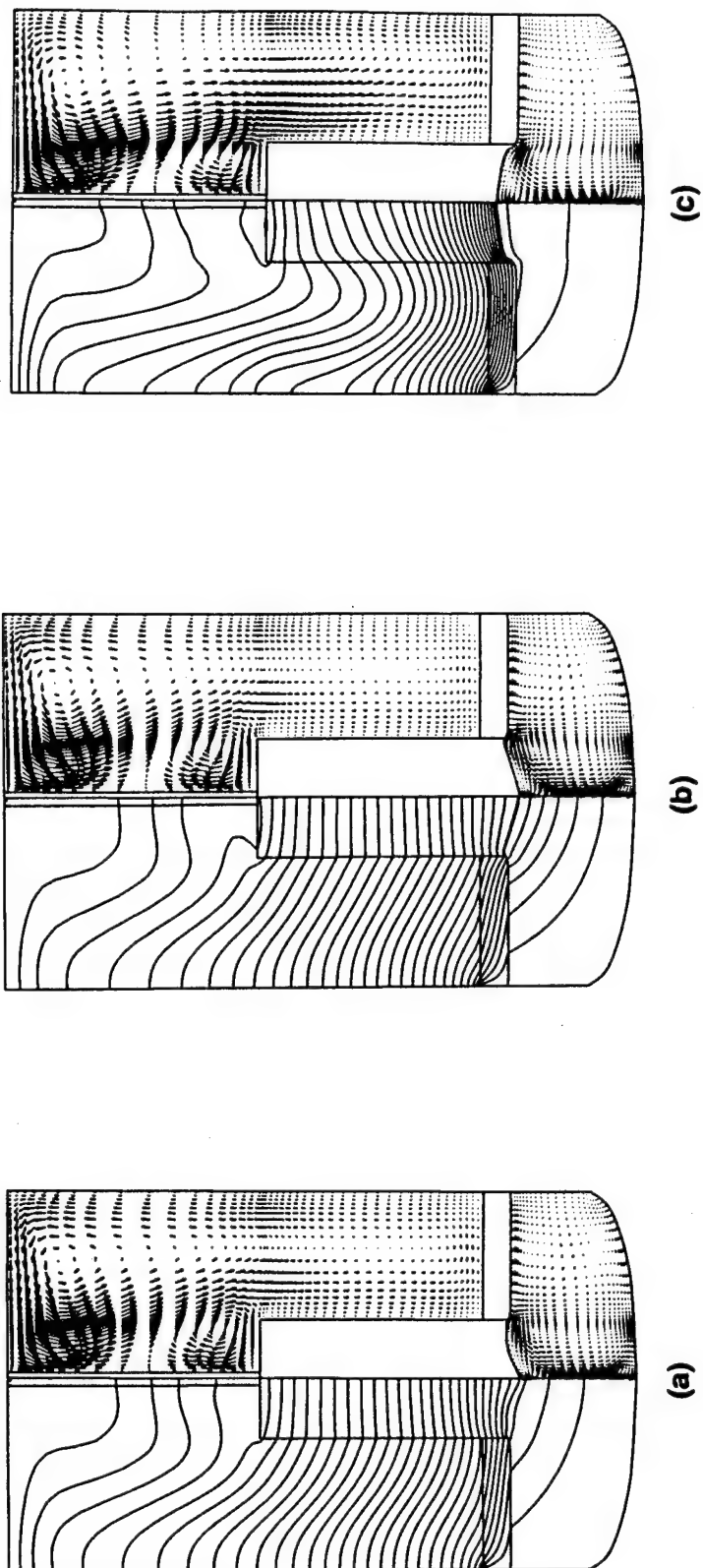
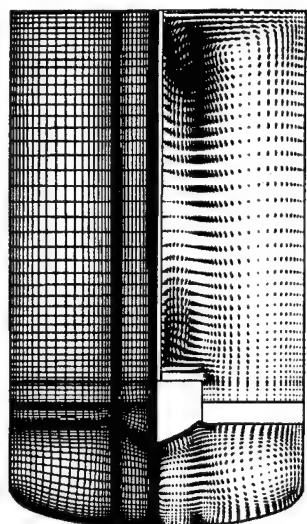
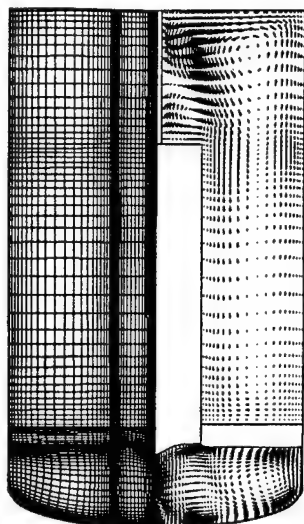


Figure 4



(a)



(b)

Figure 5

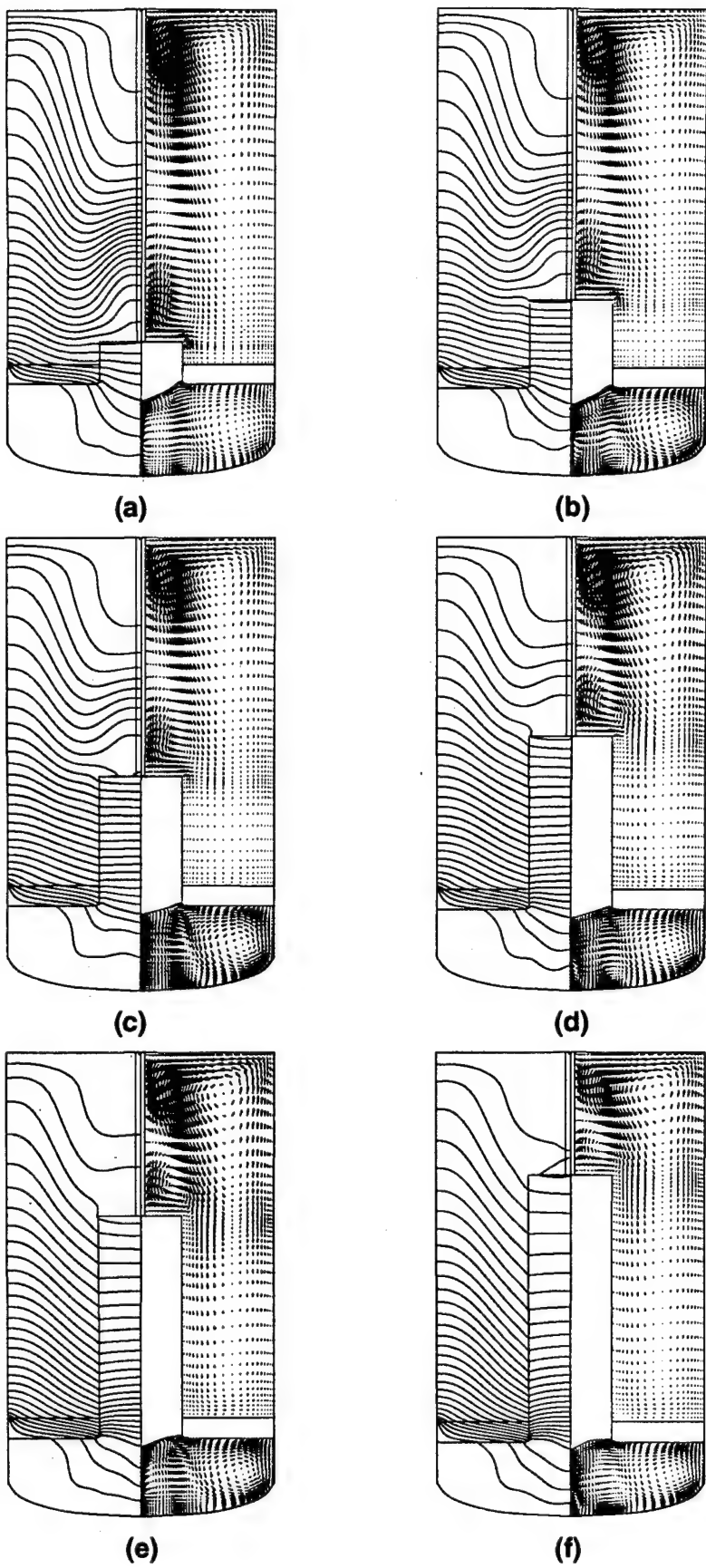


Figure 6

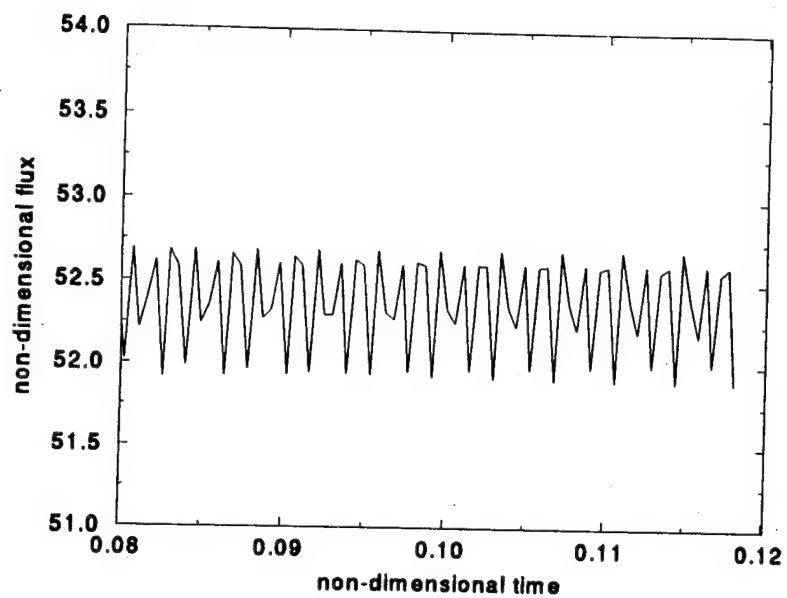


Figure 7

APPENDIX D

Dynamics of Melt-Crystal Interface and Coupled Convection-Stress Predictions for Czochralski Crystal Growth Processes

Y. F. Zou, H. Zhang, and V. Prasad

Process Modeling Laboratory,

State University of New York, Stony Brook, NY 11794-2300

Abstract

A coupled thermal-elastic model is developed to study the transport phenomena of Czochralski crystal growth and thermal stresses in the grown crystal, both at low- and high-pressures. A multizone adaptive scheme for transport and phase-change processes (*MASTRAPP*) is used to predict the melt and gas flows as well as the temperature distribution. Using the grid-field and temperature distributions generated by *MASTRAPP* a finite-element software package, *ALGOR* calculates the stresses in the crystal. The numerical results demonstrate that the convective flows in both the melt and the gas have significant effects on thermal stresses in the crystal. Indeed, a realistic model for a high-pressure CZ process must account for thermal interaction between the melt and the gas. Also, the novel approach of combined finite-volume/finite-element methods can be successfully used for thermo-mechanical problems.

1 Introduction

Control of thermal stresses is important for the final quality of Czochralski (CZ) grown crystals. Extensive research has, therefore, been carried out in recent years to model and predict the stress distribution in the crystal. Following the pioneering work of Jordan et al. [1], several investigators employed either analytical or finite element methods to calculate these stresses. However, the early analyses generally isolated the crystal from the furnace, neglected the influence of the melt flows, and assumed the melt/crystal interface as either planar or some other known shape. Motakef [2,3], Dupret [4], Bornside [5], and their co-workers later improved the stress models and used a conduction-radiation global model to

perform a finite element analysis. The effects of melt convection on stresses in the oxide single crystal was investigated by Nobuyuki et al. [6]. Kinney [7,8] and co-workers later developed a comprehensive computer model to predict thermal stresses which could also account for the melt convection. In the case of moderate or high-pressure LEC growth of III-V compounds, these studies either assumed that the gas recirculation is non-existent or used an average heat transfer coefficient for convective losses from the melt to the gas.

Recently, it has been demonstrated by Prasad and co-workers [9-11] that the gas flow significantly influences the melt conditions as well as the heat transfer from the crystal and the encapsulated melt, when the pressure inside the furnace is moderate or high. These studies conclude that the flow and thermal interaction between the gas and the melt flows must be taken into account if the pressure inside the furnace is not very low. This is certainly true in the case of LEC growth of indium phosphide crystals since the growth pressure must be above 27 atm. to maintain chemical equilibrium at the melting point of InP. Indeed, the gas flow is also important in the case of LEC growth of gallium arsenide crystals since these crystals are also grown at a moderately high pressure, above 100 psi. Evidently, the stress model for high-pressure growth must account for the buoyancy-induced gas flows inside the furnace. Also, since the simulation of convective flows is computationally intensive and time-consuming, an efficient and less-expensive method needs to be devised to calculate stresses once the flow and temperature fields have already been predicted using an appropriate numerical scheme.

The purpose of this paper is to report a novel scheme of coupling a finite volume code for flow simulation with a finite element package for stress prediction and perform preliminary calculations for stresses in a high-pressure, LEC-grown crystal. We use a high-resolution multizone adaptive scheme for transport and phase-change processes (*MASTRAPP*) to simulate convective flows in the melt and the gas, and temperature distributions in the entire system (consisting of melt, encapsulant, crystal, and gas); and a commercial FEM software (*ALGOR*) [12] to calculate the stresses. The *MASTRAPP* algorithm employs a multizone

adaptive-grid generation (MAGG) for discretization of the physical domains of arbitrary shapes and a curvilinear finite-volume formulation for discretization of the governing partial differential equations. A crystal-growth model based on this scheme has been recently developed by Zhang and Prasad [10,11]. The numerical results indicate that the effects of gas flow on the shape of the melt/crystal interface and stresses in the crystal are significant and cannot be ignored.

2 Model Description and Numerical Scheme

The present model assumes that the growth process is quasi-steady and axisymmetric; the gas and melt flows are laminar; the Boussinesq approximation is applicable; the thermo-physical properties are constant except those of the inert gas and the density variation in the body-force term; radiation is grey and diffusive and occurs with isothermal surroundings; the crucible walls are maintained at a constant temperatures T_h ; the radius of the crystal remains unchanged by adjusting the pull rate; the encapsulant/inert gas interface is flat; and the thermocapillary effects due to interfacial tension gradients in the melt/encapsulant and encapsulant/inert gas are negligible.

With the above assumptions, the general dimensionless form of the transport equations can be written as follows:

Conservation equations for mass, momentum and energy :

$$\nabla \cdot \mathbf{V} = 0 \quad (1)$$

$$\frac{\partial \mathbf{V}}{\partial t} + \mathbf{V} \cdot \nabla \mathbf{V} = -\nabla p - \nabla \cdot \boldsymbol{\tau} + Gr \, \theta \, \mathbf{e}_z \quad (2)$$

where, $\boldsymbol{\tau} = -(\nabla \mathbf{V} + (\nabla \mathbf{V})^T)$

$$\frac{\partial \theta}{\partial t} + \mathbf{V} \cdot \nabla \theta = \frac{1}{Pr} \nabla^2 \theta \quad (3)$$

and, for the solid crystal, $\mathbf{V} = \mathbf{V}_s$. Here \mathbf{V} , \mathbf{V}_s , θ , p , and $\boldsymbol{\tau}$ are the dimensionless velocity vector, crystal-pulling velocity, temperature, pressure, and shear stress, respectively. In

equations (1)-(3), Gr, Pr are the Grashof and Prandtl numbers, respectively; the Grashof number of the gas is defined as $g\beta_g b^3(T_h - T_f)/\nu_g^2$ and the Grashof number of the melt is defined as $g\beta_l b^3(T_f - T_t)/\nu_l^2$. Here b represents the radius of the crucible; T_h , T_f , and T_t represent the temperatures of the crucible, interface, and cold top wall, respectively; \mathbf{e}_z is a unit vector in the axial direction.

The boundary and interface conditions for transport simulation are discussed in detail in [14] for low-pressure growth and in [10,11] for high-pressure cases. For the high pressure calculations presented in this paper, a linearly varying temperature beyond crucible to the top, has been assumed. For stress calculations, the crystal surface is considered to be traction-free.

In the crystal-growth simulation, the positions of the melt/crystal interface and the free surfaces are neither known, *a priori*, nor planar, and hence, iterations must be performed for both the field variables and the shapes and positions of the melt/crystal interface and free surfaces. Therefore, considerable computational resources are required to simulate this process. The numerical difficulty becomes much more severe when a high-pressure growth is considered and the gas is allowed to interact with the melt flow. Also, most of the CPU time is spent on the transport simulations rather than the stress calculation which can be performed independently.

The finite-element method has been very successful for complex geometry problems. In the simulation of the CZ growth, global models invariably use FEM, and it has an additional benefit of being well suited for the stress calculations. However, the conventional FEM requires much larger computer resources, e.g., large-memory requirements and much more CPU time especially for the flow calculations. Also, the development time required for a FEM code is usually long.

Here, we use a high-resolution two-dimensional computer code, *MASTRAPP2d*, for transport calculations [10,11]; which employs a multizone adaptive-grid generation technique (MAGG) for discretization of the physical domains of arbitrary shapes and curvilinear b

nite volume (CFV) for the discretization of the governing equations. The MAGG algorithm generates a mesh that moves adaptively as the solution progresses and conforms to the change in the domain and internal interface shapes dynamically. This adaptive technique is able to handle irregular boundaries and provide accurate front tracking. It also preserves conventional advantages of the finite-volume method, i.e., straightforward physical interpretation, moderate requirements on computer resources, and is easy to develop and expand. The primary shortcoming of this approach is that it does not provide the same benefits as a finite-element code when a coupled flow and stress problem is encountered. This difficulty can be easily overcome by coupling a finite-element stress solver with *MASTRAPP*. The combination is meaningful and convenient since we use curvilinear coordinates for the finite-volume discretization. By carefully selecting the element model for stress calculations, the temperature interpolation can be avoided, and an efficient coupling can be successfully achieved. In *MASTRAPP2d*, the values of temperature as well as other variables are stored at the center of the control volume. Also, the data on grid locations and their sizes are already available from the MAGG module. Hence, we can select a four-node quadrilateral element and place the corner nodes on the four central points of the four connected control volumes. The use of such elements eliminates the extra effort needed to generate finite-element grids, and only the input data from *MASTRAPP2d* is required.

After the melt/crystal interface profile and temperature distribution in the crystal are obtained from *MASTRAPP2d*, we couple the finite-element code, *ALGOR* as a post processor to predict the thermal elastic stress in the crystal. For stress calculations, we assume that the material is linear elastic and isotropic; the crystal is stress free under uniform temperature; the material properties are constant; and the gas pressure on crystal side is the same as the melt pressure at the melt/crystal interface and remains unchanged. Also, any fluctuations in the pressure due to flow oscillations are considered to be small and are neglected.

Finally, the plastic deformation threshold in an isotropic material is evaluated from the von Mises stress using the theory of plastic deformation

$$\sigma_{VM} = \frac{1}{2}[(\sigma_1 - \sigma_2)^2 + (\sigma_2 - \sigma_3)^2 + (\sigma_3 - \sigma_1)^2]^{\frac{1}{2}} \quad (4)$$

where σ_{VM} is the von Mises stress and $\sigma_1, \sigma_2, \sigma_3$ are the principle stresses.

Further details on the mathematical model for low- and high-pressure crystal growth, grid generation, numerical methodology, and coupling with a FEM package can be found in Zhang and Prasad [10,11] and Zou et al. [14].

3 Results and Discussion

Two sets of results are presented here. The first case we have considered is Si growth where the effect of gas flow is assumed to be negligible because of the low pressure. Figure 1 presents the stream function, temperature, and stress distributions for Grashof number, $Gr_l = 10^7$, and shows that the melt/crystal interface is doubly-curved. The flow in the melt is, however, unicellular (in the half of the crucible). As shown in figure 2a, the shape of the melt/crystal interface changes significantly with Grashof number. As the convective flow in the melt becomes stronger, the melt/crystal interface changes from almost flat (for conduction) to a doubly-curved profile. This typical interface shape is well supported by the experimental data of Koai et al. [13] and other investigators, but has been predicted only by few models that incorporate convective flows in the melt. The conduction-radiation model assumes that the effect of melt convection is to simply increase the transport of heat from crucible to the melt since the Prandtl number for Si is very small. However, our simulations indicate that this enhancement in heat transfer is not uniform along the interface, and it may change the interface profile not just in the axial direction but also in the radial direction because of the complex flow structure in the vicinity of the interface.

The predicted stress distributions for the corresponding three cases, $Gr_l = 0, 10^6$, and 10^7 , look similar (not shown here). However, large differences in stress magnitude are predicted for different convection conditions. In figure 2b, the von Mises stress at the interface shows more

than 50% variation at some points (Fig. 2b). Since the melt/crystal interface happens to be an isotherm, a change in the interface profile implies variations in temperature gradients in the interface region. Hence, small changes in the interface shape can cause large variations in the stresses. Figure 2b also shows that the location of maximum and minimum stresses shift with the Grashof number. It is evident that for accurate prediction of stresses, especially near the interface region, which is considered to be the important transition area for dislocation formation, melt convection must be included in the model even at low Prandtl numbers. Also, the numerical scheme must be able to resolve the smallest variations in the interface profile.

Although a direct comparison of the results presented in figures 1 and 2 is not possible, they are in good qualitative agreement with the stress pattern and magnitude predicted by Kinney [8]. The difference between our results and those obtained by Kinney can be attributed to the variation in boundary conditions and geometry. Hwang et al. [15] have used an analytical method to investigate the effect of interface shape on the stresses in the crystal, and have reported that more than 50% variation may occur if the interface is not planar.

In the case of high-pressure growth, our preliminary simulations show that the effect of gas convection on temperature and stress fields in the growing crystal is significant. The velocity vectors, temperature and stress distributions for a simplified high pressure growth simulation with a 5-inch-diameter crucible and 1.667-inch-diameter crystal are presented in figures 3 and 4 for two different gas-flow conditions, $Gr_g = 10^7$ and 10^8 . For the cases presented here, the other governing parameters are: $Gr_l = 10^6$, $Re_c = 10^2$, and $Re_s = -10^2$, where $Re_c = \omega_c b^2 / \nu_l^2$, $Re_s = \omega_s b^2 / \nu_l^2$, and ω_c and ω_s refer to the rotation rates of the crucible and crystal, respectively, and are the same.

An increase in the Grashof number for the gas from 10^7 to 10^8 changes the gas flow pattern substantially. At $Gr = 10^7$, three recirculating cells are predicted in the gas region and the flow is moderate. Out of these three cells, one is located directly between the crucible

wall and the crystal, and the other two are tall, slender cells between the seed rod and the outer boundary. When the gas Grashof number is increased to 10^8 , only two recirculating cells are found and the flow field is much more stronger. The two slender cells have merged together to form one convective roll. In figures 3 and 4, the roll between the crucible wall and the crystal is very strong and has a strong impact on the heat loss or gain from the crystal. Since the crucible wall is heated, this cell brings energy from the crucible wall and dissipates it in the upper portion of the crystal surface - thereby heating the upper part of the crystal. On the other hand, as it moves down it encounters a higher temperature at the crystal surface (see isotherms in figures 3 and 4 and hence, gains energy in the lower portion. This behavior agrees well with the observation of Volkl and Muller [16], who measured temperature at different locations in a HPCG system. Cooling of crystal above the encapsulant layer causes a strong temperature decrease in the crystal and produces large stresses in this region. Evidently, this complex behavior of heating and cooling complicates the stress phenomena in the crystal.

Previous models using average heat-transfer coefficient have assumed that the effect of gas flow on the crystal surface is to produce a cooling effect. Obviously, our simulation does not support this assumption and suggests that both heating and cooling may be produced in different regions of the crystal surface. Although the location and strength of the bottom cell in the gas region may differ with the governing parameters and the crucible height beyond the melt level, the effect of this "roll" will remain the same and needs to be investigated in much more detail.

From figures 3 and 4, it is evident that the gas flow modifies the temperature distribution in the crystal and, therefore, the stress distribution in the crystal. It can also be seen that the change in gas flow significantly affects the melt/crystal interface profile. This influence is indirect and can be attributed to the flow and heat-transfer interaction at the encapsulant/gas and crystal/gas interfaces. The change of the stress pattern in high-pressure case is much more obvious than that in the low-pressure growth. Large stresses appear in

a region close to the boron oxide/gas. The maximum stress in this region changes from 15.05 MPa to 23.4 MPa with an increase in the gas flow strength. This agrees qualitatively with the results of Volkl and Muller [16] but differs in magnitude since the temperature distribution and interface profile are not the same. It is, however, evident that the gas flow significantly influences the stress distribution both in magnitude and pattern and must be incorporated in the HPCG model.

4 Concluding Remarks

Following are some conclusions that can be easily drawn from the present results:

- The computer model, *MASTRAPP2d* is capable of predicting complex shapes of the melt/crystal interface profile and resolving the steep gradients of field variables in its vicinity for both low- and high-pressure growth.
- A coupled finite-volume/finite-element computer model can be successfully used for simultaneous calculations of flow, temperature, and stress fields.
- Convective flows in both the melt and the gas influence the interface shape, temperature field, and stress distribution significantly, and must be accounted for by the crystal growth model.
- The gas flow has a strong influence on heating and cooling of the crystal and thereby produces complex temperature and stress fields in the high-pressure-grown crystal.

The simulations reported here are only preliminary. However, this study serves the purpose of demonstrating the influence of the melt and gas flows on stress field, and hence the crystal quality. Further simulation is under progress to study the high-pressure-growth phenomena in more detail.

Acknowledgments

Acknowledgments are due to the NSF Division of Design, Manufacturing and Industrial Innovation and AFSOR Program in Computational Mathematics for the support of this research.

References

- [1] A. S. Jordan, R. Caruso, and A. R. Von Neida, *Bell System Tech. J.* 59 (1980) 593.
- [2] S. Motakef and A. F. Witt, *J. Crystal Growth* 80 (1987) 37.
- [3] K. W. Kelly, K. Koai, and S. Motakef, *J. Crystal Growth* 113 (1991) 254.
- [4] F. Dupret, P. Nécodème, Y. Ryckmans, P. Wouters, and M. J. Crochet, *Int. J. Heat Mass Transfer* 33, (1990) 1849.
- [5] B. E. Bornside, T. A. Kinney, and R. A. Brown, *J. Crystal Growth* 108 (1991) 779.
- [6] N. Imaishi, T. Tsukada, M. Hozawa, Y. Okano, and A. Hirata, *Heat and Mass Transfer in Material Processing*, eds., I. Tanasawa, and N. Lior, Hemisphere Publishing (1992) 123.
- [7] T. A. Kinney, D. E. Bornside, and R. A. Brown, *J. Crystal Growth* 126 (1993) 413.
- [8] T. A. Kinney and R. A. Brown, *J. Crystal Growth* 132 (1993) 551.
- [9] V. Prasad, D. F. Bliss, and J. A. Adamski, *J. Crystal Growth* 142 (1994) 21.
- [10] H. Zhang and V. Prasad, *J. Crystal Growth* (1995) (in press).
- [11] H. Zhang and V. Prasad, *Proc., ASME/JSME Thermal Engineering Joint Conference*, Vol. 1 (1995), 559, ASME.
- [12] *Algor Manual* (Version 1994), Algor, Inc. Pittsburgh.

- [13] K. Koai, 1990, Doctoral Dissertation, MIT.
- [14] Y. F. Zou, H. Zhang, and V. Prasad, Transport Phenomena in Materials Processing and Manufacturing, eds. R. L. Mahajan et al., HTD Vol.-, (1995)ASME.
- [15] C. C. Hwang, C. S. Wu, and Y. J. Hsien, J. Crystal Growth 132 (1993) 523.
- [16] J. Volkl and G. Muller, Proc. E-MAS Meeting, Strasbourg, 1987, eds. Y. I. Nissim and P. A. Glasow, Editions de Physique, Les Ulis (1987) 141.

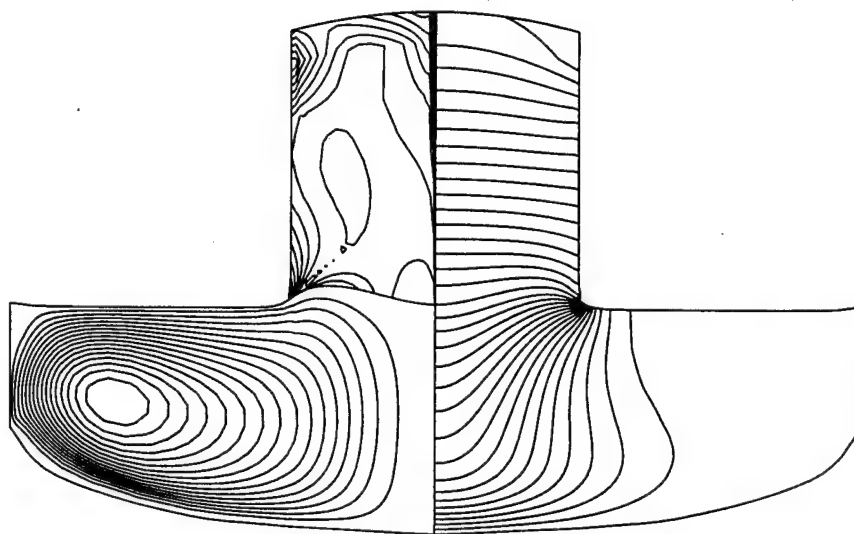
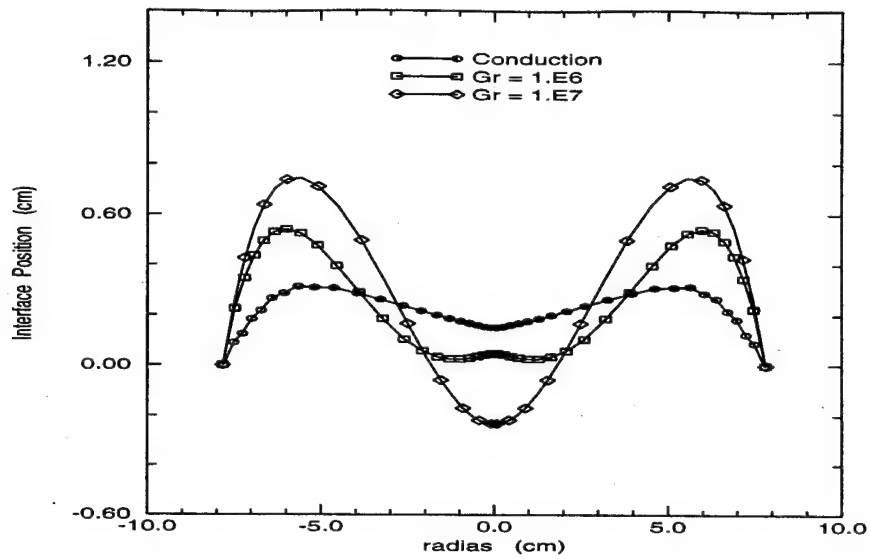
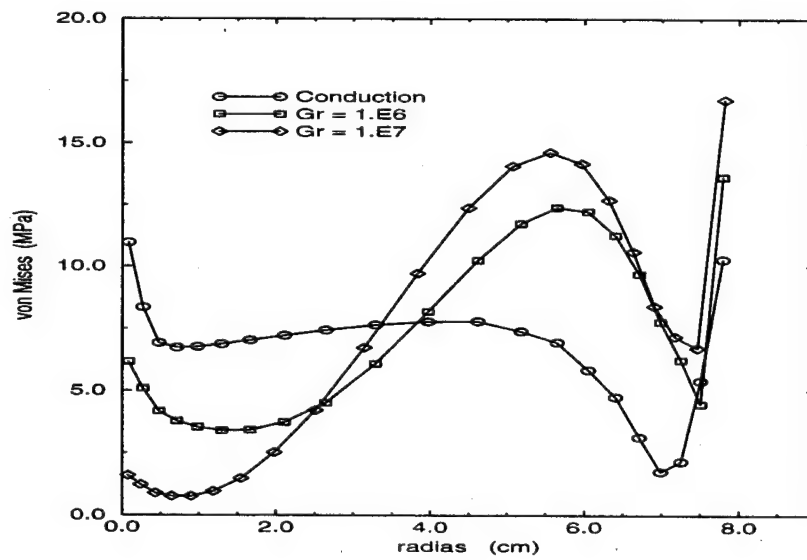


Figure 1: Distributions of the stream function, temperature, and stress for the low-pressure growth of Si crystal at the melt Grashof number, $Gr_l = 10^7$.



(a)



(b)

Figure 2: (a) Effect of melt convection on melt/crystal interface shape (Si growth) at $Gr_l = 0, 10^6$ and 10^7 , (b) Effect of melt convection on thermal stresses at the interface (Si growth) for $Gr_l = 0, 10^6$ and 10^7 .

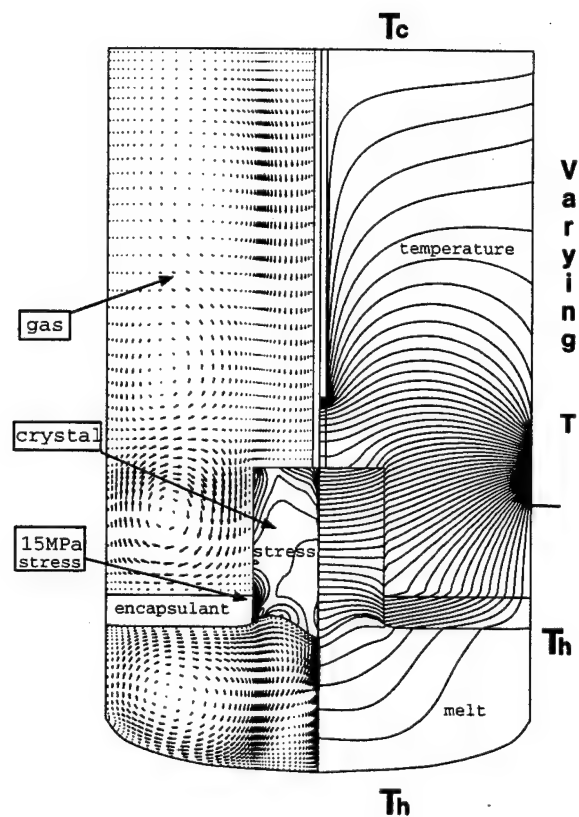


Figure 3: Distributions of temperature, stress, and velocity vectors for high-pressure growth at gas Grashof number, $Gr_g = 10^7$ and $Re_s = -10^2$, $Re_c = 10^2$ and $Gr_l = 10^6$.

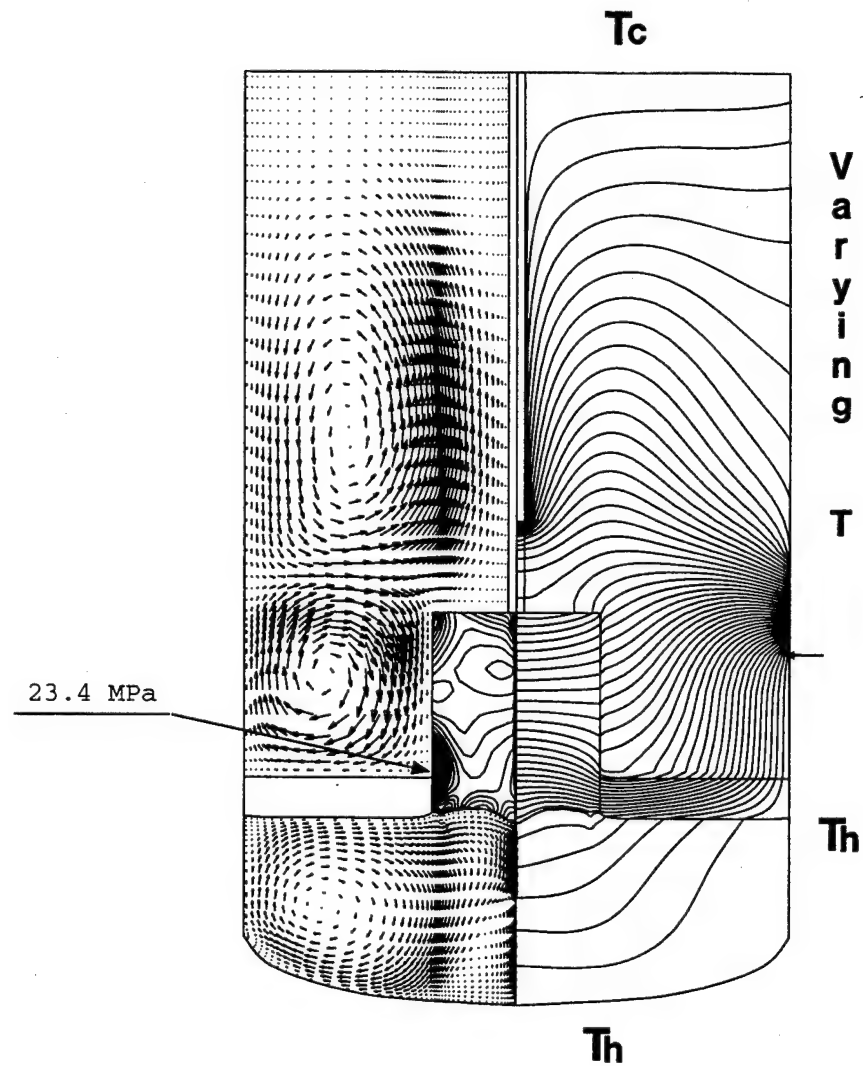


Figure 4: Distributions of temperature, stress, and velocity vectors for high-pressure growth at gas Grashof number, $Gr_g = 10^8$ and $Re_s = -10^2$, $Re_c = 10^2$ and $Gr_l = 10^6$.

APPENDIX E

TRANSPORT PHENOMENA OF CZOCHRALSKI CRYSTAL GROWTH AT LOW AND HIGH PRESSURES

H. Zhang and V. Prasad

Process Modeling Laboratory

Department of Mechanical Engineering

State University of New York, Stony Brook, NY 11794

ABSTRACT

A high resolution numerical scheme based on multizone adaptive grid generation (MAGG) and curvilinear finite volume discretization is employed to study the transport phenomena in Czochralski (CZ) and liquid-encapsulated CZ (LEC) crystal growth processes. The model incorporates melt and gas flows induced by buoyancy and surface tension forces, and crystal and crucible rotations, as well as by radiation heat transfer. In the case of CZ growth of silicon (very low pressure), the melt flow is oscillatory, and the melt/crystal interface is convex. The flow and temperature fields in the melt, the temperature distribution in the crystal, and the shape of the melt/crystal interface change significantly if an inert gas is present in the furnace (LEC growth). It is demonstrated that an applied magnetic field suppresses melt flow oscillations for both CZ and LEC growth.

INTRODUCTION

High performance electronic and opto-electronic devices require large diameter crystals with a high degree of crystallographic perfection, uniform and low resistivity gradients, low defect density, optimum and consistent dopant distribution, and high level of electrical, optical and mechanical properties. The crystalline materials are also important for many other applications, e.g., light-wave communications, fiber optics, lasers, sensors, solar cells and micro-electromechanical systems. To meet new technological demands, improve the quality and size of the crystals, and reduce their costs, crystal growth technology is moving in new directions. For example, Czochralski (CZ) silicon technology is progressing towards 300 mm (from 150-200 mm) diameter crystals as well as a solid-feed continuous (CCZ) process for Si (Anselmo et al., 1993). The expanding commercial importance of compound semiconductors has led to the development of special pulling techniques for these materials, e.g., liquid encapsulated Czochralski (LEC) technique for bulk growth of III-V compounds. Salient features of LEC growth include its simplicity, and very little mechanical modifications to a standard crystal puller.

The development of high pressure LEC technique has revolutionized the production of GaP and InP making them commercially useful substrate materials. Since the synthesis to produce these compounds as solid ingots and use them to grow crystals in a separate chamber is expensive and prone to contamination, "one-step" process is preferable. Such processes are widely used for GaAs and are under development for InP and GaP (Hurle, 1983). For example, for one-step growth of InP crystals, the In melt is synthesized in a high pressure crystal growth (HPCG) furnace by injecting phosphorus vapor and then a crystal is grown from this InP melt by either LEC, magnetically-stabilized LEC or Kyropoulos (MLEK) technique. The vapor pressure required to maintain chemical equilibrium at the melting temperature (1063°C) of InP is 27.5 atm. Generally, a pressure of about 4 MPa is maintained for the InP growth. It should be noted that Si crystals are grown at very low pressure (negligible gas convection) and GaAs crystals are produced at a pressure of about 0.6 MPa. The presence of gas inside the furnace and an encapsulant layer over the melt in a LEC or LEK process changes the heat exchange pattern into the furnace and influences the interface and meniscus conditions significantly. The growth dynamics of LEC processes are therefore very different from that of the regular CZ growth. The recirculatory gas flow in such systems is oscillatory and turbulent (Prasad et al., 1994). The flow and heat transfer interaction between the recirculating gas, B_2O_3 surface and crystal is highly complex and affects the crystal quality significantly. It is therefore important to understand the mechanisms of energy transport in moderate and high pressure growth systems, which include all modes of heat transfer and varying flow regimes. However, very little has been reported on thermal characteristics of these systems (Prasad et al., 1994 ; Dupret, 1994).

Over the past two decades, numerical simulations of CZ and LEC growth have been performed with varying degrees of complexity. The simulations vary from bulk flow approximations that only simulate two-dimensional cavity flows to models which incorporate many of the crystal, melt and puller thermal characteristics and describe global heat transfer within the furnace (Langlois, 1981, Hurle, 1983; Muller, 1983; Brown, 1988; Dupret, 1994). More comprehensive models include the melt/crystal region, the radiative enclosures, and other components of the furnace. These methods are based on separate analysis of heat transfer within major component and employs continuity of temperature and heat flux at the interface to couple the calculations in various regions. The global models for CZ and LEC processes reported thus far consider radiation and conduction heat transfer in each element, and convective flow and heat transfer is considered only in the melt. In the case of high pressure crystal growth (HPCG), gas convection is extremely important since it can directly cool or heat the elements, as well as indirectly change the radiation heat transfer by changing the surface temperature.

Crystal growth is a complex process and the quality of crystal depends on many macro- and microscopic physical effects. Description of all of these physical phenomena and their incorporation into a mathematical model is not an easy task. One therefore has to make a judicious choice and consider all of the primary effects which can influence the growth process first. The transport model, however, must account for the flows induced by buoyancy and surface tension forces, crucible and crystal rotations, and crystal pulling. In the case of moderate and high pressure systems, convective flows in the gas and diffusion through the encapsulant layer also need to be included.

To simulate the transport phenomena of CZ and LEC crystal growth, we have developed a high resolution computer model that is based on multizone adaptive grid generation (MAGG) and curvilinear finite volume (CFV) discretization. In the area of multizone adaptive finite

volume algorithm we have constructed an efficient algorithm for clustering of grids in the interface regions as the solutions progress. This is particularly suitable for problems involving irregular domains and free as well as moving boundaries and interfaces. A unified set of two-dimensional governing equations in curvilinear coordinate systems has been derived for the entire multiphase crystal growth system and transformation relations for coefficients and equations for moving interfaces have been obtained. An efficient scheme based on finite volume flux discretization, non-staggered grids, power law for convective fluxes, and pressure correction has been implemented. $k-\epsilon$ equations have been employed to model the turbulent gas flows. The present formulation also incorporates a magnetohydrodynamic (MHD) model suitable for liquid metals. The motivation to include magnetic effects comes from the fact that they are known to suppress flow and temperature oscillations and are being used in many industrial and laboratory processes. This paper reports preliminary results to demonstrate the suitability of this process model and the effects of gas convection in a HPCG system as well as the effect of magnetic fields on flow oscillations.

FORMULATION AND NUMERICAL SCHEME

A schematic of the high pressure crystal growth (HPCG) system under consideration is shown in Fig. 1. It is assumed that the system is axisymmetric; the thermophysical properties of crystal, melt and encapsulant are constant; the properties of the inert gas are only temperature dependent; the crystal, melt and encapsulant surfaces are grey and each of them exchange radiation only with the HPCG walls which are treated as isothermal black surfaces; the crucible side wall and bottom are isothermally heated; and a desired crystal diameter can be maintained by adjusting the pull rate. Based on Grashof number estimates by Prasad et al. (1994), the melt flow is considered to be laminar while the gas flow is turbulent and is modeled by $k-\epsilon$ formulation (Launder, 1978; Ristorcelli and Lumley, 1992). With these assumptions, the growth process is governed by conservation equations for mass, momentum, and energy in the melt, the encapsulant (B_2O_3), the inert gas, and energy equation in the solid, which can be written in a general form as

$$\begin{aligned} & \frac{\partial}{\partial t}(r\gamma\phi) + \frac{\partial}{\partial x}(r\gamma u\phi) + \frac{\partial}{\partial r}(r\gamma v\phi) \\ &= \frac{\partial}{\partial x}(r\Gamma\frac{\partial\phi}{\partial x}) + \frac{\partial}{\partial r}(r\Gamma\frac{\partial\phi}{\partial r}) + rS \end{aligned} \quad (1)$$

where ϕ is the generalized variable (Table 1), S is the volumetric source, Γ is the diffusion coefficient and γ is the density ratio. Equation (1) is used for the entire multicomponent, multiphase system, with the provision to account for local properties, and abrupt changes in transport properties across the zone boundaries as well as their possible movement.

The following scales have been used to non-dimensionalize the governing equations: length: b , velocity: ν_m/b , pressure: $\rho_m\nu_m^2/b^2$, time: b^2/ν_m , density: ρ_m , dynamic viscosity: μ_m , conductivity: k_m , specific heat: C_{pm} , heat source: $k_m(T_h - T_f)Pr_m/b^2$, and temperature: $\theta = (T - T_f)/(T_h - T_f)$.

In energy equation, the radiation heat flux is given by:

$$q'' = \epsilon\sigma_r(T^4 - T_\infty^4)b/kPr_m(T_h - T_f) = Bi_r(\theta - \theta_\infty) \quad (2)$$

In the above equations, the governing parameters are Gr_i , Pr_i , γ_i , ζ_i , Rc_i , where i represents the phase/zone of the system (Table 2).

Table 1: Variables for the generalized governing equation

Eqs	Variable	Diffusivity	Source
	γ	0	0
u^+	γu	μ'_{eff}	$-\partial p/\partial z + Gr\beta\rho\Theta$ $+ S_{turb} + S_{mag}$
v^+	γv	μ'_{eff}	$-\partial p/\partial r - v/r^2$ $+ w^2/r + S_{turb}$ $+ S_{mag}$
rw^+	γrw	μ'_{eff}	$-(2/r) \partial(rw)/\partial r$ $+ S_{turb} + S_{mag}$
θ	$\gamma C'_p \theta$	$\mu'_{eff} C'_p / Pr$	$-\nabla \cdot \mathbf{q}'' + S_{turb}$
k	γk	μ'_{eff}/σ_k	$G - \gamma\epsilon$
ϵ	$\gamma \epsilon$	$\mu'_{eff}/\sigma_\epsilon$	$C_1 G\epsilon/k - C_2 \gamma \epsilon^2/k$
ϕ_e	$\phi_e(\gamma = 0)$	σ_e	$-\nabla \cdot (\sigma_e \mathbf{u} \times \mathbf{B})$

⁺ The terms, S_{turb} and S_{mag} , refer to the source terms from turbulence, magnetic forces, and μ'_{eff} is the effective dimensionless viscosity.

To examine the effect of magnetic field on flow oscillations, the model incorporates the MHD equations. The general study of magnetohydrodynamics begins with the Maxwell's equations and Ohm's law for a medium in motion. The theory of hydromagnetic crystal growth flow is greatly simplified by the liquid metal approximations. First, the induced magnetic field, which is much weaker than the applied magnetic field, can be neglected. Second, if the applied field is steady, the electric field is irrotational and hence can be driven by a potential ϕ_e . An equation for ϕ_e when the magnetic field is applied in the vertical direction has been listed in Table 1 (Hjellming and Walker, 1987; Sabhapathy and Salcudean, 1990) where σ_e is the electrical conductivity.

The boundary conditions include no-slip on the solid boundaries and a shear stress balance at the free surface. Wall function corrections have been employed for turbulence equation and an insulation condition has been used for the electric current (electric current in the crystal has been negative in this study) (Launder, 1978; Hjellming and Walker, 1987; Zhang and Prasad, 1995a, 1995b). Important operating parameters used for present simulations are shown in Table 2.

The governing equations for melt and crystal phases are solved iteratively and independently by invoking the quasi-steady assumption (within one time interval) for the crystal/melt interface. Underrelaxation is employed while iterating for the free surface movement. With the interface fixed at any time step, the fusion temperature at the interface is forced as

Table 2: Governing parameters for present simulations.

Parameter	Definition	Si	HPCG
Density	$\gamma_s = \rho_s / \rho_m$	1.0	1.0
Conductivity	$\kappa_s = k_s / k_m$	0.4	0.4
Specific heat	$Rc_s = C_{ps} / C_{pm}$	0.96	1.0
Aspect ratio	$Ar_m = h_m / b$	0.375	0.68
Radius ratio	$Rr_s = a / b$	0.5	0.5
Melt Grashof	$Gr_m = \frac{g\beta_m b^3 (T_h - T_l)}{\nu_m^2}$	10^8	10^7
Gas Grashof	$Gr_g = \frac{g\beta_g b^3 (T_h - T_l)}{\nu_g^2}$	0	10^8
Reynolds No. for Crucible	$Re_c = \omega_c b^2 / \nu_m$	0	-500
for Crystal	$Re_s = \omega_s b^2 / \nu_m$	0	500
Prandtl No.	$Pr_m = \nu_m / \alpha_m$	0.015	0.068
			0.015
Hartmann No.	$Ha = Bb(\sigma / \rho\nu)^{1/2}$	200	200
Biot No.	$Bi_r = \epsilon_{eff} \sigma_r b / k_m \times$ $(T_m^2 + T_\infty^2)(T_m + T_\infty)$	ϵ_{eff} 0.25	ϵ_{eff} 0.25
Froude No.	$Fr_m = \nu_m^2 / gb^3$	10^{-9}	10^{-9}
Bond No.	$Bo_m = \rho_m gb^2 / \sigma_m$	1000	1000
Contact angles	ϕ_{sl}	45°	45°

the boundary condition for both phases. When the solutions for two phases have converged to the desired accuracy, an interface energy balance is employed to evaluate the new position of the solidification front. A detailed discussions on boundary and interface conditions can be found in Zhang and Prasad (1995a, 1995b).

A high resolution two-dimensional computer code, MASTRAPP2d, suitable for transport and phase-change processes involving time-varying domains and irregular boundaries is used for present simulations (Zhang and Prasad, 1995a). The numerical scheme employs (a) a multizone adaptive grid generation technique (MAGG) for the discretization of physical domains of arbitrary shape, and (b) the curvilinear finite-volume (CFV) approach for the discretization of the governing partial differential equations and development of the finite difference equations (Zhang and Prasad, 1995c). The MAGG scheme is based on constrained adaptive optimization of grid characteristics. One of the major advantages of this scheme is that it preserves internal interfaces separating various zones and always makes them coincide with some grid lines. The scheme allows grids to move adaptively as the solutions progress and/or domains (or subdomains) change. The generated grids are always smooth and orthogonal and cluster in the interface and free surface regions. The CFV approach is based on flux discretization in the physical domain which makes the change of domain boundaries in the process model easy and less costly. More accurate solutions can be obtained for a large range of grid orthogonality. Combined use of these two techniques together with non-staggered grids, power law for convective fluxes, and pressure correction has resulted in an efficient scheme. A detailed description of the numerical scheme and its suitability for both

low and high pressure crystal growth processes can be found in Zhang and Prasad (1995a).

The computer model has been validated and tested against the numerical results of Anselmo et al. (1993) and an excellent agreement (within 5 % difference in velocity and temperature fields) has been achieved for 2D melt flows in a crucible with curved bottom. The code has also been tested for solidification in open and closed cavities when cooling takes place on cavity wall(s). The predicted results agree well with the experiments (Zhang, 1995d). Simulations for CZ and LEC growth were performed on SUN workstations. 42×42 nodes were used for low pressure growth which required about 48 hours of CPU time for steady and periodic oscillatory solutions. Approximately 72 hours were required to attain convergence for high pressure growth, with 62×42 nodes.

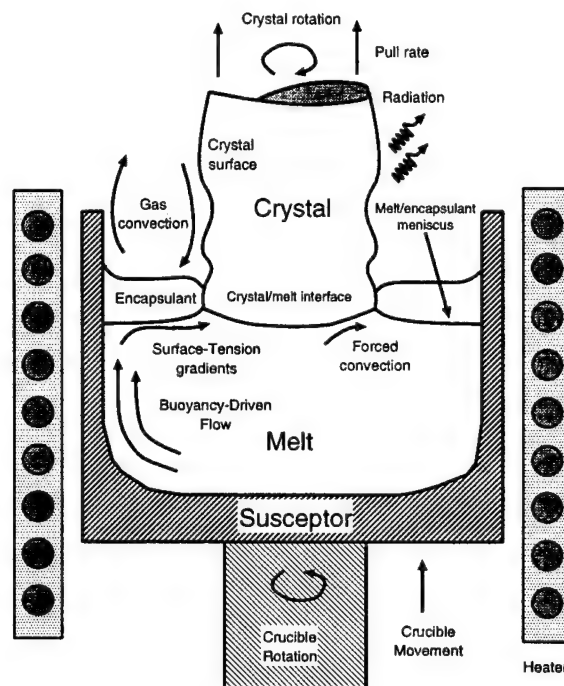


Figure 1: A schematic of the driving forces and transfer mechanisms in a LEC growth.

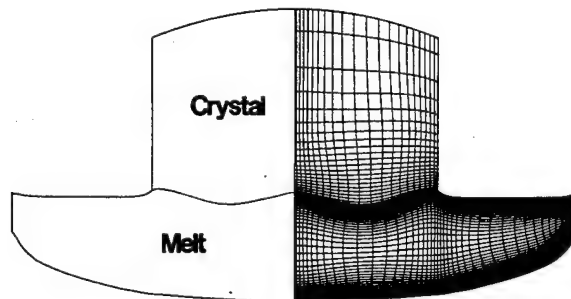


Figure 2: Grid distribution for CZ growth in physical domain.

RESULTS AND DISCUSSIONS

A schematic of driving forces and transport mechanisms in LEC growth of GaAs and InP crystals is presented in Fig. 1. The layer of encapsulant is not used in the case of Si growth. Also, since Si is grown at a very low pressure the gas convection can be neglected, radiation playing a dominant role in heat dissipation from the melt surface. However, in the case of GaAs and InP growth, both convection and radiation are considered to be important. The temperature distribution and local heat flux on surfaces of both the crystal and the encapsulant layer are controlled by turbulent convection and radiation heat transfer, which directly affects the crystal quality and the crystal/melt interface shape. Four types of driving forces are considered in the melt - buoyancy, rotation of crystal, rotation of crucible, and surface tension due to temperature gradient at the surface of the melt. Since the encapsulant layer is highly viscous and transparent, it allows radiation and conduction but has no velocities. The crucible is held by a graphite susceptor, heated by either a resistance heater or a RF coil(s), and hence, the temperature boundary condition on crucible wall is generally complicated.

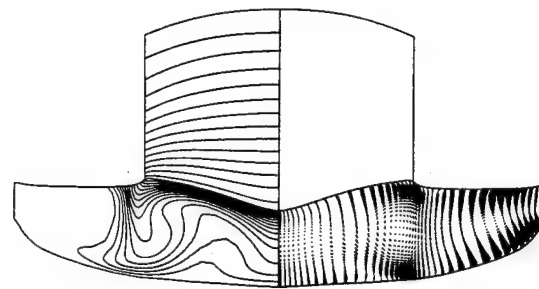
The grid distribution considered for CZ simulation of Si growth is shown in Fig. 2. Only crystal and melt are included in the computational domain. A structured grid is used and grid lines are smooth and continuous everywhere. The grids are orthogonal and always cluster near the interface, the free surface and the solid boundary. After the crystal/melt interface is determined, the grid points can only move along the interface:

Figure 3(a) presents the velocity and temperature fields for CZ growth at Grashof number, $Gr_m = 10^8$, when the crystal and crucible are not rotated, ($Re_c = Re_s = 0$) and the crucible bottom and side walls are isothermally heated. The free surface of the melt is assumed to be insulated (no radiation loss). In reality, the melt flow is a three-dimensional phenomena when $Gr_m = 10^8$. However, the axisymmetric assumption is still widely used in the literature for calculation in the melt. Further, the laminar flow assumption may not be valid in reality (Hurle and Cockayne, 1994).

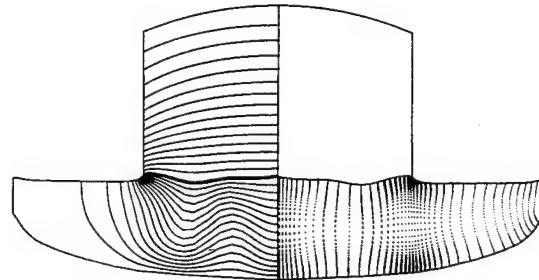
The temperature distribution in this case is very complex and there exists three recirculating cells in the half of the crucible. The temperature gradient in the vicinity of the interface and crystal/melt meniscus is very steep. Although not shown here, both the flow and temperature fields oscillate in this case (see heat flux plot in Fig. 3d). This is consistent with the behavior reported by previous investigators (Anselmo et al., 1993). As can be expected, the melt/crystal interface oscillates although the interface remains concave. Figure 3(a) also demonstrates the special capability of the numerical scheme to resolve complex shapes of the interface, meniscus and free surface.

The effect of an applied magnetic field ($Ha = 200$) on streamline patterns and temperature distribution for the case considered in Fig. 3(a) is presented in Fig. 3(b). Interestingly, the temperature field has changed drastically and shows much less skewness. Indeed, this temperature field is much closer to the conduction profile. Although three convective rolls are still present in the melt, their strengths are much weakened. The most desirable effect from crystal growth considerations is the flatness of the interface shape achieved with the use of a magnetic field. It has also reduced the steepness of the temperature gradient in the interface and meniscus region. Figure 3(d) shows that the melt flow and temperature are still oscillatory. However, the amplitude of oscillations is very small, and growth conditions are much better than that in Fig. 3(a).

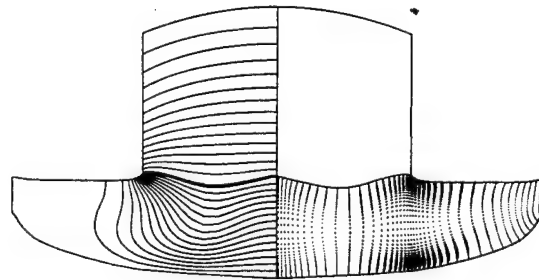
To further examine the strength of melt convection, we have also performed computations for $Gr_m = 10^7$, all other parameters remaining the same ($Ha = 0$) as in Fig. 3(a). One



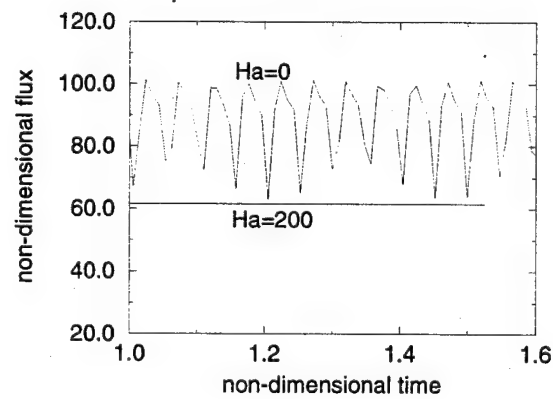
(a)



(b)

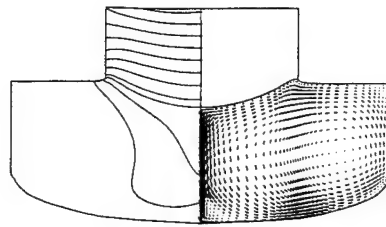


(c)

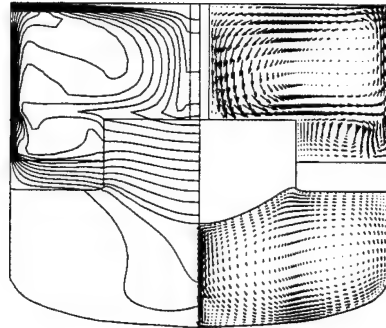


(d)

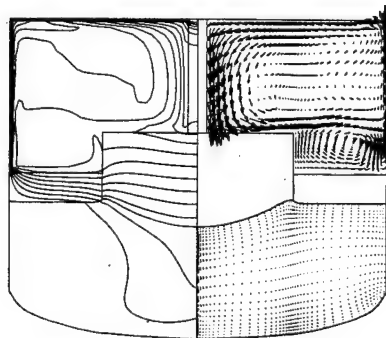
Figure 3: Flow field and temperature distributions for (a) $Gr_m = 10^8$, $Ha = 0$, (b) $Gr_m = 10^8$, $Ha = 200$ and (c) $Gr_m = 10^7$, $Ha = 0$ (d) Oscillations of heat flux for the system with and without a magnetic field for $Gr_m = 10^8$ (Figs. 3a and 3b).



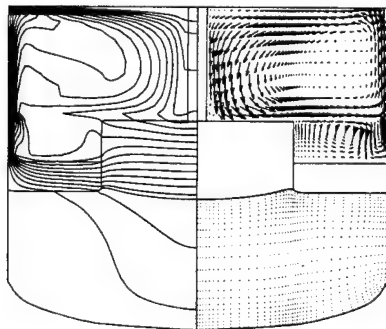
(a)



(b)



(c)



(d)

Figure 4: Flow and temperature fields for the melt and crystal for the growth of (a) Si, (b) GaAs, (c) InP and (d) GaAs with an applied magnetic field ($Ha = 200$).

can now very easily see the resemblance between Fig. 3(c) and 3(b). It is evident that the magnetic field reduces the strength of buoyancy induced convection by reducing the strength of the body force term in the momentum equation.

Next, computations are performed to compare the LEC growth of GaAs and InP with the CZ growth of Si. To consider the effect of gas convection computations are performed for three cases - no gas convection, moderate pressure gas and high pressure gas. Note that the pressure inside the HPCG furnace is much lower in the case of GaAs growth than for the InP growth and hence, the gas flow is expected to be weaker for GaAs growth. In all of these cases, the melt height, the crystal size and the thickness of the encapsulant layer are kept constant. The parameters used for these simulations are: $Gr_m = 10^7$, $Pr_m = 0.015$ and $Re_c = -Re_s = 500$. The walls of the crucible are considered to be isothermally heated. The radiative boundary conditions are imposed on both the top and the sidewall of the crystal. The upper end of the crystal is considered to be flat, a characteristics of the Kyropoulos growth, as opposed to a crown-shape for CZ Si growth.

Figure 4(a) presents the velocity and temperature distributions for Si growth conditions. There exist two recirculatory cells in the melt, one in the outer region and the other directly underneath the crystal. The crystal/melt interface is nonplanar and convex, and penetrates deep into the melt. This is only a representative solution for the CZ Si growth. In general, the flow under industrial growth conditions are much more complex and oscillates (Muller, 1988, Anselmo et al., 1993). The melt/crystal interface under those conditions is wavy (doubly-curved) and can also oscillate. The temperature gradients near the interface, meniscus and free surface are generally steep. However, the results in Fig. 4(a) presents a good case to examine the effect of gas convection.

The velocity and temperature fields at moderate pressure growth (GaAs) are presented in Fig. 4(b). The governing parameters are the same as that used for Si growth in Fig. 4(a), except that $Pr_m = 0.068$, and $Gr_g = 10^7$, $Pr_g = 0.7$ and $P_g = 1$ atm. The upper surface of the computational domain is considered to be cooled at a constant temperature and the side wall of the domain is assumed to be at a higher temperature. Since crucible sits inside a graphite susceptor whose height is generally larger than the crucible height, this assumption is not unrealistic for preliminary calculations. Note that the melt height in the crucible also decreases with the growth. As is evident from Fig. 4(b), convective flow in the gas is quite strong. The gas flows upward along the hot side wall and downward along the seed shaft. This produces a large recirculatory cell above the top of the crystal. The crystal and crucible rotations in opposite directions, on the other hand, result in two counter-rotating cells underneath the large cell and directly above the encapsulant layer. Temperature profiles on the upper surface of the crystal, the sidewall of the crystal, and the top surface of the encapsulant layer are therefore determined by both gas convection and radiation heat transfer. Although the gas pressure is only 1 atm., it is affecting the thermal characteristics of the furnace in a big way. Indeed, it may heat the crystal in its lower portion by bringing energy directly from the hot sidewall while it produces a cooling effect in the upper portion of the crystal. The flow pattern in the melt is similar to that observed in Fig. 4(a). The shape of the crystal/melt interface remains convex but the penetration of interface into the melt has increased due to gas cooling.

Figure 4(c) presents the results for high pressure gas flows, a condition required for the InP growth. The governing parameters are again the same except that the gas pressure is taken as 40 atm, and $Pr_m = 0.015$. The gas convection in this case is much stronger than that in Fig. 4(b). Although not directly evident from vector plots (due to graphics

limitations), the maximum velocity in Fig. 4(b) is about 10 times larger than that in Fig. 4(a). The melt flow pattern is nearly the same but the recirculatory flow in the gas has become more complex. Three cell structure is still preserved though the size and positions of the cells have changed. Also, three secondary cells have appeared within the the large recirculatory cell above the crystal. Figure 4(b) shows that under high pressure conditions, thin boundary layers can emerge resulting in strong flows near the gas boundaries. This produces much more uniform temperature in the core of the gas. The temperature gradient in the crystal is now weaker because of the heat gain from the crucible side wall (Fig. 4c) due to gas convection. Since the crystal is now hotter, the crystal/melt interface is less convex as compared to that in Fig. 4(b).

The melt flows in Figs. 4(b) and 4(c) are oscillatory (Fig. 5). Oscillations in the case of GaAs growth is much more stronger than that for the InP growth. The reason for large oscillations at moderate pressures and weak oscillations at a high pressure is not clear at this time. It may need a systematic study for a wide range of governing parameters to understand this phenomenon. Since these oscillations greatly affect the quality of the grown crystals, it is important that this behavior is thoroughly analyzed.

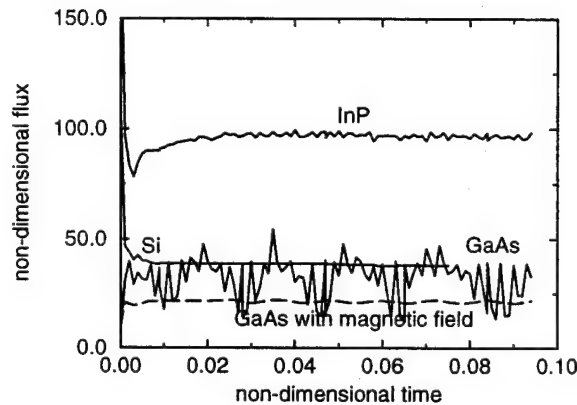


Figure 5: Oscillations in heat flux for Si, GaAs (with and without a magnetic field) and InP crystal growth.

Figure 5 demonstrates another important aspect of the high pressure growth that the heat loss in the case of InP growth is about 100% more than that for the Si and GaAs growth. The average heat transfer rates for Si and GaAs growth are observed to be almost equal although the Si melt is seen to be stable under the conditions of Fig. 4(a). This large scale change in overall heat transfer behavior and flow oscillations clearly indicate the importance of gas convection in the HPCG growth.

The effect of an applied magnetic field ($Ha = 200$) on velocity field and temperature distributions for the case considered in Fig. 4(b) is presented in Fig. 4(d). The temperature field has changed and shows less skewness. The flow in the melt is much weaker than that without a magnetic field. Convection in the gas remain unchanged. The magnetic field has reduced the steepness of temperature gradient in the interface and meniscus region and the interface is much less convex. Figure 5 shows that the melt flow and temperature are still oscillatory. However, the amplitude of oscillations is small, and growth conditions have been greatly improved by the application of this magnetic field.

CONCLUDING REMARKS

The simulations for Si, GaAs, and InP growth using the multizone adaptive process model (MASTRAPP2d) demonstrate (a) the effectiveness of the MAGG scheme to simulate multiphase systems with more than one material, and free and moving interfaces; and (b) the complexity of the flow structure and temperature field in a HPCG system that ultimately determine the crystal quality. The calculations presented here are only preliminary and they are not ready to be compared with the experimental data due to lack of information on boundary conditions and process variables. However, these results clearly indicate that the thermal conditions in a HPCG system is extremely complex. Both temperature distribution and melt/crystal interface shape are dramatically changed with the presence of the gas in the furnace and its pressure. An applied magnetic field is observed to suppress oscillations in the melt. It makes the velocity field weak and the temperature gradients in the interface region less steeper. As a result the shape of the melt/crystal interface greatly improved.

ACKNOWLEDGEMENTS

This research has been supported by the AFOSR program in computational mathematics. Acknowledgments are also due to D.F. Bliss of the US Air Force Rome Laboratory for encouraging this research on high pressure crystal growth, and to A. Anselmo for helpful discussions.

References

- [1] Anselmo, A., Prasad, V., Koziol, J. and Gupta, K.P., "Oscillatory Convection in Low Aspect ratio Czochralski Melts," *J. Crystal Growth*, **134**, 116-140, 1993.
- [2] Bliss, D.F., Hilton, R.M., Bachowski, S. and Adamski, J.A., *J. Electronic Materials*, **20**, 967-971, 1991.
- [3] Brown, R.A., "Theory of Transport Processes in Single Crystal Growth from the Melt," *AIChE Journal*, **43**, 881-911, 1988.
- [4] Dupret, F. and Bogaert, N. van den, Modeling Bridgman and Czochralski growth, in *Handbook of Crystal Growth*, Hurle, D.T.J., Ed., Vol. 2, pp. 875-1010, North-Holland, New York, 1994.
- [5] Hjellming, L.N. and Walker, J.S., Melt Motion in a Czochralski Crystal Puller with an Axial Magnetic Field: Isothermal Motion, *J. Fluid Mechanics*, **182**, 335-368, 1987.
- [6] Hurle, D.T.J., Convective Transport in Melt Growth Systems, *J. Crystal Growth*, **65**, 124-132, 1983.
- [7] Hurle, D.T.J. and Cockayne, B., Czochralski growth, in *Handbook of Crystal Growth*, Hurle, D.T.J., Ed., Vol. 2, pp. 99-212, North-Holland, New York, 1994.
- [8] Jordan, A.S., Estimated Thermal Diffusivity, Prandtl Number and Grashof Number of Molten GaAs, InP, and GaSb, *J. Crystal Growth*, **71**, 551-558, 1985.
- [9] Langlois, W. E., Convection in Czochralski Growth Melts, *PCH PhysicoChemical Hydrodynamics*, **2**, 245-261, 1981.
- [10] Launder, B.E., *Turbulence in Topics in Applied Physics*, Vol. 12, Springer-Verlag, Berlin, 1978.

- [11] Muller, G., Crystals, Vol. 12, Springer-Verlag, Berlin, 1988.
- [12] Prasad, V., Bliss, D.F. and Adamski, J.A., Thermal Characterization of the High Pressure Crystal Growth System for In-Situ Synthesis and Growth of InP Crystals, *J. Crystal Growth*, **142**, 21-30, 1994.
- [13] Ristorcelli, J.R. and Lumley, J.L., Instabilities, Transition and Turbulence in the Czochralski Crystal Melt, *J. Crystal Growth*, **116**, 447-460, 1992.
- [14] Sabhapathy P. and Salcudean, M.E., Numerical Study of Flow and Heat Transfer in LEC Growth of GaAs with an Axial Magnetic Field, *J. Crystal Growth*, **104**, 371-380, 1990.
- [15] Zhang, H. and Prasad, V., Multizone Adaptive Process Model for Czochralski Crystal Growth at Low and High Pressure, *J. Crystal Growth*, 1995 (in press).
- [16] Zhang, H., and Prasad, V., Multizone Adaptive Simulations for High Pressure Crystal Growth, ASME/JSME Thermal Engineering Joint Conference, Maui, Hawaii, pp. 559-568, 1995.
- [17] Zhang, H., and Moallemi, M.K., A Multizone Adaptive Grid Generation Technique for Simulation of Moving and Free Boundary Problems, *Numerical Heat Transfer, Part B*, **27**, 255-276, 1995.
- [18] Zhang, H., Moallemi, M.K., and Prasad, V., Application of MAGG - A Multizone Adaptive Generation technique - for Simulations of Moving and free Boundary problems, *Numerical Heat Transfer*, 1995 (submitted).

APPENDIX F

EXPERIMENTAL TECHNIQUES AND MEASUREMENT OF InP PROPERTIES

In order to successfully model the synthesis and growth of InP crystals, accurate values of the thermophysical properties of the solid and the melt are required. At the beginning of this project there were no reliable data for the density of liquid InP and no reported values for the thermal or electrical conductivities of the melt. In addition the vapor pressure over In melts containing varying amounts of P had been reported only for the range from about 43 to 50 atomic percent P.

Obtaining data for molten InP is complicated by the high vapor pressure of P that exists over a stoichiometric melt (about 30 atm) and by the tendency of the melt to supercool by as much as hundreds of degrees centigrade if it is entirely melted before freezing. If an open crucible is employed to contain a melt, the high vapor pressure requires encapsulation with an inert material such as B_2O_3 . This glassy material is very viscous even at the 1065°C melting point of InP and it also wets the silica crucibles that are generally used. The crucibles therefore break whenever they are returned to room temperature. Due to these problems and the high temperature, experiments to measure the thermophysical properties are cumbersome and intricate and in some cases they need to be repeated a number of times before reliable information can be obtained. In spite of these obstacles, the vapor pressure of P over $In_{1-x}P_x$ as a function of x has been determined at 1100°C and the thermal and electrical conductivities of molten InP measured. The change in density when InP melts has also been estimated.

Phosphorus Vapor Pressure over $In_{1-x}P_x$ Liquid at 1100°C

The phosphorus vapor pressure over $In_{1-x}P_x$ melts at 1100°C containing up to 50.5 atomic percent phosphorus has been measured. A diagram of the fused silica ampoule used for this purpose is shown in Fig. 1. As the P pressure inside the ampoule increases with respect to the argon pressure outside, the flat diaphragm flexes and the long arm moves a linear variable

differential transformer (LVDT) core and produces a voltage that varies nearly linearly with pressure. The balance condition is obtained by noting the LVDT voltage when the ampoule and pressure vessel are both evacuated at the beginning of a run. The sensitivity is determined by observing the change in the LVDT voltage signal when the argon pressure is reduced from 1 atm to 0 as the vessel is evacuated.

The pressure data obtained are shown in Fig. 2 together with some points estimated from the report by Bachman.¹ The solution is non ideal since the P pressure increases almost linearly from 0 to 2 atm as the P content rises from 0 to about 35 atomic percent and then nearly linearly again from 5 to 30 atm as the solution composition varies only from 40 to 50 atomic percent P. This non-ideal nature of the $\text{In}_{1-x}\text{P}_x$ solution is probably related to the P_2 and P_4 molecules in the vapor phase and the tendency of the phosphorus to form chains in the melt.

A convenient way to synthesize InP from the elements is illustrated schematically in Fig. 3. In this process, P is loaded into an injector consisting of an ampoule with a downward projecting tube that is open at the bottom. The injector can be lowered to position the end of the open tube into an In melt that is encapsulated with liquid B_2O_3 . This apparatus is housed in a vessel containing an inert gas at a pressure greater than 30 atm. Nitrogen gas at 40 atm is generally employed at Rome Laboratory. When the melt is held at a temperature above the melting point of InP (1065°C) and the injector temperature raised, P vapor transports into the In forming an $\text{In}_{1-x}\text{P}_x$ solution with x increasing from 0 to 0.5 as the P pressure increases from 0 to 30 atm. One of the problems in the synthesis process is the bubbling that occurs in the B_2O_3 encapsulant with the associated non-reproducible loss of phosphorus. The phosphorus coats the windows of the pressure vessel and also coats a silica dome that surrounds the melt, thereby limiting the vision required for *in situ* synthesis and liquid-encapsulated Kyropoulos growth. With the aid of the pressure data in Fig. 2 we have attempted to explain this behavior.

First, by using the data of Bachman for the vapor pressure of spongy red phosphorus as a function of temperature we have constructed the curve shown in Fig. 4. This figure shows the equilibrium temperature of a phosphorus reservoir that is required to produce an $\text{In}_{1-x}\text{P}_x$ melt at

1100°C plotted versus x . For a constant rate of phosphorus injection the abscissa could be labeled time (for example $x = 0.5$ could be labeled 3 hr for a 3 hour synthesis) and Fig. 2 would give the heating ramp required, provided that equilibrium were achieved at every point. Of course equilibrium will not be achieved with a continuously increasing phosphorus pressure and the reaction may be limited by the rate of sublimation of phosphorus gas from the solid and by the diffusion (or mixing) of P into the melt.

To explain the bubbling early in the process we consider the high-pressure N_2 gas that occupies both the pressure vessel and the phosphorus injector before the open injector tube is lowered into the melt. Since the volume of the injector is about 420 cm^3 and it contains about 250 g of P with a density of 2.2 g/cm^3 the N_2 gas occupies over 300 cm^3 at 40 atm and 300 K. Therefore the quantity of N_2 in the injector is about 0.5 mole. According to Fig. 2 when the injector is first heated from room temperature to 300°C, essentially no phosphorus is injected into the melt, but at 300°C the injector contains only about 0.26 mole of N_2 at 40 atm and therefore a volume of 680 cm^3 of N_2 (at 40 atm and 1100°C) must have escaped up through the In melt and the B_2O_3 at a rate of about $2\frac{1}{2}\text{ cm}^3$ per °C of injector temperature rise. No harm should be done to this point however, since very little if any phosphorus should have been carried along with the N_2 .

If we next consider the P pressure increase from nearly zero to about 3 atm as the injector temperature is increased from 300 to 415°C, the melt composition changes from pure In to $In_{0.63}P_{0.37}$. Since about 70% of the phosphorus is injected during this period, the N_2 remaining in the injector at 415°C occupies about 370 cm^3 at a partial pressure of 37 atm and amounts to about 0.24 mole. Therefore only about 55 cm^3 or 0.5 cm^3 of N_2 gas per °C of injector temperature rise bubbled out through the B_2O_3 during this part of the synthesis process.

We finally examine the rise from 3 to 30 atm corresponding to the phosphorus temperature increasing from 415 to 550°C and to the change from $In_{0.63}P_{0.37}$ to $In_{0.5}P_{0.5}$. Essentially all of the phosphorus is now in the vapor phase and the N_2 gas occupies the whole injector volume of 420 cm^3 but its partial pressure is 10 atm and therefore only 0.06 mole of N_2

remains in the injector. During this final phase of the injection then about 510 cm^3 of N_2 bubbles out at a much higher rate of about 4 cm^3 per $^\circ\text{C}$ of injector temperature rise. Experimentally it is in the last stage of the process that phosphorus often escapes and coats the windows and the silica dome.

If the primary cause of phosphorus loss through the B_2O_3 is the N_2 , it should in principle be possible to reduce the loss in a number of ways. If for instance a dense solid phosphorus charge could replace the low density "powder" charge now employed, the volume available for N_2 gas could be greatly reduced and therefore the volume of N_2 bubbling out would likewise be reduced. Such a charge could be used either with a ground tapered silica joint on an injector top or with a specially designed silica seal for fusing with a hydrogen torch. A further problem could then be encountered during the injection stage that increases the P content of the melt from 0 to 37 atomic %. Since a significant volume of solid phosphorus sublimates during this period with only 3 atm of P partial pressure increase, the total pressure in the injector can decrease due to the expansion of the N_2 into the volume that had been occupied by the red phosphorus. If the N_2 pressure in the growth chamber is held constant, the pressure differential will force a column of liquid up into the injector tube where it will freeze (because above the B_2O_3 the temperature rapidly falls below the liquidus temperature even for melts with P content as low as a few atomic %). The injector tube then becomes sealed and the injector explodes. If the N_2 pressure is reduced at the correct rate this problem could be avoided and the volume of N_2 bubbled out through the B_2O_3 , still substantially reduced. One other possibility might be to change from N_2 to Ar gas and to employ a quartz frit or a molecular sieve filter that would allow the argon to escape from the injector but not the larger P_4 molecules.

If a silica differential pressure transducer could be fabricated with a sensitivity better than about 0.01 psi (corresponding a head of liquid InP of about 1 mm) the injection process could begin with both the pressure vessel and the injector under vacuum. After the injector tube was lowered into the melt and when the phosphorus pressure began to rise, the N_2 pressure would be increased to just equal the phosphorus pressure with a tolerance of + 0.03 to -0 psi. The melt

would then not rise up into the injector tube (where it can freeze and seal off the injector due to the decreasing temperature in the upward direction) nor in principle would phosphorus bubble out through the B_2O_3 , since a thickness of 15 mm of B_2O_3 encapsulant would provide an additional hydrostatic pressure of about 0.03 psi.

Electrical Resistivity

The value of the electrical resistivity of liquid InP is required to model the effect of a magnetic field on the convective flow in the growth melt. After attempting to measure ρ with various melt container configurations, we finally succeeded with the silica "U" tube and graphite electrodes shown schematically in Fig. 5. The InP charge, which happened to be Zn doped to about 10^{18} cm^{-3} , was a cylinder which initially fit into one of the larger diameter tubes above the 3 mm i.d. "U" tube. B_2O_3 was loaded on top of the charge and also alongside the graphite electrodes in the other larger tube. Finally, the two remaining electrodes were inserted into the tube above the InP and B_2O_3 and weighted to slide down into the InP after it was melted to fill the "U" tube and contact all four electrodes. Voltage measurements were made at 1, 5, 10 and 15 amps in both polarities and averaged to find a resistance of 0.078Ω giving a resistivity of $2.5 \times 10^{-4} \Omega\text{cm}$ for an average melt temperature of about 1100°C .

One attempt to measure the electrical resistivity provided some amusement but perhaps also some potentially useful information for InP crystal growth in silica crucibles. A rectangular silica boat with inside dimensions 10 cm long, 1 mm wide and 6 mm deep was filled with a center slab of InP 8 cm long x 1 mm wide x 6 mm high and four rectangular graphite electrodes at the ends spaced with smaller InP slabs and all encapsulated with B_2O_3 inside a larger boat. Upon melting in the high-pressure furnace, the InP rose out of the boat and formed several spheres each about 4 to 6 mm in diameter indicating that at least under some conditions liquid InP does not wet silica.

Thermal Conductivity

An estimate of the thermal conductivity of molten InP was made by utilizing two concentric graphite cylinders submerged into liquid InP and all encapsulated with B₂O₃ in a high-pressure vessel. A schematic cross section is shown in Fig. 6. When power Q is applied to the Mo wire resistance heater inside the center graphite cylinder, the heat flows through the InP in the space separating the cylinders and creates a steady-state temperature difference ΔT between the thermocouples. The thermal conductivity k is then $\frac{Q}{\Delta T} \frac{\ln(d_o / d_i)}{2\pi\ell}$ where d_o is the i.d. of the outer cylinder (23.8 mm in our case) d_i is the o.d. of the inner cylinder (18.3 mm) and ℓ is the length of the heater and of the InP that conducts the heat (33 mm).

The InP was first melted with the furnace heater that was wound on a threaded Al₂O₃ core (not shown) and a flat heater below the bottom disc (also not shown). Then, for powers applied to the submerged heater ranging from 10 to 65 W, thermocouple temperatures were recorded until the temperature reached steady-state values. The power to the bottom flat heater was then slowly decreased in order to solidify the melt from the bottom to avoid breakage due to the expansion of InP on freezing. The same type of temperature recordings were then made just below the 1065°C melting point. After that, the material was once again melted and another set of data obtained for the liquid. Finally after very slowly freezing the InP again, data were taken at a number of temperatures between 1050 and 60°C.

The major uncertainty in the calculated thermal conductivity is the power that is actually generated inside the submerged graphite cylinder, since the Mo wire heater length inside that cylinder is only 99 cm; not much longer than the two lead lengths which add to 78 cm. Taking the published temperature coefficient of the resistance of Mo (0.0046°C⁻¹) and approximating the temperature along each lead, we estimate that ~80% of the external power is generated inside the cylinder. The results are shown in Fig. 7 together with the best analytical fit to the previous experimental data² for solid InP. The ratio of the thermal conductivity of liquid InP just above the 1065°C melting point to that of the solid just below 1065°C is about 1.5.

Density of Liquid InP

Measuring the density of a liquid in the usual manner by accurately weighting a mass before and after it is submerged in the melt would be difficult in the case of InP because of the viscous B_2O_3 encapsulant required to prevent P evaporation. In addition, the precision balance would need to be located inside a high-pressure vessel under a pressure greater than 30 atm and subject to heating from the furnace used to melt InP at 1065 °C. Therefore several experiments were carried out to detect the height of a melt in a tall crucible by lowering a graphite probe until electrical contact with the liquid was made, and then to freeze the InP and detect the height of the solid in the same manner.

In one experiment a flat bottom fused silica ampoule with 36 mm i.d. was employed with two close-fitting sleeves inserted part way down so that the i.d. at the top was 27 mm. A graphite electrode and a thermocouple inside a 7 mm o.d. silica tube were secured to one side of the ampoule inside the upper zone. Another graphite probe located near the center of the ampoule was moved up and down to detect that top of the molten or solid InP via electrical contact. A schematic diagram is shown in Fig. 8. After heating until the thermocouple immersed in the charge indicated a temperature above the InP melting point, clear thermal arrests were observed during cooling indicating that the material froze without severe super cooling. Unfortunately the bottom molybdenum flat wire heater burned out during the first heating cycle but the experiment was continued. The relative height of the melt indicated by electrical contact after the first heating cycle was 64.3 mm. After cooling through the thermal arrest the height of the solid was 66.0 mm, after reheating 63.9 mm and after cooling again 65.0 mm. By observing a longitudinal section of the ingot after the experiment it became obvious that the bottom 30 mm length had never melted. Although it was fairly dense (apparently due to mass transport in the solid state) it contained some holes and a clear line of demarcation was observed between the top melted part with no holes and the bottom. Effectively then, the height of the 36-mm-dia cylinder that melted and froze was 59 mm and that of the 27-mm-dia part 30 mm. The increase in height due to

freezing was taken to be the average of the 1.7 mm height increase after the first melting and freezing and the 1.1 mm increase after the second melting (presumably to a somewhat lower position along the ingot) and freezing. The 1.4 mm average corresponds to a density change of about 1.1%. This is certainly far from the 7.2% change that is obtained from the data of Glazov *et al.*^{3,4} who report 4.71 grams/cm³ for the density of the solid and 5.05 grams/cm³ for that of the liquid.

Since the discrepancy is so large and the reliability of the density data reported in Ref. 3 and 4 is difficult to assess, a very simple experiment was carried out in a "U" tube shown schematically in Fig. 9. The whole "U" tube was located inside a larger open crucible and entirely encapsulated with B₂O₃ to a level above its open top. After melting the InP charge in a pressure vessel, the temperature of the bottom was slowly reduced in order to directionally freeze the melt. A thermal arrest indicated that very little super cooling occurred and that the melt did indeed freeze from the bottom up. If the liquid level had been at the point indicated in Fig. 9 and a significant density decrease occurred on freezing, the height of InP in the right hand column with the reduced diameter should have raised 9 times as much as that in the left column with the 9 mm diameter. In fact, we found no measurable difference in the heights although the level was about 5 mm above the bottom of the 3-mm-dia section. In spite of this, the level in the right column should still raise more than 8 times that in the left. A possible problem is that the liquid levels in the two columns were different due to the diameter difference but if the density difference were 7% the liquid levels would have had to be well below the 3 mm diameter section.

References

1. K.J. Bachman and E. Buehler, *J. Electrochem. Soc.* **121**, 835 (1974).
2. C.M. Bhandari and D.M Rowe, *Thermal Conduction in Semiconductors* (Wiley, New York, 1988).
3. V.M. Glazov, A. Ya. Nashel'skii, F.R. Rzaev, M.M. Mamedov, *Sov. Phys. Semicond.* (USA) **10**, 498 (1976).
4. V.M. Glazov, K. Dovletov, A. Ya. Nashel'skii, and M.M. Madedov, *Inorg. Mater.* **13**, 26 (1977).

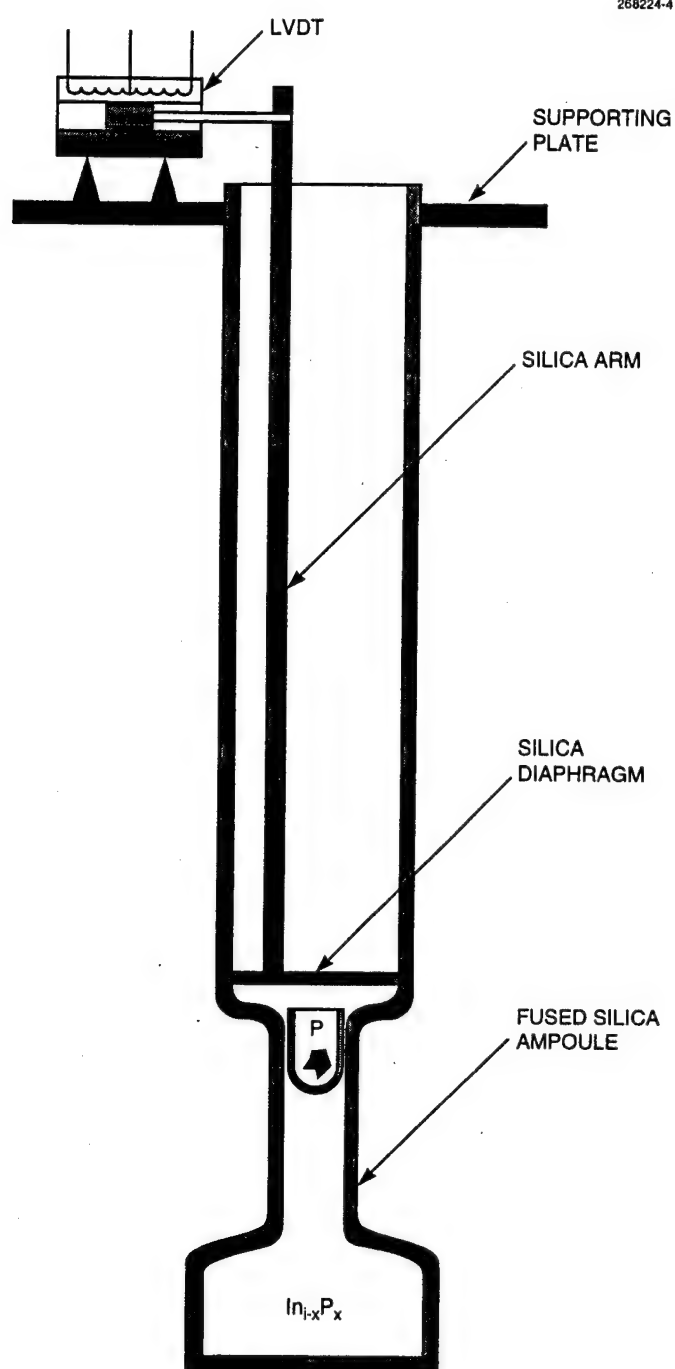


Fig. 1 Fused silica ampoule and linear variable differential transformer for measuring phosphorus pressure over $\text{In}_{1-x}\text{P}_x$ liquids. Pressure of argon outside sealed part of ampoule is adjusted to obtain zero deflection of diaphragm. At that point phosphorus pressure is equal to measured argon pressure.

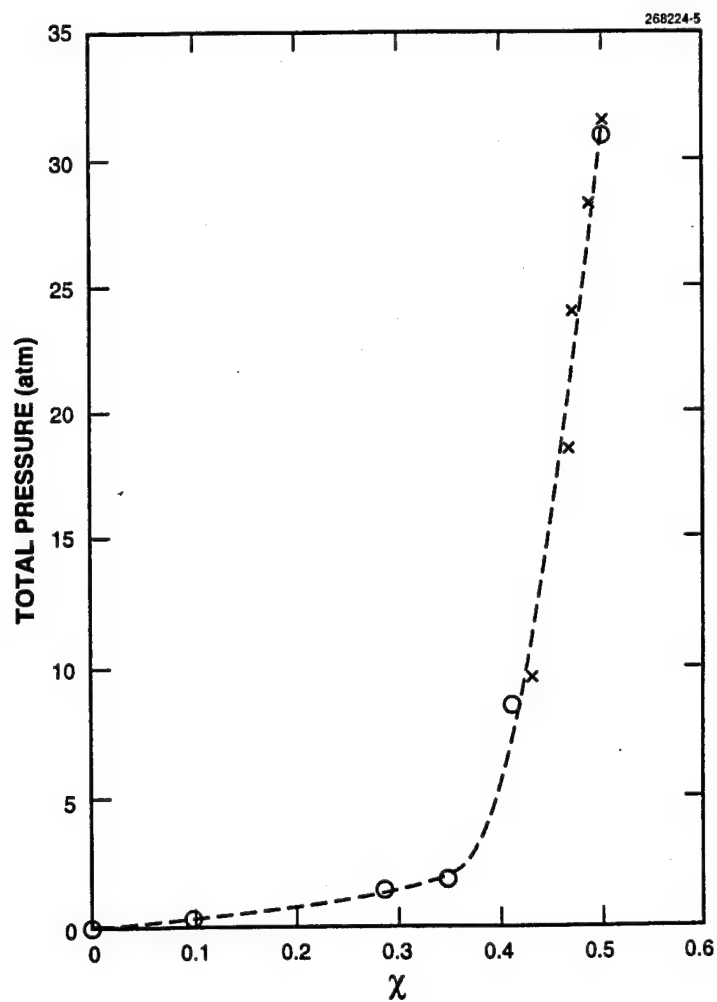


Fig. 2 Total phosphorus pressure over $\text{In}_{1-x}\text{P}_x$ versus x at 1100°C ; present data (x) points estimated from data of Bachman (●).

In-Situ Synthesis and Growth Method for InP

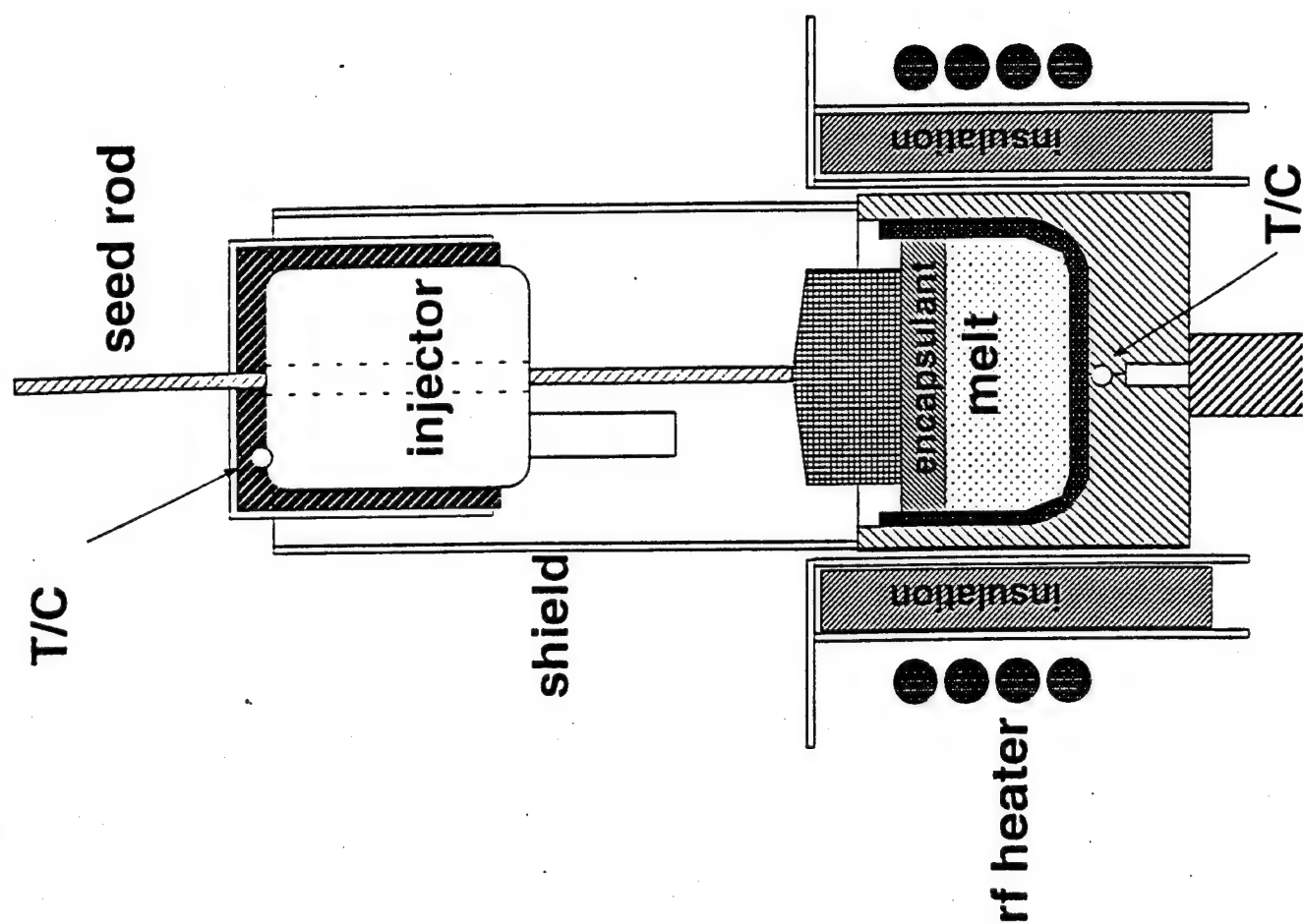


Fig. 3 Schematic of apparatus for synthesizing InP from the elements by injecting

phosphorus vapor into an In melt at 1000°C

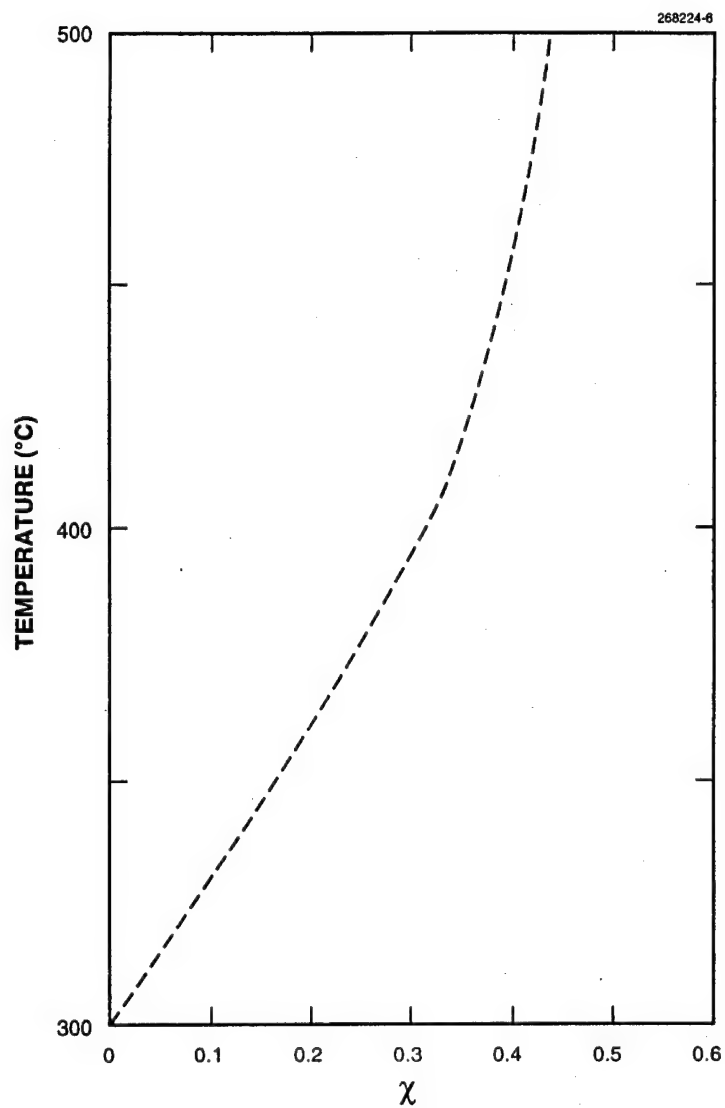


Fig. 4 Approximate temperature of phosphorus reservoir required to establish equilibrium for $\text{In}_{1-x}\text{P}_x$ liquid at 1100°C versus x .

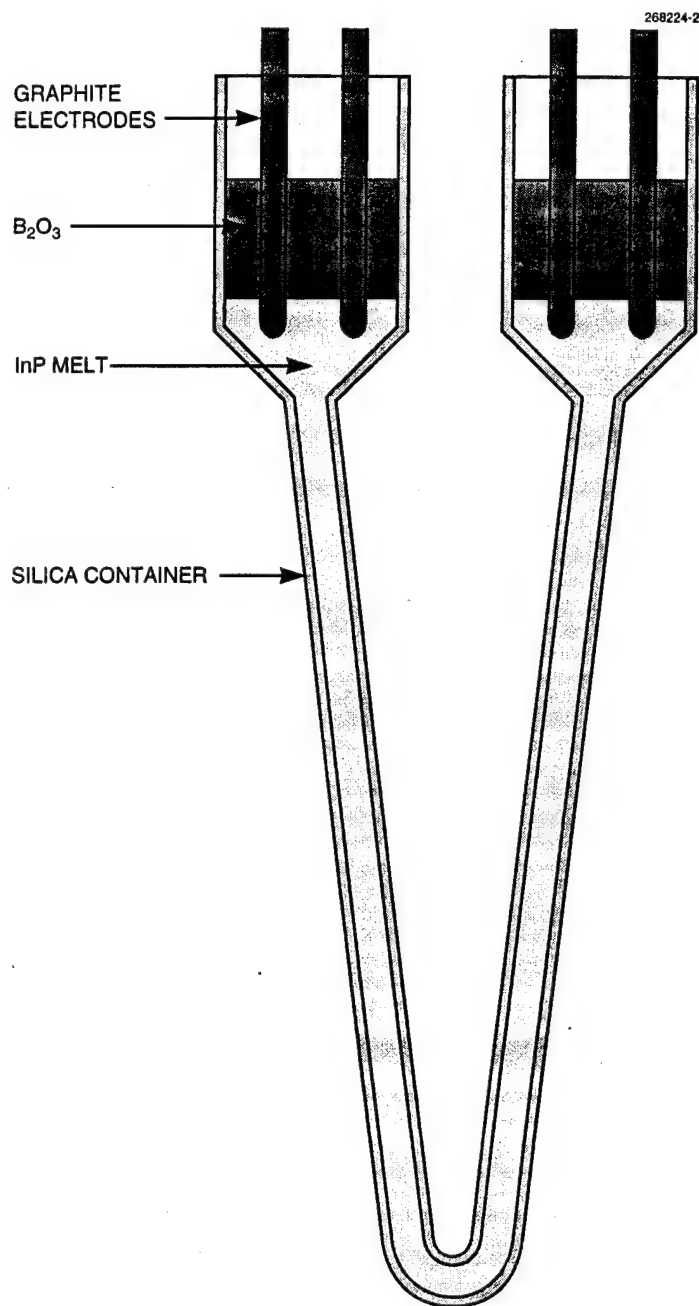


Fig. 5 Fused silica "U" tube to measure electrical resistivity of molten InP. One electrode on each side carried d.c. current and other was used for voltage measurement.

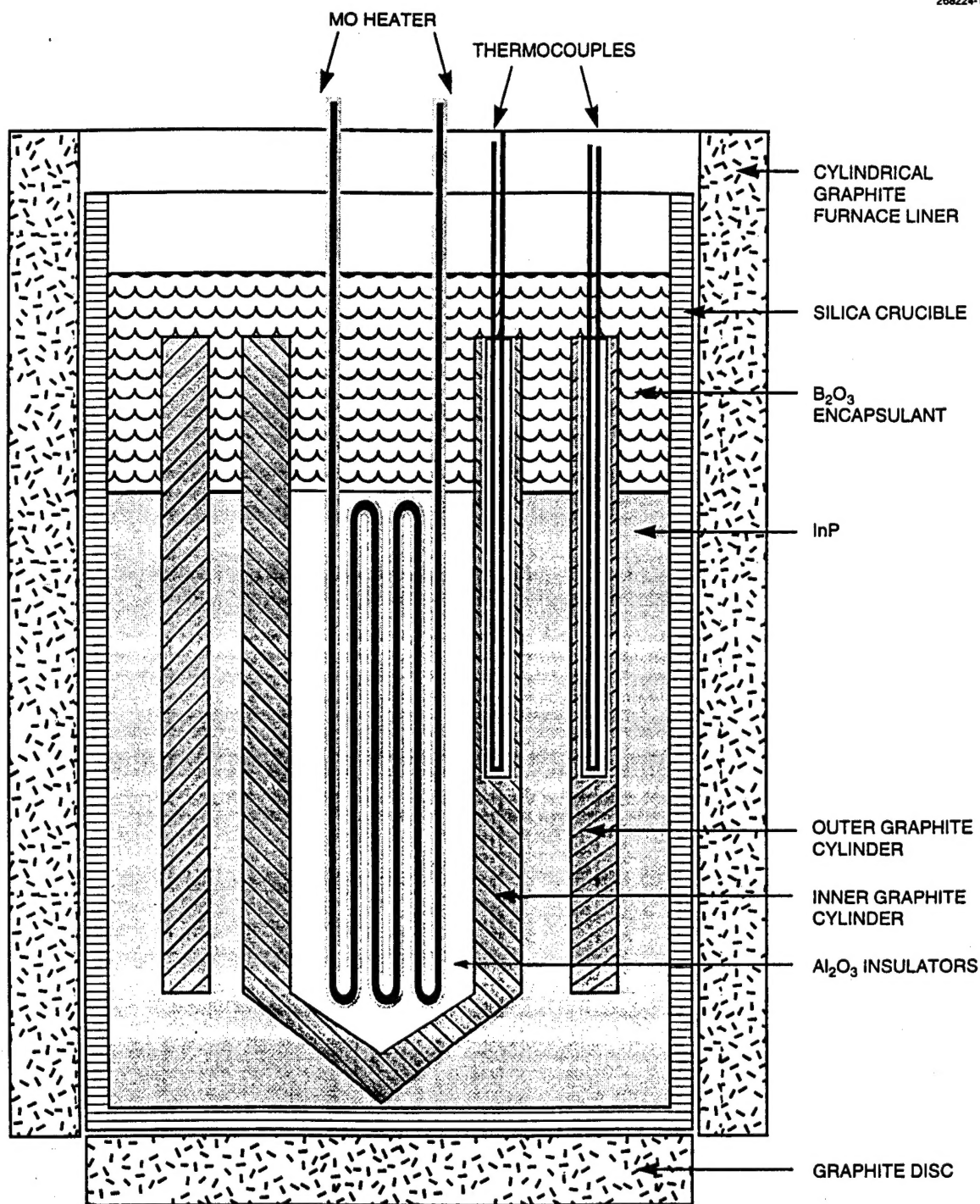


Fig. 6 Apparatus for thermal conductivity measurement of solid and liquid InP. Temperature difference between two thermocouples was measured as a function of power supplied by Mo heater.

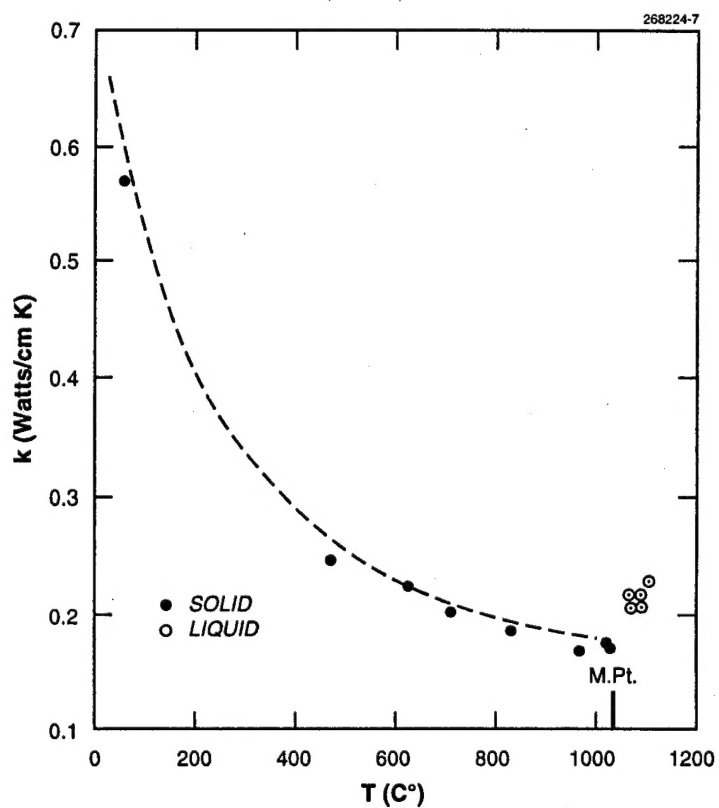


Fig. 7 Thermal conductivity measured as a function of temperature for solid and liquid InP. Dashed line is approximate curve representing previous data² for solid InP.

268224-3

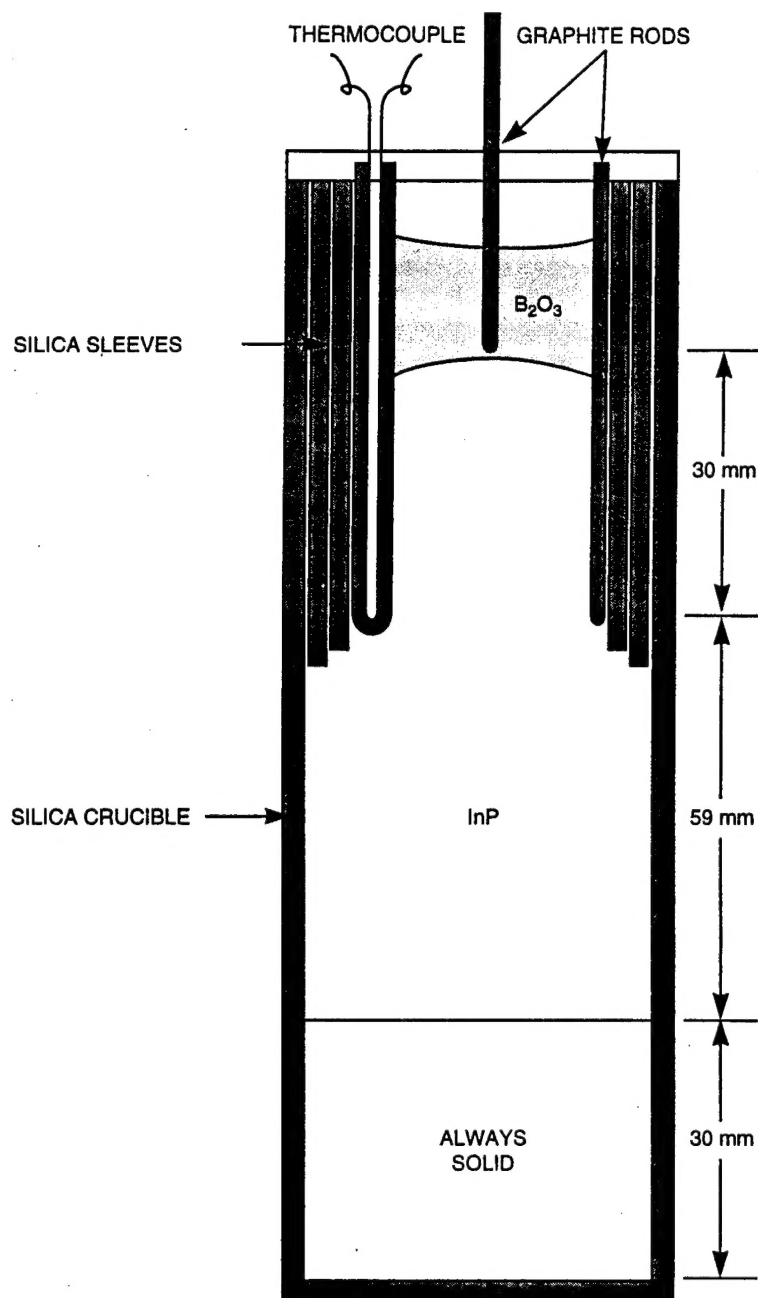


Fig. 8 Schematic diagram of fused silica tube with sleeves to estimate relative density of liquid InP compared to solid material.

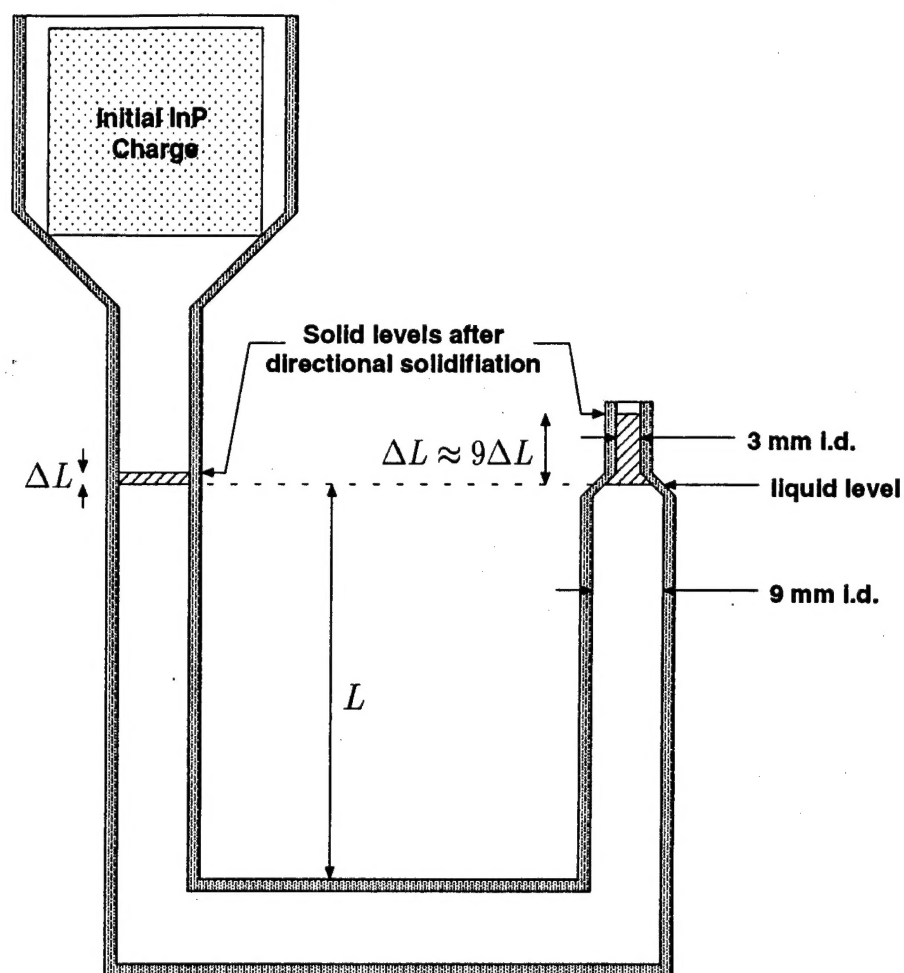


Fig. 9 Schematic diagram of fused silica "U" tube to estimate InP density change on freezing.